

1 SEARCH FOR PRODUCTION OF A HIGGS BOSON AND A SINGLE TOP
2 QUARK IN MULTILEPTON FINAL STATES IN pp COLLISIONS AT $\sqrt{s} = 13$
3 TeV.

4 by

5 Jose Andres Monroy Montañez

A DISSERTATION

7 Presented to the Faculty of

8 The Graduate College at the University of Nebraska

In Partial Fulfilment of Requirements

10 For the Degree of Doctor of Philosophy

11 Major: Physics and Astronomy

12 Under the Supervision of Kenneth Bloom and Aaron Dominguez

13 Lincoln, Nebraska

14 July, 2018

15 SEARCH FOR PRODUCTION OF A HIGGS BOSON AND A SINGLE TOP
16 QUARK IN MULTILEPTON FINAL STATES IN pp COLLISIONS AT $\sqrt{s} = 13$
17 TeV.

18 Jose Andres Monroy Montañez, Ph.D.

19 University of Nebraska, 2018

20 Adviser: Kenneth Bloom and Aaron Dominguez

₂₁ Table of Contents

₂₂ Table of Contents	iii
₂₃ List of Figures	vii
₂₄ List of Tables	x
₂₅ 1 INTRODUCTION	1
₂₆ 2 Theoretical approach	2
27 2.1 Introduction	2
28 2.2 Standard model of particle physics	3
29 2.2.1 Fermions	5
30 2.2.1.1 Leptons	6
31 2.2.1.2 Quarks	8
32 2.2.2 Fundamental interactions	12
33 2.2.3 Gauge invariance.	15
34 2.2.4 Gauge bosons	18
35 2.3 Electroweak unification and the Higgs mechanism	19
36 2.3.1 Spontaneous symmetry breaking (SSB)	27
37 2.3.2 Higgs mechanism	31

38	2.3.3	Masses of the gauge bosons	34
39	2.3.4	Masses of the fermions	35
40	2.3.5	The Higgs field	36
41	2.3.6	Production of Higgs bosons at LHC	37
42	2.3.7	Higgs boson decay channels	41
43	2.4	Experimental status of the anomalous Higgs-fermion coupling	42
44	2.5	Associated production of a Higgs boson and a single top quark	44
45	2.6	CP-mixing in tH processes	49
46	3	The CMS experiment at the LHC	54
47	3.1	Introduction	54
48	3.2	The LHC	55
49	3.3	The CMS experiment	65
50	3.3.1	CMS coordinate system	68
51	3.3.2	Tracking system	70
52	3.3.3	Silicon strip tracker	73
53	3.3.4	Electromagnetic calorimeter	74
54	3.3.5	Hadronic calorimeter	76
55	3.3.6	Superconducting solenoid magnet	77
56	3.3.7	Muon system	79
57	3.3.8	CMS trigger system	80
58	3.3.9	CMS computing	81
59	4	Event generation, simulation and reconstruction	86
60	4.1	Event generation	87
61	4.2	Monte Carlo Event Generators	91
62	4.3	CMS detector simulation	92

63	4.4 Event reconstruction	94
64	4.4.1 Particle-Flow Algorithm	94
65	4.4.1.1 Missing transverse energy	106
66	4.4.2 Event reconstruction examples	106
67	5 Statistical methods	110
68	5.1 Multivariate analysis	110
69	5.1.1 Decision trees	113
70	5.1.2 Boosted decision trees (BDT)	116
71	5.1.3 Overtraining.	119
72	5.1.4 Variable ranking.	119
73	5.1.5 BDT output example.	120
74	5.2 Statistical inference.	121
75	5.2.1 Nuisance parameters.	121
76	5.2.2 Maximum likelihood estimation method	122
77	5.2.3 Hypothesis test	123
78	5.3 exclusion limits	124
79	5.4 asymptotic limits	124
80	6 Search for production of a Higgs boson and a single top quark in multilepton final states in pp collisions at $\sqrt{s} = 13$ TeV	125
82	6.1 Introduction	125
83	6.2 tHq signature	127
84	6.3 Background processes	129
85	6.4 Data and MC Samples	131
86	6.4.1 Full 2016 dataset and MC samples	131
87	6.4.2 Triggers	132

88	6.5 Object Identification	136
89	6.5.1 Jets and b -jet tagging.	136
90	6.5.2 Missing Energy MET.	137
91	6.5.3 Lepton reconstruction and identification	138
92	6.5.4 Lepton selection efficiency	146
93	6.6 Event selection	148
94	6.7 Background predictions	149
95	6.8 Signal discrimination	151
96	6.8.1 Classifiers response	153
97	6.9 Additional discriminating variables	157
98	Bibliography	159
99	References	161

¹⁰⁰ List of Figures

101	2.1 Standard Model of particle physics.	4
102	2.2 Transformations between quarks	12
103	2.3 Fundamental interactions in nature.	13
104	2.4 SM interactions diagrams	14
105	2.5 Neutral current processes	20
106	2.6 Spontaneous symmetry breaking mechanism	28
107	2.7 SSB Potential form	29
108	2.8 Potential for complex scalar field	30
109	2.9 SSB mechanism for complex scalar field	31
110	2.10 Proton-Proton collision	37
111	2.11 Higgs boson production mechanism Feynman diagrams	39
112	2.12 Higgs boson production cross section and decay branching ratios	40
113	2.13 Two dimensional κ_t - κ_V plot of the coupling modifiers. ATLAS and CMS combination.	43
115	2.14 Higgs boson production in association with a top quark mechanism Feyn- man diagrams	45
117	2.15 Cross section for tHq process as a function of κ_t	48
118	2.16 Cross section for tHW process as a function of κ_{Htt}	48

119	2.17 NLO cross section for tX_0 and $t\bar{t}X_0$.	52
120	2.18 NLO cross section for tWX_0 , $t\bar{t}X_0$.	53
121	3.1 CERN accelerator complex	55
122	3.2 LHC protons source. First acceleration stage.	56
123	3.3 The LINAC2 accelerating system at CERN.	57
124	3.4 LHC layout and RF cavities module.	58
125	3.5 LHC dipole magnet.	60
126	3.6 Integrated luminosity delivered by LHC and recorded by CMS during 2016	62
127	3.7 LHC interaction points	63
128	3.8 Multiple pp collision bunch crossing at CMS.	65
129	3.9 Layout of the CMS detector	66
130	3.10 CMS detector transverse slice	67
131	3.11 CMS detector coordinate system	69
132	3.12 CMS tracking system schematic view.	70
133	3.13 CMS pixel detector	71
134	3.14 SST Schematic view.	73
135	3.15 CMS ECAL schematic view	75
136	3.16 CMS HCAL schematic view	77
137	3.17 CMS solenoid magnet	78
138	3.18 CMS Muon system schematic view	79
139	3.19 CMS Level-1 trigger architecture	81
140	3.20 WLCG structure	82
141	3.21 Data flow from CMS detector through hardware Tiers	84
142	4.1 Event generation process.	87
143	4.2 Particle flow algorithm.	95

144	4.3	Jet reconstruction.	102
145	4.4	Jet energy corrections.	103
146	4.5	Secondary vertex in a b-hadron decay.	105
147	4.6	HIG-13-004 Event 1 reconstruction.	107
148	4.7	$e\mu$ event reconstruction.	108
149	4.8	Recorded event reconstruction.	109
150	5.1	Scatter plots-MVA event classification.	112
151	5.2	Scalar test statistical.	112
152	5.3	Decision tree.	114
153	5.4	Decision tree output example.	117
154	5.5	BDT output example.	120
155	6.1	tHq event signature.	128
156	6.2	$t\bar{t}$ and $t\bar{t}W$ events signature.	130
157	6.3	Tight vs loose lepton selection efficiencies in the 2lss channel.	146
158	6.4	Tight vs loose lepton selection efficiencies in the 3l channel.	147
159	6.5	Input variables to the BDT for signal discrimination normalized.	152
160	6.6	Input variables to the BDT for signal discrimination not normalized.	154
161	6.7	BDT inputs as seen by TMVA against $t\bar{t}$.	155
162	6.8	BDT inputs as seen by TMVA against $t\bar{t}V$.	156
163	6.9	Correlation matrices for the input variables in the TMVA.	157
164	6.10	MVA classifiers performance.	157
165	6.11	Additional discriminating variables distributions.	159

¹⁶⁶ List of Tables

167	2.1	Fermions of the SM.	5
168	2.2	Fermion masses.	6
169	2.3	Lepton properties.	8
170	2.4	Quark properties.	9
171	2.5	Fermion weak isospin and weak hypercharge multiplets.	11
172	2.6	Fundamental interactions features.	15
173	2.7	SM gauge bosons.	19
174	2.8	Higgs boson properties.	37
175	2.9	Predicted branching ratios for a SM Higgs boson with $m_H = 125 \text{ GeV}/c^2$	41
176	2.10	Predicted SM cross sections for tH production at $\sqrt{s} = 13 \text{ TeV}$	46
177	2.11	Predicted enhancement of the tHq and tHW cross sections at LHC	49
178	6.1	Signal samples and their cross section and branching fraction.	132
179	6.2	κ_V and κ_t combinations.	133
180	6.3	List of background samples used in this analysis (CMSSW 80X).	134
181	6.4	Leading-order $t\bar{t}W$ and $t\bar{t}Z$ samples used in the signal BDT training.	134
182	6.5	Table of high-level triggers that we consider in the analysis.	135
183	6.6	Trigger efficiency scale factors and associated uncertainties.	136
184	6.7	Effective areas, for electrons and muons.	142

185	6.8 Requirements on each of the three muon selections.	145
186	6.9 Criteria for each of the three electron selections.	145
187	6.10 MVA input discriminating variables	153
188	6.11 TMVA input variables ranking for BDTA_GRAD method	158
189	6.12 TMVA configuration used in the BDT training.	158
190	6.13 ROC-integral for all the testing cases.	160

¹⁹¹ Chapter 1

¹⁹² INTRODUCTION

¹⁹³ **Chapter 2**

¹⁹⁴ **Theoretical approach**

¹⁹⁵ **2.1 Introduction**

¹⁹⁶ The physical description of the universe is a challenge that physicists have faced by
¹⁹⁷ making theories that refine existing principles and proposing new ones in an attempt
¹⁹⁸ to embrace emerging facts and phenomena.

¹⁹⁹ At the end of 1940s Julian Schwinger [1] and Richard P. Feynman [2], based on
²⁰⁰ the work of Sin-Itiro Tomonaga [3], developed an electromagnetic theory consistent
²⁰¹ with special relativity and quantum mechanics that describes how matter and light
²⁰² interact; the so-called *quantum electrodynamics* (QED) was born.

²⁰³ QED has become the guide in the development of theories that describe the uni-
²⁰⁴ verse. It was the first example of a quantum field theory (QFT), which is the theore-
²⁰⁵ tical framework for building quantum mechanical models that describes particles and
²⁰⁶ their interactions. QFT is composed of a set of mathematical tools that combines
²⁰⁷ classical fields, special relativity and quantum mechanics, while keeping the quantum
²⁰⁸ point particles and locality ideas.

²⁰⁹ This chapter gives an overview of the standard model of particle physics, starting

210 with a description of the particles and interactions that compose it, followed by a
 211 description of the electroweak interaction, the Higgs boson and the associated pro-
 212 duction of Higgs boson and a single top quark (tH). The description contained in
 213 this chapter is based on References [4–6].

214 2.2 Standard model of particle physics

215 Particle physics at the fundamental level is modeled in terms of a collection of inter-
 216 acting particles and fields in a theory known as the *standard model of particle physics*
 217 (*SM*). The full picture of the SM is composed of three fields¹ whose excitations are
 218 interpreted as particles called mediators or force-carriers, a set of fields whose excita-
 219 tions are interpreted as elementary particles interacting through the exchange of those
 220 mediators, and a field that gives the mass to elementary particles. Figure 2.1 shows
 221 the scheme of the SM particles’ organization. In addition, for each of the particles
 222 in the scheme there exists an antiparticle with the same mass and opposite quantum
 223 numbers. The existence of antiparticles is a prediction of the relativistic quantum
 224 mechanics from the solution of the Dirac equation for which a negative energy solu-
 225 tion is also possible. In some cases a particle is its own anti-particle, like photon or
 226 Higgs boson.

227 The mathematical formulation of the SM is based on group theory and the use of
 228 Noether’s theorem [8] which states that for a physical system modeled by a Lagrangian
 229 that is invariant under a group of transformations a conservation law is expected. For
 230 instance, a system described by a time-independent Lagrangian is invariant (symmet-
 231 ric) under time changes (transformations) with the total energy conservation law as

¹ The formal and complete treatment of the SM is out of the scope of this document, however a plenty of textbooks describing it at several levels are available in the literature. The treatment in References [5, 6] is quite comprehensive and detailed. Note that gravitational field is not included in the standard model formulation

Standard Model of Elementary Particles

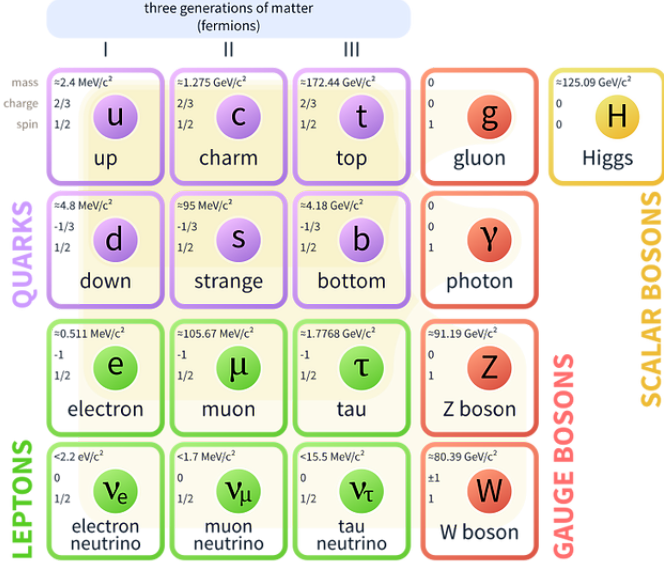


Figure 2.1: Schematic representation of the Standard Model of particle physics. The SM is a theoretical model intended to describe three of the four fundamental forces of the universe in terms of a set of particles and their interactions. [7].

the expected conservation law. In QED, the charge operator (Q) is the generator of the $U(1)$ symmetry which according to the Noether's theorem means that there is a conserved quantity; this conserved quantity is the electric charge and thus the law of conservation of electric charge is established.

In the SM, the symmetry group $SU(3)_C \otimes SU(2)_L \otimes U(1)_Y$ describes three of the four fundamental interactions in nature (see Section 2.2.2): strong interaction (SI), weak interaction (WI) and electromagnetic interactions (EI) in terms of symmetries associated to physical quantities:

- Strong: $SU(3)_C$ associated to color charge
- Weak: $SU(2)_L$ associated to weak isospin and chirality
- Electromagnetic: $U(1)_Y$ associated to weak hypercharge and electric charge

243 It will be shown that the electromagnetic and weak interactions are combined in
 244 the so-called electroweak interaction where chirality, hypercharge, weak isospin and
 245 electric charge are the central concepts.

246 **2.2.1 Fermions**

247 The basic constituents of the ordinary matter at the lowest level, which form the set
 248 of elementary particles in the SM formulation, are quarks and leptons. All of them
 249 have spin 1/2, therefore they are classified as fermions since they obey Fermi-Dirac
 250 statistics. There are six *flavors* of quarks and three of leptons organized in three
 251 generations, or families, as shown in Table 2.1.

		Generation		
		1st	2nd	3rd
Leptons	Charged	Electron (e)	Moun(μ)	Tau (τ)
	Neutral	Electron neutrino (ν_e)	Muon neutrino (ν_μ)	Tau neutrino (ν_τ)
Quarks	Up-type	Up (u)	Charm (c)	Top (t)
	Down-type	Down (d)	Strange (s)	Bottom (b)

Table 2.1: Fermions of the SM. There are six flavors of quarks and three of leptons, organized in three generations, or families, composed of two pairs of closely related particles. The close relationship is motivated by the fact that each pair of particles is a member of an $SU(2)_L$ doublet that has an associated invariance under isospin transformations. WI between leptons is limited to the members of the same generation; WI between quarks is not limited but greatly favored, to same generation members.

252

253 There is a mass hierarchy between generations (see Table 2.2), where the higher
 254 generation particles decays to the lower one, which can explain why the ordinary
 255 matter is made of particles from the first generation. In the SM, neutrinos are modeled
 256 as massless particles so they are not subject to this mass hierarchy; however, today it
 257 is known that neutrinos are massive so the hierarchy could be restated. The reason
 258 behind this mass hierarchy is one of the most important open questions in particle

259 physics, and it becomes more puzzling when noticing that the mass difference between
 260 first and second generation fermions is small compared to the mass difference with
 261 respect to the third generation.

Lepton	Mass (MeV/c ²)	Quark	Mass (MeV/c ²)
e	0.51	u	2.2
μ	105.65	c	1.28×10^3
τ	1776.86	t	173.1×10^3
ν_e	Unknown	d	4.7
ν_μ	Unknown	s	96
τ_μ	Unknown	b	4.18×10^3

Table 2.2: Fermion masses [9]. Generations differ by mass in a way that has been interpreted as a mass hierarchy. Approximate values with no uncertainties are used, for comparison purpose.

262

263 Usually, the second and third generation fermions are produced in high energy
 264 processes, like the ones recreated in particle accelerators.

265 **2.2.1.1 Leptons**

266 A lepton is an elementary particle that is not subject to the SI. As seen in Table 2.1,
 267 there are two types of leptons, the charged ones (electron, muon and tau) and the
 268 neutral ones (the three neutrinos). The electric charge (Q) is the property that gives
 269 leptons the ability to participate in the EI. From the classical point of view, Q plays
 270 a central role determining, among others, the strength of the electric field through
 271 which the electromagnetic force is exerted. It is clear that neutrinos are not affected
 272 by EI because they don't carry electric charge.

273 Another feature of the leptons that is fundamental in the mathematical description
 274 of the SM is the chirality, which is closely related to spin and helicity. Helicity
 275 defines the handedness of a particle by relating its spin and momentum such that

276 if they are parallel then the particle is right-handed; if spin and momentum are
 277 antiparallel the particle is said to be left-handed. The study of parity conservation
 278 (or violation) in β -decay has shown that only left-handed electrons/neutrinos or right-
 279 handed positrons/anti-neutrinos are created [10]; the inclusion of that feature in the
 280 theory was achieved by using projection operators for helicity, however, helicity is
 281 frame dependent for massive particles which makes it not Lorentz invariant and then
 282 another related attribute has to be used: *chirality*.

283 Chirality is a purely quantum attribute which makes it not so easy to describe in
 284 graphical terms but it defines how the wave function of a particle transforms under
 285 certain rotations. As with helicity, there are two chiral states, left-handed chiral (L)
 286 and right-handed chiral (R). In the highly relativistic limit where $E \approx p \gg m$ helicity
 287 and chirality converge, becoming exactly the same for massless particles.

288 In the following, when referring to left-handed (right-handed) it will mean left-
 289 handed chiral (right-handed chiral). The fundamental fact about chirality is that
 290 while EI and SI are not sensitive to chirality, in WI left-handed and right-handed
 291 fermions are treated asymmetrically, such that only left-handed fermions and right-
 292 handed anti-fermions are allowed to couple to WI mediators, which is a violation of
 293 parity. The way to translate this statement in a formal mathematical formulation is
 294 based on the isospin symmetry group $SU(2)_L$.

295 Each generation of leptons is seen as a weak isospin doublet.² The left-handed
 296 charged lepton and its associated left-handed neutrino are arranged in doublets of
 297 weak isospin $T=1/2$ while their right-handed partners are singlets:

$$\begin{pmatrix} \nu_l \\ l \end{pmatrix}_L, l_R := \begin{pmatrix} \nu_e \\ e \end{pmatrix}_L, \begin{pmatrix} \nu_\mu \\ \mu \end{pmatrix}_L, \begin{pmatrix} \nu_\tau \\ \tau \end{pmatrix}_L, e_R, \mu_R, \tau_R, \nu_{eR}, \nu_{\mu R}, \nu_{\tau R} \quad (2.1)$$

² The weak isospin is an analogy of the isospin symmetry in strong interaction where neutron and proton are affected equally by strong force but differ in their charge.

298 The isospin third component refers to the eigenvalues of the weak isospin operator
 299 which for doublets is $T_3 = \pm 1/2$, while for singlets it is $T_3 = 0$. The physical meaning
 300 of this doublet-singlet arrangement falls in that the WI couples the two particles in
 301 the doublet by exchanging the interaction mediator while the singlet member is not
 302 involved in WI. The main properties of the leptons are summarized in Table 2.3.

303 Although all three flavor neutrinos have been observed, their masses remain un-
 304 known and only some estimations have been made [11]. The main reason is that
 305 the flavor eigenstates are not the same as the mass eigenstates which implies that
 306 when a neutrino is created its mass state is a linear combination of the three mass
 307 eigenstates and experiments can only probe the squared difference of the masses. The
 308 Pontecorvo-Maki-Nakagawa-Sakata (PMNS) mixing matrix encodes the relationship
 309 between flavor and mass eigenstates.

Lepton	$Q(e)$	T_3	L_e	L_μ	L_τ	Lifetime (s)
Electron (e)	-1	-1/2	1	0	0	Stable
Electron neutrino(ν_e)	0	1/2	1	0	0	Unknown
Muon (μ)	-1	-1/2	0	1	0	2.19×10^{-6}
Muon neutrino (ν_μ)	0	1/2	0	1	0	Unknown
Tau (τ)	-1	-1/2	0	0	1	290.3×10^{-15}
Tau neutrino (τ_μ)	0	1/2	0	0	1	Unknown

Table 2.3: Lepton properties [9]. Q: electric charge, T_3 : weak isospin. Only left-handed leptons and right-handed anti-leptons participate in the WI. Anti-particles with inverted T_3 , Q and lepton number complete the leptons set but are not listed. Right-handed leptons and left-handed anti-leptons, neither listed, form weak isospin singlets with $T_3 = 0$ and do not take part in the weak interaction.

310

311 2.2.1.2 Quarks

312 Quarks are the basic constituents of protons and neutrons. The way quarks join to
 313 form bound states, called *hadrons*, is through the SI. Quarks are affected by all the

314 fundamental interactions which means that they carry all the four types of charges:
 315 color, electric charge, weak isospin and mass.

Flavor	$Q(e)$	I_3	T_3	B	C	S	T	B'	Y	Color
Up (u)	2/3	1/2	1/2	1/3	0	0	0	0	1/3	r,b,g
Charm (c)	2/3	0	1/2	1/3	1	0	0	0	4/3	r,b,g
Top(t)	2/3	0	1/2	1/3	0	0	1	0	4/3	r,b,g
Down(d)	-1/3	-1/2	-1/2	1/3	0	0	0	0	1/3	r,b,g
Strange(s)	-1/3	0	-1/2	1/3	0	-1	0	0	-2/3	r,b,g
Bottom(b)	-1/3	0	-1/2	1/3	0	0	0	-1	-2/3	r,b,g

Table 2.4: Quark properties [9]. Q: electric charge, I_3 : isospin, T_3 : weak isospin, B: baryon number, C: charmness, S: strangeness, T: topness, B' : bottomness, Y: hypercharge. Anti-quarks posses the same mass and spin as quarks but all charges (color, flavor numbers) have opposite sign.

316

317 Table 2.4 summarizes the features of quarks, among which the most remarkable
 318 is their fractional electric charge. Note that fractional charge is not a problem, given
 319 that quarks are not found isolated, but serves to explain how composed particles are
 320 formed out of two or more valence quarks³.

321 Color charge is responsible for the SI between quarks and is the symmetry ($SU(3)_C$)
 322 that defines the formalism to describe SI. There are three colors: red (r), blue (b)
 323 and green (g) and their corresponding three anti-colors; thus each quark carries one
 324 color unit while anti-quarks carries one anti-color unit. As explained in Section 2.2.2,
 325 quarks are not allowed to be isolated due to the color confinement effect, hence, their
 326 features have been studied indirectly by observing their bound states created when

- 327 • one quark with a color charge is attracted by an anti-quark with the correspond-
 328 ing anti-color charge forming a colorless particle called a *meson*.

³ Hadrons can contain an indefinite number of virtual quarks and gluons, known as the quark and gluon sea, but only the valence quarks determine hadrons' quantum numbers.

329 • three quarks (anti-quarks) with different color (anti-color) charges are attracted
 330 among them forming a colorless particle called a *baryon* (*anti-baryon*).

331 In practice, when a quark is left alone isolated a process called *hadronization* occurs
 332 where the quark emits gluons (see Section 2.2.4) which eventually will generate new
 333 quark-antiquark pairs and so on; those quarks will recombine to form hadrons that
 334 will decay into leptons. This proliferation of particles looks like a *jet* coming from
 335 the isolated quark. More details about the hadronization process and jet structure
 336 will be given in chapter4.

337 In the first version of the quark model (1964), M. Gell-Mann [12] and G. Zweig
 338 [13, 14] developed a consistent way to classify hadrons according to their properties.
 339 Only three quarks (u, d, s) were involved in a scheme in which all baryons have baryon
 340 number $B=1$ and therefore quarks have $B=1/3$; non-baryons have $B=0$. Baryon
 341 number is conserved in SI and EI which means that single quarks cannot be created
 342 but in pairs $q - \bar{q}$.

343 The scheme organizes baryons in a two-dimensional space (I_3 - Y); Y (hyper-
 344 charge) and I_3 (isospin) are quantum numbers related by the Gell-Mann-Nishijima
 345 formula [15, 16]:

$$Q = I_3 + \frac{Y}{2} \quad (2.2)$$

346 where $Y = B + S + C + T + B'$ are the quantum numbers listed in Table 2.4.

347 There are six quark flavors organized in three generations (see Table 2.1) fol-
 348 lowing a mass hierarchy which, again, implies that higher generations decay to first
 349 generation quarks.

	Quarks			T_3	Y_W	Leptons			T_3	Y_W
Doublets	$(\frac{u}{d'})_L$	$(\frac{c}{s'})_L$	$(\frac{t}{b'})_L$	$(\frac{1/2}{-1/2})$	$1/3$	$(\nu_e)_L$	$(\nu_\mu)_L$	$(\nu_\tau)_L$	$(\frac{1/2}{-1/2})$	-1
Singlets	u_R	c_R	t_R	0	$4/3$	ν_{eR}	$\nu_{\mu R}$	$\nu_{\tau R}$		
	d'_R	s'_R	b'_R	0	$-2/3$	e_R	μ_R	τ_R	0	-2

Table 2.5: Fermion weak isospin and weak hypercharge multiplets. Weak hypercharge is calculated through the Gell-Mann-Nishijima formula 2.2 but using the weak isospin and charge for quarks.

351 Isospin doublets of quarks are also defined (see Table 2.5), and same as for neutrinos,
352 the WI eigenstates are not the same as the mass eigenstates which means that
353 members of different quark generations are connected by the WI mediator; thus, up-
354 type quarks are coupled not to down-type quarks (the mass eigenstates) directly but
355 to a superposition of down-type quarks (q'_d ; *the weak eigenstates*) via WI according
356 to:

$$q'_d = V_{CKM} q_d$$

357

$$\begin{pmatrix} d' \\ s' \\ b' \end{pmatrix} = \begin{pmatrix} V_{ud} & V_{us} & V_{ub} \\ V_{cd} & V_{cs} & V_{cb} \\ V_{td} & V_{ts} & V_{tb} \end{pmatrix} \begin{pmatrix} d \\ s \\ b \end{pmatrix} \quad (2.3)$$

358 where V_{CKM} is known as Cabibbo-Kobayashi-Maskawa (CKM) mixing matrix [17,18]
359 given by

$$\begin{pmatrix} |V_{ud}| & |V_{us}| & |V_{ub}| \\ |V_{cd}| & |V_{cs}| & |V_{cb}| \\ |V_{td}| & |V_{ts}| & |V_{tb}| \end{pmatrix} = \begin{pmatrix} 0.97427 \pm 0.00015 & 0.22534 \pm 0.00065 & 0.00351^{+0.00015}_{-0.00014} \\ 0.22520 \pm 0.00065 & 0.97344 \pm 0.00016 & 0.0412^{+0.0011}_{-0.0005} \\ 0.00867^{+0.00029}_{-0.00031} & 0.0404^{+0.0011}_{-0.0005} & 0.999146^{+0.000021}_{-0.000046} \end{pmatrix}. \quad (2.4)$$

360 The weak decays of quarks are represented in the diagram of Figure 2.2; again
361 the CKM matrix plays a central role since it contains the probabilities for the differ-

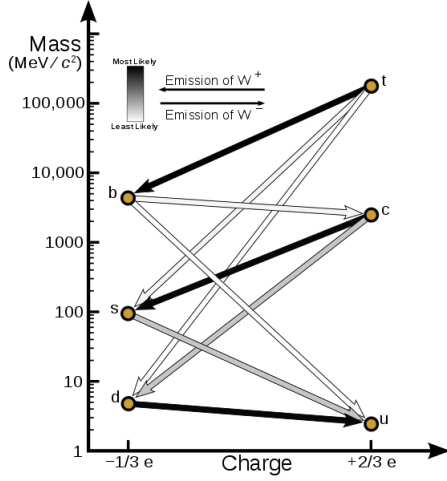


Figure 2.2: Transformations between quarks through the exchange of a WI. Higher generations quarks decay to first generation quarks by emitting a W boson. The arrow color indicates the likelihood of the transition according to the grey scale in the top left side which represent the CKM matrix parameters [19].

362 ent quark decay channels, in particular, note that quark decays are greatly favored
 363 between generation members.

364 CKM matrix is a 3×3 unitary matrix parametrized by three mixing angles and
 365 the *CP-mixing phase*; the latter is the parameter responsible for the Charge-Parity
 366 symmetry violation (CP-violation) in the SM. The fact that the top quark decays
 367 almost all the time to a bottom quark is exploited in this thesis when making the
 368 selection of the signal events by requiring the presence of a jet tagged as a jet coming
 369 from a *b* quark in the final state.

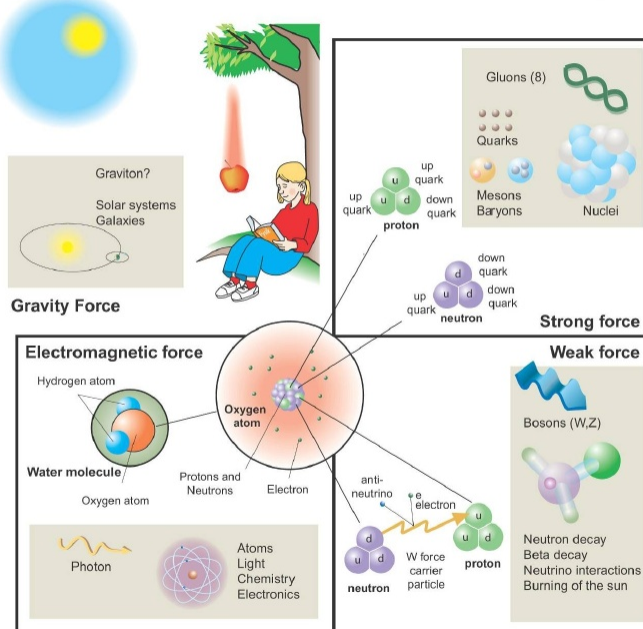
370 2.2.2 Fundamental interactions

371 Even though there are many manifestations of force in nature, like the ones repre-
 372 sented in Figure 2.3, we can classify all of them in four fundamental interactions:

- 373 • *Electromagnetic interaction (EI)* affects particles that are *electrically charged*,
 374 like electrons and protons. Figure 2.4a. shows a graphical representation, known

Fundamental interactions.

Illustration: Typoform



Summer School KPI 15 August 2009

Figure 2.3: Fundamental interactions in nature. Despite the many manifestations of forces in nature, we can track all of them back to one of the fundamental interactions. The most common forces are gravity and electromagnetic given that all of us are subject and experience them in everyday life.

375 as *Feynman diagram*, of electron-electron scattering.

- 376 • *Strong interaction (SI)* described by Quantum Chromodynamics (QCD). Hadrons
 377 like the proton and the neutron have internal structure given that they are com-
 378 posed of two or more valence quarks⁴. Quarks have fractional electric charge
 379 which means that they are subject to electromagnetic interaction and in the case
 380 of the proton they should break apart due to electrostatic repulsion; however,
 381 quarks are held together inside the hadrons against their electrostatic repulsion
 382 by the *Strong Force* through the exchange of *gluons*. The analog to the electric
 383 charge is the *color charge*. Electrons and photons are elementary particles as

⁴ Particles made of four and five quarks are exotic states not so common.

384 quarks but they don't carry color charge, therefore they are not subject to SI. A
 385 Feynman diagram for gluon exchange between quarks is shown in Figure 2.4b.

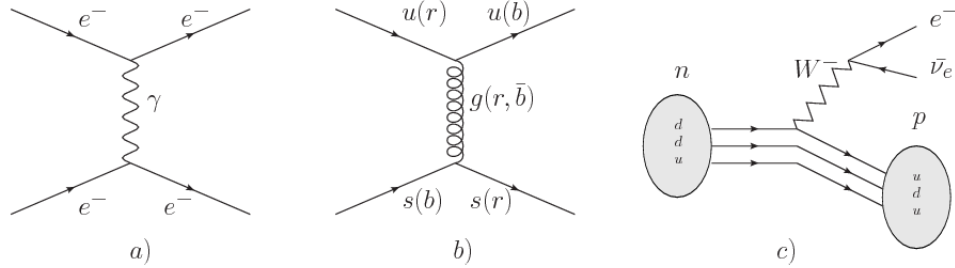


Figure 2.4: Feynman diagrams representing the interactions in SM; a) EI: e - e scattering; b) SI: gluon exchange between quarks ; c) WI: β -decay

386 • *Weak interaction (WI)* described by the weak theory (WT), is responsible, for
 387 instance, for the radioactive decay in atoms and the deuterium production
 388 within the sun. Quarks and leptons are the particles affected by the weak
 389 interaction; they possess a property called *flavor charge* (see 2.2.1) which can
 390 be changed by emitting or absorbing one weak force mediator. There are three
 391 mediators of the *weak force* known as Z boson in the case of electrically neutral
 392 flavor changes and W^\pm bosons in the case of electrically charged flavor changes.
 393 The *weak isospin* is the WI analog to electric charge in EI, and color charge in
 394 SI, and defines how quarks and leptons are affected by the weak force. Figure
 395 2.4c. shows the Feynman diagram of β -decay where a neutron (n) is transformed
 396 in a proton (p) by emitting a W^- particle.

397 • *Gravitational interaction (GI)* described by General Theory of Relativity (GR).
 398 It is responsible for the structure of galaxies and black holes as well as the
 399 expansion of the universe. As a classical theory, in the sense that it can be
 400 formulated without even appeal to the concept of quantization, it implies that
 401 the space-time is a continuum and predictions can be made without limitation

402 to the precision of the measurement tools. The latter represents a direct con-
 403 tradiction of the quantum mechanics principles. Gravity is deterministic while
 404 quantum mechanics is probabilistic; despite that, efforts to develop a quantum
 405 theory of gravity have predicted the *graviton* as mediator of the gravitational
 406 force⁵.

Interaction	Acts on	Relative strength	Range (m)	Mediators
Electromagnetic (QED)	Electrically charged particles	10^{-2}	Infinite	Photon
Strong (QCD)	Quarks and gluons	1	10^{-15}	Gluon
Weak (WI)	Leptons and quarks	10^{-6}	10^{-18}	W^\pm, Z
Gravitational (GI)	Massive particles	10^{-39}	Infinite	Graviton

Table 2.6: Fundamental interactions features [20].

407

408 Table 2.6 summarizes the main features of the fundamental interactions. The
 409 relative strength of the fundamental forces reveals the meaning of strong and weak;
 410 in a context where the relative strength of the SI is 1, the EI is about hundred times
 411 weaker and WI is about million times weaker than the SI. A good description on how
 412 the relative strength and range of the fundamental interactions are calculated can
 413 be found in References [20, 21]. In the everyday life, only EI and GI are explicitly
 414 experienced due to the range of these interactions; i.e., at the human scale distances
 415 only EI and GI have appreciable effects, in contrast to SI which at distances greater
 416 than 10^{-15} m become negligible.

417 2.2.3 Gauge invariance.

418 QED was built successfully on the basis of the classical electrodynamics theory (CED)
 419 of Maxwell and Lorentz, following theoretical and experimental requirements imposed

⁵ Actually a wide variety of theories have been developed in an attempt to describe gravity; some famous examples are string theory and supergravity.

420 by

- 421 • Lorentz invariance: independence on the reference frame.
- 422 • Locality: interacting fields are evaluated at the same space-time point to avoid
423 action at a distance.
- 424 • Renormalizability: physical predictions are finite and well defined.
- 425 • Particle spectrum, symmetries and conservation laws already known must emerge
426 from the theory.
- 427 • Local gauge invariance.

428 The gauge invariance requirement reflects the fact that the fundamental fields
429 cannot be directly measured but associated fields which are the observables. Electric
430 (**E**) and magnetic (**B**) fields in CED are associated with the electric scalar potential
431 V and the vector potential **A**. In particular, **E** can be obtained by measuring the
432 change in the space of the scalar potential (ΔV); however, two scalar potentials
433 differing by a constant f correspond to the same electric field. The same happens
434 in the case of the vector potential **A**; thus, different configurations of the associated
435 fields result in the same set of values of the observables. The freedom in choosing one
436 particular configuration is known as *gauge freedom*; the transformation law connecting
437 two configurations is known as *gauge transformation* and the fact that the observables
438 are not affected by a gauge transformation is called *gauge invariance*.

439 When the gauge transformation:

$$\begin{aligned} \mathbf{A} &\rightarrow \mathbf{A} - \Delta f \\ V &\rightarrow V - \frac{\partial f}{\partial t} \end{aligned} \tag{2.5}$$

440 is applied to Maxwell equations, they are still satisfied and the fields remain invariant.
 441 Thus, CED is invariant under gauge transformations and is called a *gauge theory*.
 442 The set of all gauge transformations form the *symmetry group* of the theory, which
 443 according to the group theory, has a set of *group generators*. The number of group
 444 generators determine the number of *gauge fields* of the theory.

445 As mentioned in the first lines of Section 2.2, QED has one symmetry group ($U(1)$)
 446 with one group generator (the Q operator) and one gauge field (the electromagnetic
 447 field A^μ). In CED there is not a clear definition, beyond the historical convention,
 448 of which fields are the fundamental and which are the associated, but in QED the
 449 fundamental field is A^μ . When a gauge theory is quantized, the gauge fields are
 450 quantized and their quanta are called *gauge bosons*. The word boson characterizes
 451 particles with integer spin which obey Bose-Einstein statistics.

452 As will be detailed in Section 2.3, interactions between particles in a system can
 453 be obtained by considering first the Lagrangian density of free particles in the sys-
 454 tem, which of course is incomplete because the interaction terms have been left out,
 455 and demanding global phase transformation invariance. Global phase transforma-
 456 tion means that a gauge transformation is performed identically to every point
 457 in the space⁶ and the Lagrangian remains invariant. Then, the global transforma-
 458 tion is promoted to a local phase transformation (this time the gauge transformation
 459 depends on the position in space) and again invariance is required.

⁶ Here space corresponds to the 4-dimensional space i.e. space-time.

460 Due to the space dependence of the local transformation, the Lagrangian density is
 461 not invariant anymore. In order to reinstate the gauge invariance, the gauge covariant
 462 derivative is introduced in the Lagrangian and with it the gauge field responsible for
 463 the interaction between particles in the system. The new Lagrangian density is gauge
 464 invariant, includes the interaction terms needed to account for the interactions and
 465 provides a way to explain the interaction between particles through the exchange of
 466 the gauge boson.

467 This recipe was used to build QED and the theories that aim to explain the
 468 fundamental interactions.

469 2.2.4 Gauge bosons

470 The importance of the gauge bosons comes from the fact that they are the force
 471 mediators or force carriers. The features of the gauge bosons reflect those of the fields
 472 they represent and they are extracted from the Lagrangian density used to describe
 473 the interactions. In Section 2.3, it will be shown how the gauge bosons of the EI and
 474 WI emerge from the electroweak Lagrangian. The SI gauge bosons features are also
 475 extracted from the SI Lagrangian but it is not detailed in this document. The main
 476 features of the SM gauge bosons will be briefly presented below and summarized in
 477 Table 2.7.

- 478 • **Photon.** EI occurs when the photon couples to (is exchanged between) parti-
 479 cles carrying electric charge; however, The photon itself does not carry electric
 480 charge, therefore, there is no coupling between photons. Given that the photon
 481 is massless the EI is of infinite range, i.e., electrically charged particles interact
 482 even if they are located far away one from each other; this also implies that
 483 photons always move with the speed of light.

- 484 • **Gluon.** SI is mediated by gluons which just as photons are massless. They
 485 carry one unit of color charge and one unit of anticolor charge, hence, gluons
 486 can couple to other gluons. As a result, the range of the SI is not infinite
 487 but very short due to the attraction between gluons, giving rise to the *color*
 488 *confinement* which explains why color charged particles cannot be isolated but
 489 live within composite particles, like quarks inside protons.
- 490 • **W, Z.** W^\pm and Z, are massive which explains their short-range. Given that
 491 the WI is the only interaction that can change the flavor of the interacting
 492 particles, the W boson is the responsible for the nuclear transmutation where
 493 a neutron is converted into a proton or vice versa with the involvement of an
 494 electron and a neutrino (see Figure 2.4c). The Z boson is the responsible for the
 495 neutral weak processes like neutrino elastic scattering where no electric charge
 496 but momentum transference is involved. WI gauge bosons carry isospin charge
 497 which makes interaction between them possible.

Interaction	Mediator	Electric charge (e)	Color charge	Weak Isospin	mass (GeV/c ²)
Electromagnetic	Photon (γ)	0	No	0	0
Strong	Gluon (g)	0	Yes -octet	No	0
Weak	W^\pm	± 1	No	± 1	80.385 ± 0.015
	Z	0	No	0	91.188 ± 0.002

Table 2.7: SM gauge bosons main features [9].

498

499 **2.3 Electroweak unification and the Higgs
 500 mechanism**

501 Physicists dream of building a theory that contains all the interactions in one single
 502 interaction, i.e., showing that at some scale in energy all the four fundamental inter-

actions are unified and only one interaction emerges in a *Theory of everything*. The first sign of the feasibility of such unification came from success in the construction of the CED. Einstein spent years trying to reach that full unification, which by 1920 only involved electromagnetism and gravity, with no success; however, a new partial unification was achieved in the 1960's, when S.Glashow [22], A.Salam [23] and S.Weinberg [24] independently proposed that electromagnetic and weak interactions are two manifestations of a more general interaction called *electroweak interaction* (EWI). EWI was developed by following the useful prescription provided by QED and the gauge invariance principles.

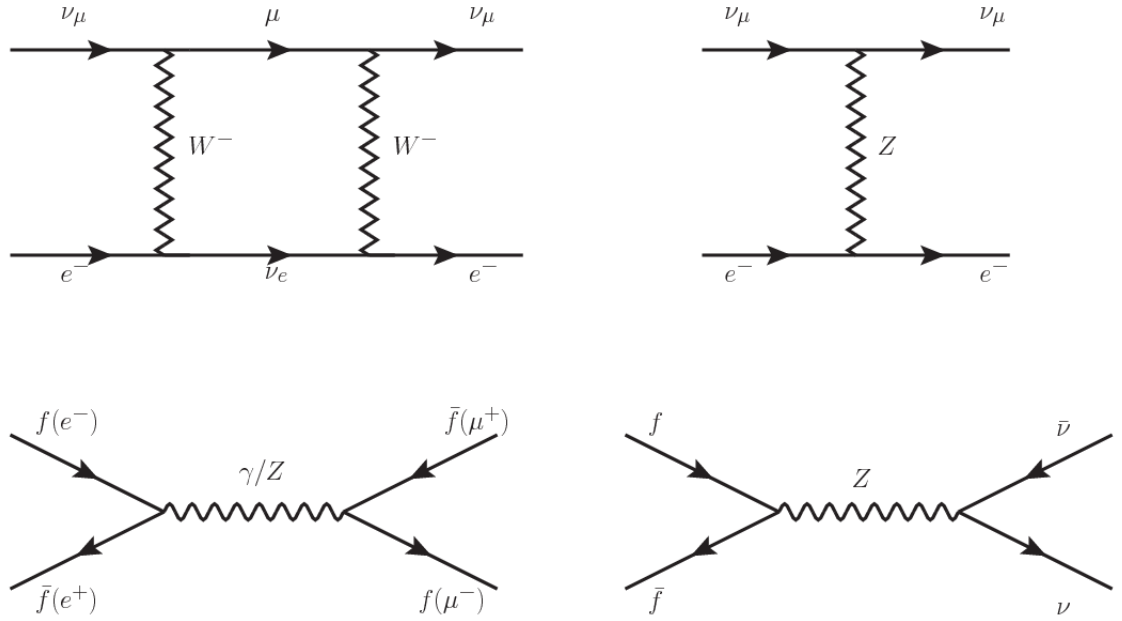


Figure 2.5: Top: $\nu_\mu - e^-$ scattering going through charged currents (left) and neutral currents (right). Bottom: neutral current processes for charged fermions (left) and involving neutrinos (right). While neutral current processes involving only charged fermions can proceed through EI or WI, those involving neutrinos can only proceed via WI.

The *classic* weak theory developed by Fermi, did not have the concept of the W boson but instead it was treated as a point interaction with the dimensionful constant G_F associated with it. It works really well at low energies very far off the W mass

515 shell. When going up in energy, the theory of weak interactions involving the W
 516 boson is capable of explaining the β -decay and in general the processes mediated by
 517 W^\pm bosons. However, there were some processes like the $\nu_\mu - e$ scattering which
 518 would require the exchange of two W bosons (see Figure 2.5 top diagrams) giving
 519 rise to divergent loop integrals and then non-finite predictions. The EWI theory, by
 520 including neutral currents involving fermions via the exchange of a neutral bosons Z,
 521 overcomes those divergences and the predictions become realistic.

522 Neutral weak interaction vertices conserve flavor in the same way as the electro-
 523 magnetic vertices do, but additionally, the Z boson can couple to neutrinos which
 524 implies that processes involving charged fermions can proceed through EI or WI but
 525 processes involving neutrinos can proceed only through WI.

526 The prescription to build a gauge theory of the WI consists of proposing a free
 527 field Lagrangian density that includes the particles involved; next, by requesting
 528 invariance under global phase transformations first and generalizing to local phase
 529 transformations invariance later, the conserved currents are identified and interactions
 530 are generated by introducing gauge fields. Given that the goal is to include the EI
 531 and WI in a single theory, the group symmetry considered should be a combination of
 532 $SU(2)_L$ and $U(1)_{em}$, however the latter cannot be used directly because the EI treats
 533 left and right-handed particles indistinctly in contrast to the former. Fortunately, the
 534 weak hypercharge, which is a combination of the weak isospin and the electric charge
 535 (Eqn. 2.2) is suitable to be used since it is conserved by the EI and WI. Thus, the
 536 symmetry group to be considered is

$$G \equiv SU(2)_L \otimes U(1)_Y \quad (2.6)$$

537 The following treatment applies to any of the fermion generations, but for sim-

538 plicity the first generation of leptons will be considered [5, 6, 25, 26].

539 Given the first generation of leptons

$$\psi_1 = \begin{pmatrix} \nu_e \\ e^- \end{pmatrix}_L, \quad \psi_2 = \nu_{eR}, \quad \psi_3 = e_R^- \quad (2.7)$$

540 the charged fermionic currents are given by

$$J_\mu \equiv J_\mu^+ = \bar{\nu}_{eL} \gamma_\mu e_L, \quad J_\mu^\dagger \equiv J_\mu^- = \bar{e}_L \gamma_\mu \nu_{eL} \quad (2.8)$$

541 and the free Lagrangian is given by

$$\mathcal{L}_0 = \sum_{j=1}^3 i\bar{\psi}_j(x) \gamma^\mu \partial_\mu \psi_j(x). \quad (2.9)$$

542 Mass terms are included directly in the QED free Lagrangians since they preserve
 543 the invariance under the symmetry transformations involved which treat left and right
 544 handed particles similarly, however mass terms of the form

$$m_W^2 W_\mu^\dagger(x) W^\mu(x) + \frac{1}{2} m_Z^2 Z_\mu(x) Z^\mu(x) - m_e \bar{\psi}_e(x) \psi_e(x) \quad (2.10)$$

545 which represent the mass of W^\pm , Z and electrons, are not invariant under G trans-
 546 formations, therefore the gauge fields described by the EWI are in principle massless.

547 Experiments have shown that the EWI gauge fields are not massless [27–30];
 548 however, they have to acquire mass through a mechanism compatible with the gauge
 549 invariance; that mechanism is known as the *Higgs mechanism* and will be considered
 550 later in this Section. The global transformations in the combined symmetry group G
 551 can be written as

$$\begin{aligned}
\psi_1(x) &\xrightarrow{G} \psi'_1(x) \equiv U_Y U_L \psi_1(x), \\
\psi_2(x) &\xrightarrow{G} \psi'_2(x) \equiv U_Y \psi_2(x), \\
\psi_3(x) &\xrightarrow{G} \psi'_3(x) \equiv U_Y \psi_3(x)
\end{aligned} \tag{2.11}$$

552 where U_L represent the $SU(2)_L$ transformation acting only on the weak isospin dou-
 553 blet and U_Y represent the $U(1)_Y$ transformation acting on all the weak isospin mul-
 554 tiplets. Explicitly

$$U_L \equiv \exp\left(i \frac{\sigma_i}{2} \alpha^i\right), \quad U_Y \equiv \exp(i y_i \beta) \quad (i = 1, 2, 3) \tag{2.12}$$

555 with σ_i the Pauli matrices and y_i the weak hypercharges. In order to promote the
 556 transformations from global to local while keeping the invariance, it is required that
 557 $\alpha^i = \alpha^i(x)$, $\beta = \beta(x)$ and the replacement of the ordinary derivatives by the covariant
 558 derivatives

$$\begin{aligned}
D_\mu \psi_1(x) &\equiv \left[\partial_\mu + ig\sigma_i W_\mu^i(x)/2 + ig'y_1 B_\mu(x) \right] \psi_1(x) \\
D_\mu \psi_2(x) &\equiv \left[\partial_\mu + ig'y_2 B_\mu(x) \right] \psi_2(x) \\
D_\mu \psi_3(x) &\equiv \left[\partial_\mu + ig'y_3 B_\mu(x) \right] \psi_3(x)
\end{aligned} \tag{2.13}$$

559 introducing in this way four gauge fields, $W_\mu^i(x)$ and $B_\mu(x)$, in the process. The
 560 covariant derivatives (Eqn. 2.13) are required to transform in the same way as fermion
 561 fields $\psi_i(x)$ themselves, therefore, the gauge fields transform as:

$$\begin{aligned} B_\mu(x) &\xrightarrow{G} B'_\mu(x) \equiv B_\mu(x) - \frac{1}{g'} \partial_\mu \beta(x) \\ W_\mu^i(x) &\xrightarrow{G} W_\mu^{i\prime}(x) \equiv W_\mu^i(x) - \frac{i}{g} \partial_\mu \alpha_i(x) - \varepsilon_{ijk} \alpha_i(x) W_\mu^j(x). \end{aligned} \quad (2.14)$$

562 The G invariant version of the Lagrangian density 2.9 can be written as

$$\mathcal{L}_0 = \sum_{j=1}^3 i \bar{\psi}_j(x) \gamma^\mu D_\mu \psi_j(x) \quad (2.15)$$

563 where free massless fermion and gauge fields and fermion-gauge boson interactions
 564 are included. The EWI Lagrangian density must additionally include kinetic terms
 565 for the gauge fields (\mathcal{L}_G) which are built from the field strengths, according to

$$B_{\mu\nu}(x) \equiv \partial_\mu B_\nu - \partial_\nu B_\mu \quad (2.16)$$

$$W_{\mu\nu}^i(x) \equiv \partial_\mu W_\nu^i(x) - \partial_\nu W_\mu^i(x) - g \varepsilon^{ijk} W_\mu^j W_\nu^k \quad (2.17)$$

566 the last term in Eqn. 2.17 is added in order to hold the gauge invariance; therefore,

$$\mathcal{L}_G = -\frac{1}{4} B_{\mu\nu}(x) B^{\mu\nu}(x) - \frac{1}{4} W_{\mu\nu}^i(x) W_i^{\mu\nu}(x) \quad (2.18)$$

567 which contains not only the free gauge fields contributions, but also the gauge fields
 568 self-interactions and interactions among them.

569 The three weak isospin conserved currents resulting from the $SU(2)_L$ symmetry
 570 are given by

$$J_\mu^i(x) = \frac{1}{2} \bar{\psi}_1(x) \gamma_\mu \sigma^i \psi_1(x) \quad (2.19)$$

571 while the weak hypercharge conserved current resulting from the $U(1)_Y$ symmetry is
 572 given by

$$J_\mu^Y = \sum_{j=1}^3 \bar{\psi}_j(x) \gamma_\mu y_j \psi_j(x) \quad (2.20)$$

573 In order to evaluate the electroweak interactions modeled by an isos triplet field
 574 W_μ^i that couples to isospin currents J_μ^i with strength g and additionally the singlet
 575 field B_μ which couples to the weak hypercharge current J_μ^Y with strength $g'/2$. The
 576 interaction Lagrangian density to be considered is

$$\mathcal{L}_I = -g J^{i\mu}(x) W_\mu^i(x) - \frac{g'}{2} J^{Y\mu}(x) B_\mu(x) \quad (2.21)$$

577 Note that the weak isospin currents are not the same as the charged fermionic cur-
 578 rents that were used to describe the WI (Eqn. 2.8), since the weak isospin eigenstates
 579 are not the same as the mass eigenstates, but they are closely related

$$J_\mu = \frac{1}{2}(J_\mu^1 + iJ_\mu^2), \quad J_\mu^\dagger = \frac{1}{2}(J_\mu^1 - iJ_\mu^2). \quad (2.22)$$

580 The same happens with the gauge fields W_μ^i which are related to the mass eigen-
 581 states W^\pm by

$$W_\mu^+ = \frac{1}{\sqrt{2}}(W_\mu^1 - iW_\mu^2), \quad W_\mu^- = \frac{1}{\sqrt{2}}(W_\mu^1 + iW_\mu^2). \quad (2.23)$$

582 The fact that there are three weak isospin conserved currents is an indication that
 583 in addition to the charged fermionic currents, which couple charged to neutral leptons,
 584 there should be a neutral fermionic current that does not involve electric charge
 585 exchange; therefore, it couples neutral fermions or fermions of the same electric charge.
 586 The third weak isospin current contains a term that is similar to the electromagnetic

587 current (j_μ^{em}), indicating that there is a relation between them and resembling the
 588 Gell-Mann-Nishijima formula 2.2 adapted to electroweak interactions

$$Q = T_3 + \frac{Y_W}{2}. \quad (2.24)$$

589 Just as Q generates the $U(1)_{em}$ symmetry, the weak hypercharge generates the
 590 $U(1)_Y$ symmetry as said before. It is possible to write the relationship in terms of
 591 the currents as

$$j_\mu^{em} = J_\mu^3 + \frac{1}{2} J_\mu^Y. \quad (2.25)$$

592 The neutral gauge fields W_μ^3 and B_μ cannot be directly identified with the Z
 593 and the photon fields since the photon interacts similarly with left and right-handed
 594 fermions; however, they are related through a linear combination given by

$$\begin{aligned} A_\mu &= B_\mu \cos \theta_W + W_\mu^3 \sin \theta_W \\ Z_\mu &= -B_\mu \sin \theta_W + W_\mu^3 \cos \theta_W \end{aligned} \quad (2.26)$$

where θ_W is known as the *Weinberg angle*. The interaction Lagrangian is now given by

$$\begin{aligned} \mathcal{L}_I = -\frac{g}{\sqrt{2}}(J^\mu W_\mu^+ + J^{\mu\dagger} W_\mu^-) - &\left(g \sin \theta_W J_\mu^3 + g' \cos \theta_W \frac{J_\mu^Y}{2}\right) A^\mu \\ &- \left(g \cos \theta_W J_\mu^3 - g' \sin \theta_W \frac{J_\mu^Y}{2}\right) Z^\mu \end{aligned} \quad (2.27)$$

595 the first term is the weak charged current interaction, while the second term is the

596 electromagnetic interaction under the condition

$$g \sin \theta_W = g' \cos \theta_W = e, \quad \frac{g'}{g} = \tan \theta_W \quad (2.28)$$

597 contained in the Eqn.2.25; the third term is the neutral weak current.

598

599 Note that the neutral fields transformation given by the Eqn. 2.26 can be written
600 in terms of the coupling constants g and g' as:

$$A_\mu = \frac{g' W_\mu^3 + g B_\mu}{\sqrt{g^2 + g'^2}}, \quad Z_\mu = \frac{g W_\mu^3 - g' B_\mu}{\sqrt{g^2 + g'^2}}. \quad (2.29)$$

601 So far, the Lagrangian density describing the non-massive EWI is:

$$\mathcal{L}_{nmEWI} = \mathcal{L}_0 + \mathcal{L}_G \quad (2.30)$$

602 where fermion and gauge fields have been considered massless because their regular
603 mass terms are manifestly non invariant under G transformations; therefore, masses
604 have to be generated in a gauge invariant way. The mechanism by which this goal is
605 achieved is known as the *Higgs mechanism* and is closely connected to the concept of
606 *spontaneous symmetry breaking*.

607 2.3.1 Spontaneous symmetry breaking (SSB)

608 Figure 2.6 left shows a steel nail (top) which is subject to an external force; the form
609 of the potential energy is also shown (bottom).

610 Before reaching the critical force value, the system has rotational symmetry with
611 respect to the nail axis; however, after the critical force value is reached the nail buck-

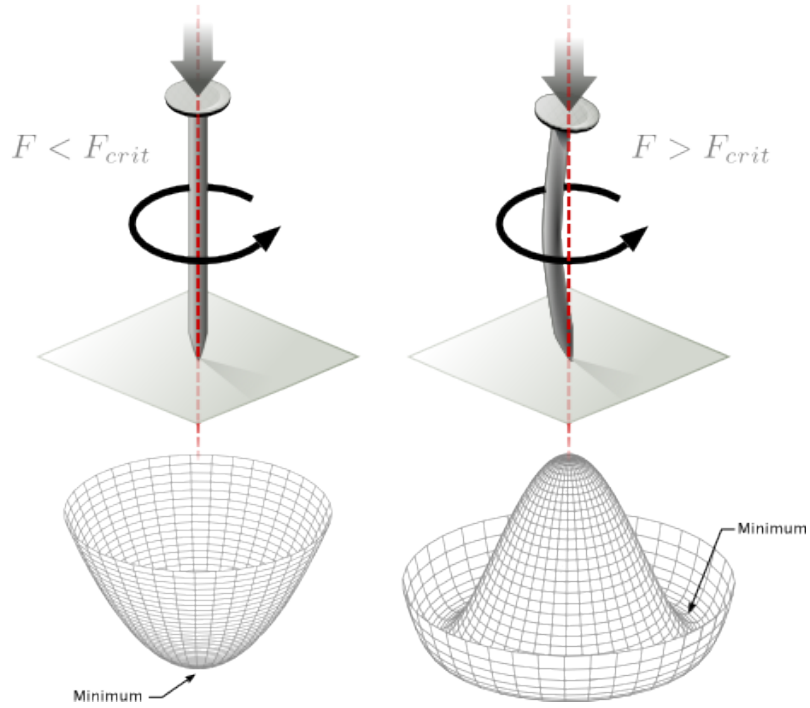


Figure 2.6: Spontaneous symmetry breaking mechanism. The steel nail, subject to an external force (top left), has rotational symmetry with respect to its axis. When the external force overcomes a critical value the nail buckles (top right) choosing a minimal energy state (ground state) and thus *breaking spontaneously the rotational symmetry*. The potential energy (bottom) changes but holds the rotational symmetry; however, an infinite number of asymmetric ground states are generated and circularly distributed in the bottom of the potential [31].

612 les (top right). The form of the potential energy (bottom right) changes appearing a
 613 set of infinity minima but preserving its rotational symmetry. Right before the nail
 614 buckles there is no indication of the direction the nail will bend because any of the
 615 directions are equivalent, but once the nail bends, choosing a direction, an arbitrary
 616 minimal energy state (ground state) is selected and it does not share the system's
 617 rotational symmetry. This mechanism for reaching an asymmetric ground state is
 618 known as *spontaneous symmetry breaking*.

619 The lesson from this analysis is that the way to introduce the SSB mechanism
 620 into a system is by adding the appropriate potential to it.

621 Figure 2.7 shows a plot of the potential $V(\phi)$ in the case of a scalar field ϕ

$$V(\phi) = \mu^2 \phi^\dagger \phi + \lambda (\phi^\dagger \phi)^2 \quad (2.31)$$

622 If $\mu^2 > 0$ the potential has only one minimum at $\phi = 0$ and describes a scalar field
 623 with mass μ . If $\mu^2 < 0$ the potential has a local maximum at $\phi = 0$ and two minima
 624 at $\phi = \pm\sqrt{-\mu^2/\lambda}$ which enables the SSB mechanism to work.

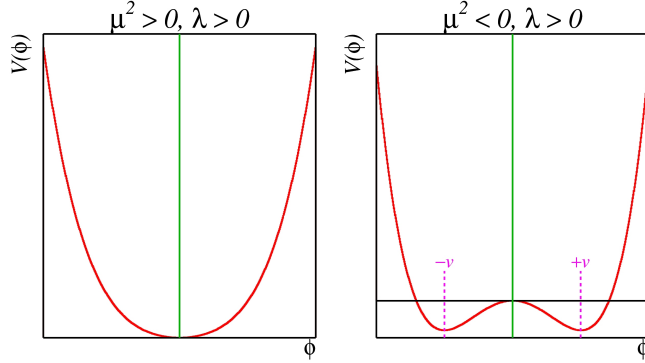


Figure 2.7: Shape of the potential $V(\phi)$ for $\lambda > 0$ and: $\mu^2 > 0$ (left) and $\mu^2 < 0$ (right). The case $\mu^2 < 0$ corresponds to the potential suitable for introducing the SSB mechanism by choosing one of the two ground states which are connected via reflection symmetry. [31].

625 In the case of a complex scalar field $\phi(x)$

$$\phi(x) = \frac{1}{\sqrt{2}}(\phi_1 + i\phi_2) \quad (2.32)$$

626 the Lagrangian (invariant under global $U(1)$ transformations) is given by

$$\mathcal{L} = (\partial_\mu \phi)^\dagger (\partial^\mu \phi) - V(\phi), \quad V(\phi) = \mu^2 \phi^\dagger \phi + \lambda (\phi^\dagger \phi)^2 \quad (2.33)$$

627 where an appropriate potential has been added in order to introduce the SSB.

628 As seen in Figure 2.8, the potential has now an infinite number of minima circularly
 629 distributed along the ξ -direction which makes possible the occurrence of the SSB by
 630 choosing an arbitrary ground state; for instance, $\xi = 0$, i.e. $\phi_1 = v, \phi_2 = 0$

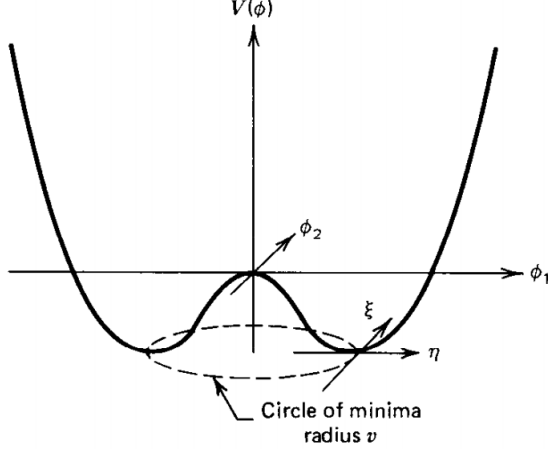


Figure 2.8: Potential for complex scalar field. There is a circle of minima of radius v along the ξ -direction [6].

$$\phi_0 = \frac{v}{\sqrt{2}} \exp(i\xi) \quad \xrightarrow{\text{SSB}} \quad \phi_0 = \frac{v}{\sqrt{2}} \quad (2.34)$$

631 As usual, excitations over the ground state are studied by making an expansion
 632 about it; thus, the excitations can be parametrized as:

$$\phi(x) = \frac{1}{\sqrt{2}}(v + \eta(x) + i\xi(x)) \quad (2.35)$$

633 which when substituted into Eqn. 2.33 produces a Lagrangian in terms of the new
 634 fields η and ξ

$$\mathcal{L}' = \frac{1}{2}(\partial_\mu \xi)^2 + \frac{1}{2}(\partial_\mu \eta)^2 + \mu^2 \eta^2 - V(\phi_0) - \lambda v \eta (\eta^2 + \xi^2) - \frac{\lambda}{4}(\eta^2 + \xi^2)^2 \quad (2.36)$$

635 where the last two terms represent the interactions and self-interaction between the
 636 two fields η and ξ . The particular feature of the SSB mechanism is revealed when
 637 looking to the first three terms of \mathcal{L}' . Before the SSB, only the massless ϕ field is

638 present in the system; after the SSB there are two fields of which the η -field has
 639 acquired mass $m_\eta = \sqrt{-2\mu^2}$ while the ξ -field is still massless (see Figure 2.9).

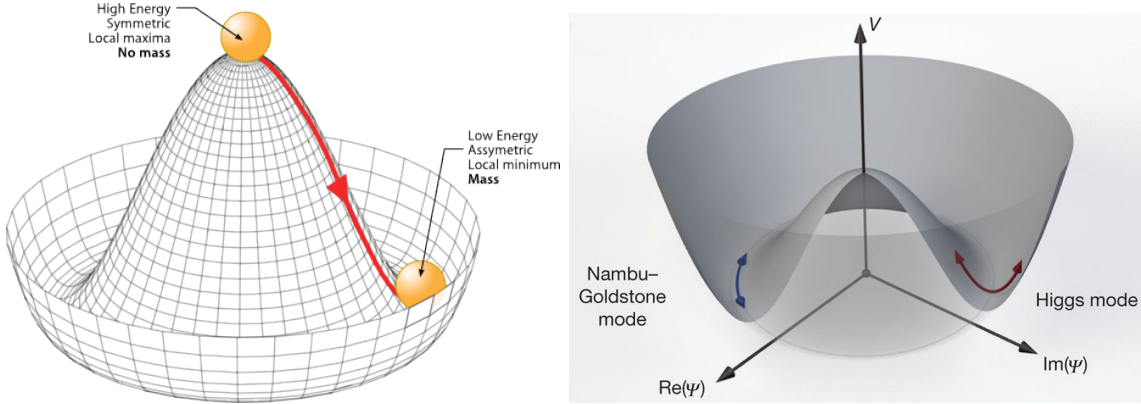


Figure 2.9: SSB mechanism for a complex scalar field [31, 32].

640 Thus, the SSB mechanism serves as a method to generate mass but as a side ef-
 641 fect a massless field is introduced in the system. This fact is known as the Goldstone
 642 theorem and states that a massless scalar field appears in the system for each con-
 643 tinuous symmetry spontaneously broken. Another version of the Goldstone theorem
 644 states that “if a Lagrangian is invariant under a continuous symmetry group G , but
 645 the vacuum is only invariant under a subgroup $H \subset G$, then there must exist as many
 646 massless spin-0 particles (Nambu-Goldstone bosons) as broken generators.” [26] The
 647 Nambu-Goldstone boson can be understood considering that the potential in the ξ -
 648 direction is flat so excitations in that direction are not energy consuming and thus
 649 represent a massless state.

650 2.3.2 Higgs mechanism

651 When the SSB mechanism is introduced in the formulation of the EWI in an attempt
 652 to generate the mass of the so far massless gauge bosons and fermions, an interesting
 653 effect is revealed. In order to keep the G symmetry group invariance and generate

654 the mass of the EW gauge bosons, a G invariant Lagrangian density (\mathcal{L}_S) has to be
 655 added to the non massive EWI Lagrangian (Eqn. 2.30)

$$\mathcal{L}_S = (D_\mu \phi)^\dagger (D^\mu \phi) - \mu^2 \phi^\dagger \phi - \lambda (\phi^\dagger \phi)^2, \quad \lambda > 0, \mu^2 < 0 \quad (2.37)$$

$$D_\mu \phi = \left(i\partial_\mu - g \frac{\sigma_i}{2} W_\mu^i - g' \frac{Y}{2} B_\mu \right) \phi \quad (2.38)$$

656 ϕ has to be an isospin doublet of complex scalar fields so it preserves the G invariance;
 657 thus ϕ can be defined as:

$$\phi = \begin{pmatrix} \phi^+ \\ \phi^0 \end{pmatrix} \equiv \frac{1}{\sqrt{2}} \begin{pmatrix} \phi_1 + i\phi_2 \\ \phi_3 + i\phi_4 \end{pmatrix}. \quad (2.39)$$

658 The minima of the potential are defined by

$$\phi^\dagger \phi = \frac{1}{2} (\phi_1^2 + \phi_2^2 + \phi_3^2 + \phi_4^2) = -\frac{\mu^2}{2\lambda}. \quad (2.40)$$

659 The choice of the ground state is critical. By choosing a ground state, invariant
 660 under $U(1)_{em}$ gauge symmetry, the photon will remain massless and the W^\pm and Z
 661 bosons masses will be generated which is exactly what is needed. In that sense, the
 662 best choice corresponds to a weak isospin doublet with $T_3 = -1/2$, $Y_W = 1$ and $Q = 0$
 663 which defines a ground state with $\phi_1 = \phi_2 = \phi_4$ and $\phi_3 = v$:

$$\phi_0 \equiv \frac{1}{\sqrt{2}} \begin{pmatrix} 0 \\ v \end{pmatrix}, \quad v^2 \equiv -\frac{\mu^2}{\lambda}. \quad (2.41)$$

664 where the vacuum expectation value v is fixed by the Fermi coupling G_F according
 665 to $v = (\sqrt{2}G_F)^{1/2} \approx 246$ GeV.

666 The G symmetry has been broken and three Nambu-Goldstone bosons will appear.

667 The next step is to expand ϕ about the chosen ground state as:

$$\phi(x) = \frac{1}{\sqrt{2}} \exp\left(\frac{i}{v} \sigma_i \theta^i(x)\right) \begin{pmatrix} 0 \\ v + H(x) \end{pmatrix} \approx \frac{1}{\sqrt{2}} \begin{pmatrix} \theta_1(x) + i\theta_2(x) \\ v + H(x) - i\theta_3(x) \end{pmatrix} \quad (2.42)$$

668 to describe fluctuations from the ground state ϕ_0 . The fields $\theta_i(x)$ represent the
 669 Nambu-Goldstone bosons while $H(x)$ is known as *Higgs field*. The fundamental fea-
 670 ture of the parametrization used is that the dependence on the $\theta_i(x)$ fields is factored
 671 out in a global phase that can be eliminated by taking the physical *unitary gauge*
 672 $\theta_i(x) = 0$. Therefore the expansion about the ground state is given by:

$$\phi(x) \frac{1}{\sqrt{2}} \begin{pmatrix} 0 \\ v + H(x) \end{pmatrix} \quad (2.43)$$

673 which when substituted into \mathcal{L}_S (Eqn. 2.37) results in a Lagrangian containing the
 674 now massive three gauge bosons W^\pm, Z , one massless gauge boson (photon) and
 675 the new Higgs field (H). The three degrees of freedom corresponding to the Nambu-
 676 Goldstone bosons are now integrated into the massive gauge bosons as their lon-
 677 gitudinal polarizations which were not available when they were massless particles.
 678 The effect by which vector boson fields acquire mass after an spontaneous symmetry
 679 breaking, but without an explicit gauge invariance breaking is known as the *Higgs*
 680 *mechanism*.

681 The mechanism was proposed by three independent groups: F.Englert and R.Brout
 682 in August 1964 [33], P.Higgs in October 1964 [34] and G.Guralnik, C.Hagen and
 683 T.Kibble in November 1964 [35]; however, its importance was not realized until
 684 S.Glashow [22], A.Salam [23] and S.Weinberg [24], independently, proposed that elec-
 685 tromagnetic and weak interactions are two manifestations of a more general interac-
 686 tion called *electroweak interaction* in 1967.

687 **2.3.3 Masses of the gauge bosons**

688 The masses of the gauge bosons are extracted by evaluating the kinetic part of La-
 689 grangian \mathcal{L}_S in the ground state (known also as the vacuum expectation value), i.e.,

$$\left| \left(\partial_\mu - ig \frac{\sigma_i}{2} W_\mu^i - i \frac{g'}{2} B_\mu \right) \phi_0 \right|^2 = \left(\frac{1}{2} v g \right)^2 W_\mu^+ W^{-\mu} + \frac{1}{8} v^2 (W_\mu^3, B_\mu) \begin{pmatrix} g^2 & -gg' \\ -gg' & g'^2 \end{pmatrix} \begin{pmatrix} W^{3\mu} \\ B^\mu \end{pmatrix} \quad (2.44)$$

690 comparing with the typical mass term for a charged boson $M_W^2 W^+ W^-$

$$M_W = \frac{1}{2} v g. \quad (2.45)$$

The second term in the right side of the Eqn.2.44 comprises the masses of the neutral bosons, but it needs to be written in terms of the gauge fields Z_μ and A_μ in order to be compared to the typical mass terms for neutral bosons, therefore using Eqn. 2.29

$$\begin{aligned} \frac{1}{8} v^2 [g^2 (W_\mu^3)^2 - 2gg' W_\mu^3 B^\mu + g'^2 B_\mu^2] &= \frac{1}{8} v^2 [g W_\mu^3 - g' B_\mu]^2 + 0[g' W_\mu^3 + g B_\mu]^2 \quad (2.46) \\ &= \frac{1}{8} v^2 [\sqrt{g^2 + g'^2} Z_\mu]^2 + 0[\sqrt{g^2 + g'^2} A_\mu]^2 \end{aligned}$$

691 and then

$$M_Z = \frac{1}{2} v \sqrt{g^2 + g'^2}, \quad M_A = 0 \quad (2.47)$$

692 **2.3.4 Masses of the fermions**

693 The lepton mass terms can be generated by introducing a gauge invariant Lagrangian
 694 term describing the Yukawa coupling between the lepton field and the Higgs field

$$\mathcal{L}_{Yl} = -G_l \left[(\bar{\nu}_l, \bar{l})_L \begin{pmatrix} \phi^+ \\ \phi^0 \end{pmatrix} l_R + \bar{l}_R (\phi^-, \bar{\phi}^0) \begin{pmatrix} \nu_l \\ l \end{pmatrix} \right], \quad l = e, \mu, \tau. \quad (2.48)$$

695 After the SSB and replacing the usual field expansion about the ground state
 696 (Eqn.2.41) into \mathcal{L}_{Yl} , the mass term arises

$$\mathcal{L}_{Yl} = -m_l (\bar{l}_L l_R + \bar{l}_R l_L) - \frac{m_l}{v} (\bar{l}_L l_R + \bar{l}_R l_L) H = -m_l \bar{l} \left(1 + \frac{H}{v} \right) \quad (2.49)$$

697

$$m_l = \frac{G_l}{\sqrt{2}} v \quad (2.50)$$

698 where the additional term represents the lepton-Higgs interaction. The quark masses
 699 are generated in a similar way as lepton masses but for the upper member of the
 700 quark doublet a different Higgs doublet is needed:

$$\phi_c = -i\sigma_2 \phi^* = \begin{pmatrix} -\bar{\phi}^0 \\ \phi^- \end{pmatrix}. \quad (2.51)$$

701 Additionally, given that the quark isospin doublets are not constructed in terms
 702 of the mass eigenstates but in terms of the flavor eigenstates, as shown in Table 2.5,
 703 the coupling parameters will be related to the CKM matrix elements; thus the quark
 704 Lagrangian is given by:

$$\mathcal{L}_{Yq} = -G_d^{i,j} (\bar{u}_i, \bar{d}'_i)_L \begin{pmatrix} \phi^+ \\ \phi^0 \end{pmatrix} d_{jR} - G_u^{i,j} (\bar{u}_i, \bar{d}'_i)_L \begin{pmatrix} -\bar{\phi}^0 \\ \phi^- \end{pmatrix} u_{jR} + h.c. \quad (2.52)$$

705 with $i, j = 1, 2, 3$. After SSB and expansion about the ground state, the diagonal form

706 of \mathcal{L}_{Yq} is:

$$\mathcal{L}_{Yq} = -m_d^i \bar{d}_i d_i \left(1 + \frac{H}{v}\right) - m_u^i \bar{u}_i u_i \left(1 + \frac{H}{v}\right) \quad (2.53)$$

707 Fermion masses depend on arbitrary couplings G_l and $G_{u,d}$ and are not predicted
708 by the theory.

709 2.3.5 The Higgs field

710 After the characterization of the fermions and gauge bosons as well as their interac-
711 tions, it is necessary to characterize the Higgs field itself. The Lagrangian \mathcal{L}_S in Eqn.
712 2.37 written in terms of the gauge bosons is given by

$$\mathcal{L}_S = \frac{1}{4} \lambda v^4 + \mathcal{L}_H + \mathcal{L}_{HV} \quad (2.54)$$

713

$$\mathcal{L}_H = \frac{1}{2} \partial_\mu H \partial^\mu H - \frac{1}{2} m_H^2 H^2 - \frac{1}{2v} m_H^2 H^3 - \frac{1}{8v^2} m_H^2 H^4 \quad (2.55)$$

714

$$\mathcal{L}_{HV} = m_H^2 W_\mu^+ W^{\mu-} \left(1 + \frac{2}{v} H + \frac{2}{v^2} H^2\right) + \frac{1}{2} m_Z^2 Z_\mu Z^\mu \left(1 + \frac{2}{v} H + \frac{2}{v^2} H^2\right) \quad (2.56)$$

715 The mass of the Higgs boson is deduced as usual from the mass term in the Lagrangian
716 resulting in:

$$m_H = \sqrt{-2\mu^2} = \sqrt{2\lambda}v \quad (2.57)$$

717 however, it is not predicted by the theory either. The experimental efforts to find the
718 Higgs boson, carried out by the *Compact Muon Solenoid (CMS)* experiment and the *A*
719 *Toroidal LHC Appartus (ATLAS)* experiments at the *Large Hadron Collider (LHC)*,
720 gave great results by July of 2012 when the discovery of a new particle compatible
721 with the Higgs boson predicted by the electroweak theory [36, 37] was announced.
722 Although at the announcement time there were some reservations about calling the
723 new particle the *Higgs boson*, today this name is widely accepted. The Higgs mass

724 measurement, reported by both experiments [38], is in Table 2.8.

Property	Value
Electric charge	0
Color charge	0
Spin	0
Weak isospin	-1/2
Weak hypercharge	1
Parity	1
Mass (GeV/c ²)	125.09±0.21 (stat.)±0.11 (syst.)

Table 2.8: Higgs boson properties. Higgs mass is not predicted by the theory and the value here corresponds to the experimental measurement.

725

726 2.3.6 Production of Higgs bosons at LHC

At the LHC, Higgs bosons are produced as a result of the collision of two counter-rotating protons beams. A detailed description of the LHC machine will be presented in chapter 3.

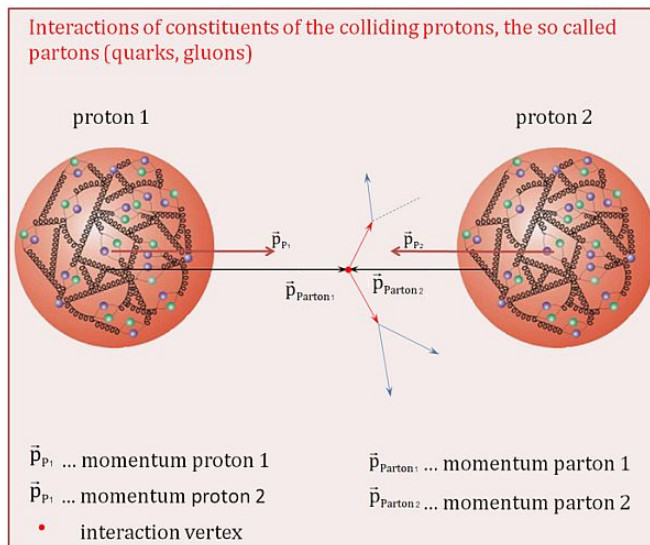


Figure 2.10: Proton-proton collision. Protons are composed of 3 valence quarks, a sea of quarks and gluons; therefore in a proton-proton collision, quarks and gluons are those who collide. [39].

729

730 Protons are composed of quarks and these quarks are bound by gluons; however,
731 what is commonly called the quark content of the proton makes reference to the
732 valence quarks. In fact, a proton is not just a rigid entity with three balls in it all
733 tied up with springs, but the gluons exchanged by the valence quarks tend to split
734 spontaneously into quark-antiquark pairs or more gluons, creating *sea of quarks and*
735 *gluons* as represented in Figure 2.10.

736 In a proton-proton (pp) collision, the proton's constituents, quarks and gluons, are
737 those that collide. The pp cross section depends on the momentum of the colliding
738 particles, reason for which it is needed to know how the momentum is distributed
739 inside the proton. Quarks and gluons are known as partons, hence, the functions that
740 describe how the proton momentum is distributed among partons inside it are called
741 *parton distribution functions (PDFs)*; PDFs are determined from experimental data
742 obtained in experiments where the internal structure of hadrons is tested.

743 In addition, in physics, a common approach to study complex systems consists
744 of starting with a simpler version of them, for which a well known description is
745 available, and adding an additional *perturbation* which represents a small deviation
746 from the known behavior. If the perturbation is small enough, the physical quantities
747 associated with the perturbed system are expressed as a series of corrections to those
748 of the simpler system. The perturbation series corresponds to an expansion in power
749 series of a small parameter, therefore, the more terms are considered in the series (the
750 higher order in the perturbation series), the more precise is the the description of the
751 complex system. If the perturbation does not get progressively smaller, the strategy
752 cannot be applied and new methods have to be employed.

753 High energy systems, like the Higgs production at LHC explored in this thesis,
754 usually can be treated perturbatively with the expansion made in terms of the cou-
755 pling constants. The overview presented here will be oriented specifically to the Higgs

756 boson production mechanisms in pp collisions at LHC.

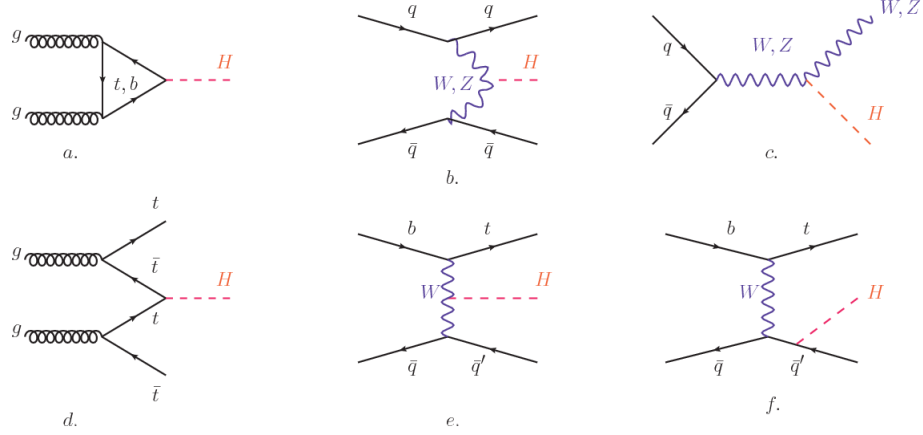


Figure 2.11: Main Higgs boson production mechanism Feynman diagrams. a. gluon-gluon fusion, b. vector boson fusion (VBF), c. Higgs-strahlung, d. Associated production with a top or bottom quark pair, e-f. associated production with a single top quark.

757 Figure 2.11 shows the Feynman diagrams for the leading order (first order) Higgs
 758 production processes at LHC, while the cross section for Higgs production as a func-
 759 tion of the center of mass-energy (\sqrt{s}) for pp collisions is showed in Figure 2.12 left.
 760 The tags NLO (next to leading order), NNLO (next to next to leading order) and
 761 N3LO (next to next to next to leading order) make reference to the order at which
 762 the perturbation series have been considered while the tags QCD and EW correspond
 763 to the strong and electroweak coupling constants respectively.

764 The main production mechanism is the gluon fusion (Figure 2.11a and $pp \rightarrow H$ in
 765 Figure 2.12) given that gluons carry the highest fraction of momentum of the protons
 766 in pp colliders. Since the Higgs boson does not couple to gluons, the mechanism
 767 proceeds through the exchange of a virtual top-quark loop. Note that in this process
 768 the Higgs boson is produced alone, turning out to be problematic for some Higgs
 769 decays, because such absence of anything produced in association with the Higgs
 770 represent a trouble for triggering, however, this mechanism is experimentally clean
 771 when combined with the two-photon or the four-lepton decay channels (see Section

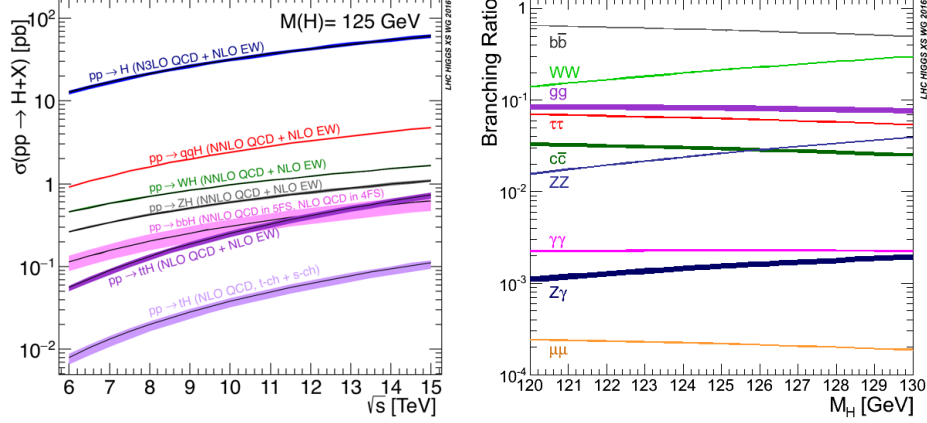


Figure 2.12: Higgs boson production cross sections (left) and decay branching ratios (right) for the main mechanisms. The VBF is indicated as qqH [40].

772 2.3.7).

773 Vector boson fusion (Figure 2.11b and $pp \rightarrow qqH$ in Figure 2.12) has the second
 774 largest production cross section. The scattering of two fermions is mediated by a weak
 775 gauge boson which later emits a Higgs boson. In the final state, the two fermions tend
 776 to be located in the central region of the detector; this kind of features are generally
 777 used as a signature when analyzing the datasets provided by the experiments⁷.

778 The next production mechanism is Higgs-strahlung (Figure 2.11c and $pp \rightarrow WH, pp \rightarrow$
 779 ZH in Figure 2.12) where two fermions annihilate to form a weak gauge boson. If the
 780 initial fermions have enough energy, the emergent boson might emit a Higgs boson.

781 The associated production with a top or bottom quark pair and the associated
 782 production with a single top quark (Figure 2.11d-f and $pp \rightarrow bbH, pp \rightarrow t\bar{t}H, pp \rightarrow tH$
 783 in Figure 2.12) have a smaller cross section than the main three mechanisms above,
 784 but they provide a good opportunity to test the Higgs-top coupling. The analysis
 785 reported in this thesis is developed using these production mechanisms. A detailed
 786 description of the tH mechanism will be given in Section 2.5.

⁷ More details about how to identify events of interest in this analysis will be given in chapter 6.

787 2.3.7 Higgs boson decay channels

788 When a particle can decay through several modes, also known as channels, the prob-
 789 ability of decaying through a given channel is quantified by the *branching ratio (BR)*
 790 of the decay channel; thus, the BR is defined as the ratio of number of decays go-
 791 ing through that given channel to the total number of decays. In regard to the
 792 Higgs boson decay, the BR can be predicted with accuracy once the Higgs mass is
 793 known [41,42]. In Figure 2.12 right, a plot of the BR as a function of the Higgs mass
 794 is presented; the largest predicted BR corresponds to the $b\bar{b}$ pair decay channel (see
 795 Table 2.9) given that it is the heaviest particle pair whose on-shell⁸ production is
 796 kinematically allowed in the decay.

Decay channel	Branching ratio	Rel. uncertainty
$H \rightarrow b\bar{b}$	5.84×10^{-1}	$+3.2\% - 3.3\%$
$H \rightarrow W^+W^-$	2.14×10^{-1}	$+4.3\% - 4.2\%$
$H \rightarrow \tau^+\tau^-$	6.27×10^{-2}	$+5.7\% - 5.7\%$
$H \rightarrow ZZ$	2.62×10^{-2}	$+4.3\% - 4.1\%$
$H \rightarrow \gamma\gamma$	2.27×10^{-3}	$+5.0\% - 4.9\%$
$H \rightarrow Z\gamma$	1.53×10^{-3}	$+9.0\% - 8.9\%$
$H \rightarrow \mu^+\mu^-$	2.18×10^{-4}	$+6.0\% - 5.9\%$

Table 2.9: Predicted branching ratios and the relative uncertainty for some decay channels of a SM Higgs boson with $m_H = 125\text{GeV}/c^2$ [9]; the uncertainties are driven by theoretical uncertainties for the different Higgs boson partial widths and by parametric uncertainties associated to the strong coupling and the masses of the quarks which are the input parameters. Further details on these calculations can be found in Reference [43]

797

798 Decays to other lepton and quark pairs, like electron, strange, up, and down
 799 quark pairs not listed in the table, are also possible but their likelihood is too small

⁸ In general, on-shell or real particles are those which satisfy the energy-momentum relation ($E^2 - |\vec{p}|^2 c^2 = m^2 c^4$); off-shell or virtual particles does not satisfy it which is possible under the uncertainty principle of quantum mechanics. Usually, virtual particles correspond to internal propagators in Feynman diagrams.

800 to measure since they are very lightweight, hence, their interaction with the Higgs
 801 boson is very weak. On other hand, the decay to top quark pairs is heavily suppressed
 802 due to the top quark mass ($\approx 173 \text{ GeV}/c^2$).

803 Decays to gluons proceed indirectly through a virtual top quark loop while the
 804 decays to photons proceed through a virtual W boson loop, therefore, their branching
 805 ratio is smaller compared to direct interaction decays. Same is true for the decay to
 806 a photon and a Z boson.

807 In the case of decays to pairs of W and Z bosons, the decay proceed with one of
 808 the bosons being on-shell and the other being off-shell. The likelihood of the process
 809 diminish depending on how far off-shell are the virtual particles involved, hence, the
 810 branching ratio for W boson pairs is bigger than for Z boson pairs since Z boson mass
 811 is bigger than W boson mass.

812 Note that the decay to a pair of virtual top quarks is possible, but the probability
 813 is way too small.

814 **2.4 Experimental status of the anomalous**

815 **Higgs-fermion coupling**

816 ATLAS and CMS have performed analyses of the anomalous H-f coupling by making
 817 likelihood scans for the two coupling modifiers, κ_t and κ_V , under the assumption
 818 that $\kappa_Z = \kappa_W \equiv \kappa_V$ and $\kappa_t = \kappa_\tau = \kappa_b \equiv \kappa_f$. Figure 2.13 shows the result of the
 819 combination of ATLAS and CMS fits; also the individual decay channels combination
 820 and the global combination results are shown. Note that from this plot there is limited
 821 information on the sign of the coupling since the only information available about the
 822 sign of the coupling comes from decays rather than production.

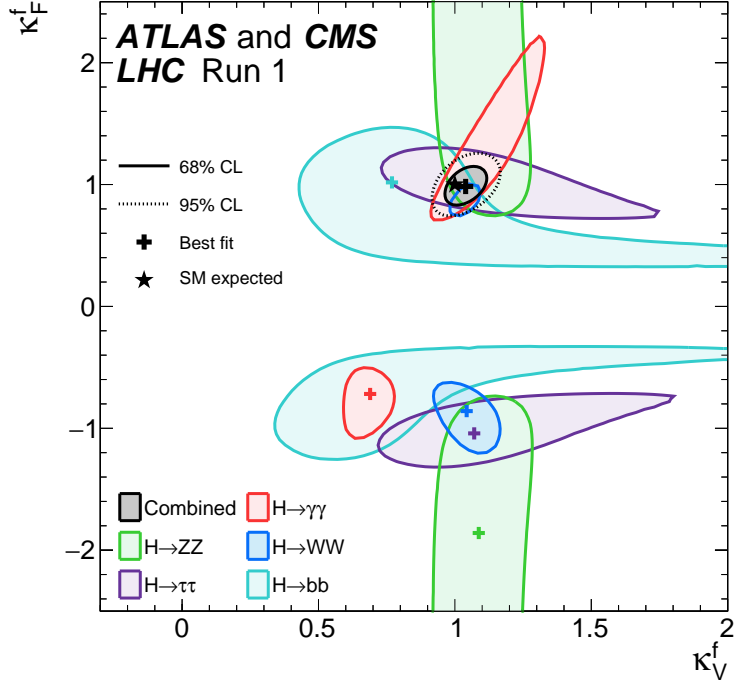


Figure 2.13: Combination of the ATLAS and CMS fits for coupling modifiers $\kappa_t - \kappa_V$; also shown the individual decay channels combination and their global combination. No assumptions have been made on the sign of the coupling modifiers [58].

While all the channels are compatible for positive values of the modifiers, for negative values of κ_t there is no compatibility. The best fit for individual channels is compatible with negative values of κ_t except for the $H \rightarrow bb$ channel. The best fit for the global fit yields $\kappa_t \geq 0$ in contrast to the yields from the individual channels; the reason of this resides in the $H \rightarrow \gamma\gamma$ coupling parameter. $H \rightarrow \gamma\gamma$ decay proceeds through a loop of either top quarks or W bosons, hence, this channel is sensitive to κ_t due to the interference of these two amplitude contributions. Under the assumption that no beyond SM particles take part in the loops, a flipped sign of κ_t will increase the $H \rightarrow \gamma\gamma$ branching fraction by a factor of ~ 2.4 which is not supported by measurements; thus, this large asymmetry between the positive and negative coupling ratios in the $H \rightarrow \gamma\gamma$ channel drives the yield of the global fit. Nevertheless, since the

834 $H \rightarrow bb$ channel is expected to be the most sensitive channel and its best fit value of
 835 κ_t is positive, the global fit is well supported as shown in Reference [58].

836 Although the contributions from all the other decay channels are small compared
 837 to the $H \rightarrow bb$ the anomalous H-t coupling cannot be excluded completely, thus, that
 838 motivates to look at tH processes, which can help with both, the limited information
 839 on the sign of the H-t coupling and the access to information from the Higgs boson
 840 production rather than from its decays.

841 **2.5 Associated production of a Higgs boson and a 842 single top quark**

843 The production of Higgs boson in association with a top quark has been extensively
 844 studied [44–48]. While measurements of the main Higgs production mechanisms rates
 845 are sensitive to the strength of the Higgs coupling to W boson or top quark, they are
 846 not sensitive to the relative sign between the two couplings. In this thesis, the Higgs
 847 boson production mechanism explored is the associated production with a single top
 848 quark (tH) which offers sensitivity to the relative sign of the Higgs couplings to W
 849 boson and to top quark. The description given here is based on Reference [46]

A process where two incoming particles interact and produce a final state with two particles can proceed in three called channels (see, for instance, Figure 2.14 omitting the red line). The t-channel represents processes where an intermediate particle is emitted by one of the incoming particles and absorbed by the other. The s-channel represents processes where the two incoming particles merge into an intermediate particle which eventually will split into the particles in the final state. The third channel, u-channel, is similar to the t-channel but the two outgoing particles interchange their

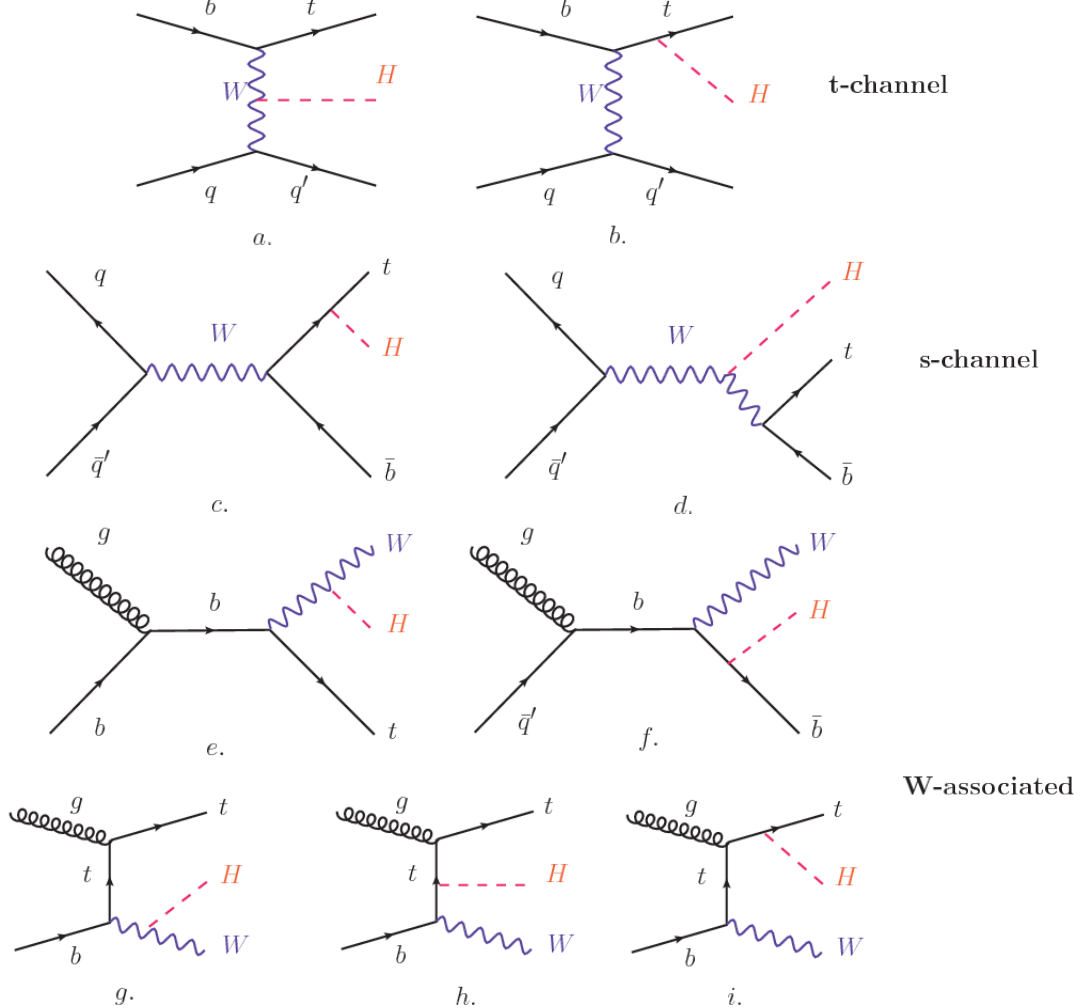


Figure 2.14: Associated Higgs boson production with a top quark mechanism Feynman diagrams. a.,b. t-channel (tHq), c.,d. s-channel (tHb), e-i. W-associated.

roles. These three channels are connected to the so-called Mandelstam variables

$$s = (p_1 + p_2)^2 = (p'_1 + p'_2)^2 \rightarrow \text{square of the center mass-energy.} \quad (2.58)$$

$$t = (p_1 - p'_1)^2 = (p'_2 - p_2)^2 \rightarrow \text{square of the four-momentum transfer.} \quad (2.59)$$

$$u = (p_1 - p'_2)^2 = (p'_1 - p_2)^2 \rightarrow \text{square of the crossed four-momentum transfer.} \quad (2.60)$$

$$s + t + u = m_1^2 + m_2^2 + m'_1^2 + m'_2^2 \quad (2.61)$$

which relate the momentum, energy and the angles of the incoming and outgoing particles in an scattering process of two particles to two particles. The importance of the Mandelstam variables reside in that they form a minimum set of variables needed to describe the kinematics of this scattering process; they are Lorentz invariant which makes them very useful when doing calculations.

The tH production, where Higgs boson can be radiated either from the top quark or from the W boson, is represented by the leading order Feynman diagrams in Figure 2.14. The cross section for the tH process is calculated, as usual, summing over the contributions from the different Feynman diagrams; therefore it depends on the interference between the contributions. In the SM, the interference for t-channel (tHq process) and W-associated (tHW process) production is destructive [44] resulting in the small cross sections presented in Table 2.10.

tH production channel	Cross section (fb)
t-channel ($pp \rightarrow tHq$)	$70.79^{+2.99}_{-4.80}$
W-associated ($pp \rightarrow tHW$)	$15.61^{+0.83}_{-1.04}$
s-channel($pp \rightarrow tHb$)	$2.87^{+0.09}_{-0.08}$

Table 2.10: Predicted SM cross sections for tH production at $\sqrt{s} = 13$ TeV [49, 50].

The s-channel contribution can be neglected. It will be shown that a deviation from the SM destructive interference would result in an enhancement of the tH cross section compared to that in SM, which could be used to get information about the sign of the Higgs-top coupling [46, 47]. In order to describe tH production processes, Feynman diagram 2.14b will be considered; there, the W boson is radiated by a quark in the proton and eventually it will interact with the b quark. In the high energy regime, the effective W approximation [51] is used to describe the process as the

870 emission of an approximately on-shell W and its hard scattering with the b quark;
 871 i.e. $Wb \rightarrow th$. The scattering amplitude for the process is given by

$$\mathcal{A} = \frac{g}{\sqrt{2}} \left[(\kappa_t - \kappa_V) \frac{m_t \sqrt{s}}{m_W v} A \left(\frac{t}{s}, \varphi; \xi_t, \xi_b \right) + \left(\kappa_V \frac{2m_W s}{v t} + (2\kappa_t - \kappa_V) \frac{m_t^2}{m_W v} \right) B \left(\frac{t}{s}, \varphi; \xi_t, \xi_b \right) \right], \quad (2.62)$$

872 where $\kappa_V \equiv g_{HVV}/g_{HVV}^{SM}$ and $\kappa_t \equiv g_{Ht}/g_{Ht}^{SM} = y_t/y_t^{SM}$ are scaling factors that quantify
 873 possible deviations of the couplings from the SM values, Higgs-Vector boson (H-
 874 W) and Higgs-top (H-t) respectively, from the SM couplings; $s = (p_W + p_b)^2$, $t =$
 875 $(p_W - p_H)^2$, φ is the Higgs azimuthal angle around the z axis taken parallel to the
 876 direction of motion of the incoming W; A and B are functions describing the weak
 877 interaction in terms of the chiral states (ξ_t, ξ_b) of the quarks b and t . Terms that
 878 vanish in the high energy limit have been neglected as well as the Higgs and b quark
 879 masses⁹.

880 The scattering amplitude grows with energy like \sqrt{s} for $\kappa_V \neq \kappa_t$, in contrast to
 881 the SM ($\kappa_t = \kappa_V = 1$), where the first term in 2.62 cancels out and the amplitude
 882 is constant for large s ; therefore, a deviation from the SM predictions represents an
 883 enhancement in the tHq cross section. In particular, for a SM H-W coupling and a
 884 H-t coupling of inverted sign with respect to the SM ($\kappa_V = -\kappa_t = 1$) the tHq cross
 885 section is enhanced by a factor greater 10 as seen in the Figure 2.15 taken from
 886 Reference [46]; Reference [52] has reported similar enhancement results.

887 A similar analysis is valid for the W-associated channel but, in that case, the in-
 888 terference is more complicated since there are more than two contributions and an ad-
 889 ditional interference with the production of Higgs boson and a top pair process($t\bar{t}H$).
 890 The calculations are made using the so-called Diagram Removal (DR) technique where

⁹ A detailed explanation of the structure and approximations used to derive \mathcal{A} can be found in Reference [46]

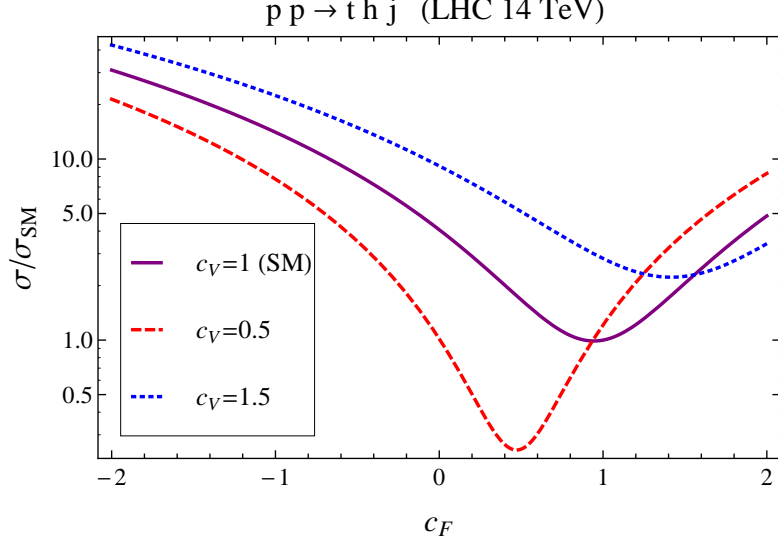


Figure 2.15: Cross section for tHq process as a function of κ_t , normalized to the SM, for three values of κ_V . In the plot c_f refers to the Higgs-fermion coupling which is dominated by the H-t coupling and represented here by κ_t . Solid, dashed and dotted lines correspond to $c_V \rightarrow \kappa_V = 1, 0.5, 1.5$ respectively. Note that for the SM ($\kappa_V = \kappa_t = 1$), the destructive effect of the interference is maximal.

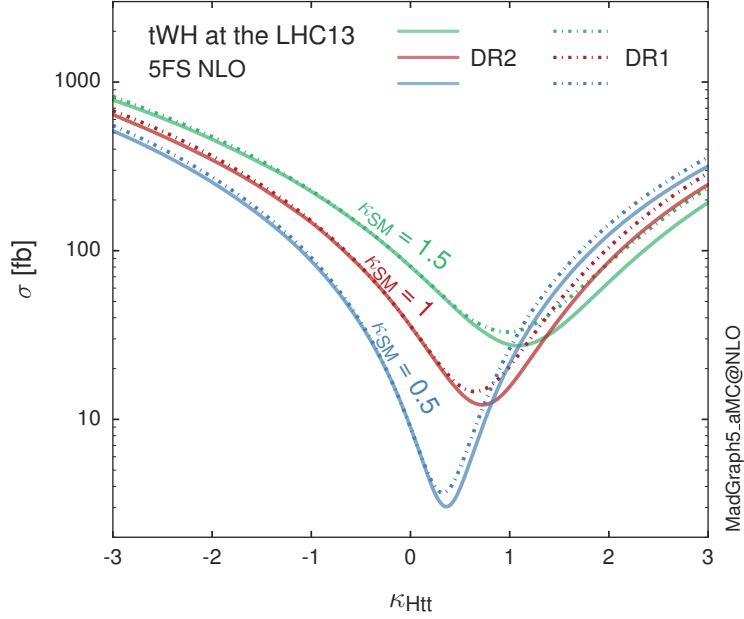


Figure 2.16: Cross section for tHW process as a function of κ_{Htt} , for three values of κ_{SM} at $\sqrt{s} = 13$ TeV. $\kappa_{Htt}^2 = \sigma_{Htt}/\sigma_{Htt}^{SM}$ is a simple re-scaling of the SM Higgs interactions.

interfering diagrams are removed (or added) from the calculations in order to evaluate the impact of the removed contributions. DR1 was defined to neglect $t\bar{t}H$ interference while DR2 was defined to take $t\bar{t}H$ interference into account [53]. As shown in Figure 2.16, the tHW cross section is enhanced from about 15 fb (SM: $\kappa_{Htt} = 1$) to about 150 fb ($\kappa_{Htt} = -1$). Differences between curves for DR1 and DR2 help to gauge the impact of the interference with $t\bar{t}H$. Results of the calculations of the tHq and tHW cross sections at $\sqrt{s} = 13$ TeV can be found in Reference [54] and a summary of the results is presented in Table 2.11.

	\sqrt{s} TeV	$\kappa_t = 1$	$\kappa_t = -1$
$\sigma^{LO}(tHq)(fb)$ [46]	8	≈ 17.4	≈ 252.7
	14	≈ 80.4	≈ 1042
$\sigma^{NLO}(tHq)(fb)$ [46]	8	$18.28^{+0.42}_{-0.38}$	$233.8^{+4.6}_{-0.0}$
	14	$88.2^{+1.7}_{-0.0}$	$982.8^{+28}_{-0.0}$
$\sigma^{LO}(tHq)(fb)$ [52]	14	≈ 71.8	≈ 893
$\sigma^{LO}(tHW)(fb)$ [52]	14	≈ 16.0	≈ 139
$\sigma^{NLO}(tHq)(fb)$ [54]	8	$18.69^{+8.62\%}_{-17.13\%}$	-
	13	$74.25^{+7.48\%}_{-15.35\%}$	$848^{+7.37\%}_{-13.70\%}$
	14	$90.10^{+7.34\%}_{-15.13\%}$	$1011^{+7.24\%}_{-13.39\%}$
$\sigma^{LO}(tHW)(fb)$ [53]	13	$15.77^{+15.91\%}_{-15.76\%}$	-
$\sigma^{NLO}DR1(tHW)(fb)$ [53]	13	$21.72^{+6.52\%}_{-5.24\%}$	≈ 150
$\sigma^{NLO}DR2(tHW)(fb)$ [53]	13	$16.28^{+7.34\%}_{-15.13\%}$	≈ 150

Table 2.11: Predicted enhancement of the tHq and tHW cross sections at LHC for $\kappa_V = 1$ and $\kappa_t = \pm 1$ at LO and NLO; the cross section enhancement of more than a factor of 10 is due to the flipping in the sign of the H-t coupling with respect to the SM one.

899

900 2.6 CP-mixing in tH processes

901 In addition to the sensitivity to sign of the H-t coupling, the tHq and tHW processes
 902 have been proposed as a tool to investigate the possibility of a H-t coupling that does

903 not conserve CP [48, 53, 55].

904 In this thesis, the sensitivity of tH processes to CP-mixing is also studied on the
 905 basis of References [48, 53] using the effective field theory framework where a generic
 906 particle (X_0) of spin-0 and a general CP violating interaction with the top quark
 907 (Htt coupling), can couple to scalar and pseudo-scalar fermionic densities. The H-W
 908 interaction is assumed to be SM-like. The Lagrangian modeling the H-t interaction
 909 is given by

$$\mathcal{L}_0^t = -\bar{\psi}_t (c_\alpha \kappa_{Htt} g_{Htt} + i s_\alpha \kappa_{Att} g_{Att} \gamma_5) \psi_t X_0, \quad (2.63)$$

910 where α is the CP-mixing phase, $c_\alpha \equiv \cos \alpha$ and $s_\alpha \equiv \sin \alpha$, κ_{Htt} and κ_{Att} are real
 911 dimensionless re-scaling parameters¹⁰ used to parametrize the magnitude of the CP-
 912 violating and CP-conserving parts of the amplitude. The model defines $g_{Htt} =$
 913 $g_{Att} = m_t/v = y_t/\sqrt{2}$ with $v \sim 246$ GeV the Higgs vacuum expectation value. In
 914 this parametrization, three special cases can be recovered

915 • CP-even coupling $\rightarrow \alpha = 0^\circ$

916 • CP-odd coupling $\rightarrow \alpha = 90^\circ$

917 • SM coupling $\rightarrow \alpha = 0^\circ$ and $\kappa_{Htt} = 1$

918 The loop induced X_0 coupling to gluons can also be described in terms of the
 919 parametrization above, according to

$$\mathcal{L}_0^g = -\frac{1}{4} \left(c_\alpha \kappa_{Hgg} g_{Hgg} G_{\mu\nu}^a G^{a,\mu\nu} + s_\alpha \kappa_{Agg} g_{Agg} G_{\mu\nu}^a \tilde{G}^{a,\mu\nu} \right) X_0. \quad (2.64)$$

920 where $g_{Hgg} = -\alpha_s/3\pi v$ and $g_{Agg} = \alpha_s/2\pi v$ and $G_{\mu\nu}$ is the gluon field strength tensors.

921 Under the assumption that the top quark dominates the gluon-fusion process at LHC

¹⁰ analog to κ_t and κ_V

energies, $\kappa_{Hgg} \rightarrow \kappa_{Htt}$ and $\kappa_{Agg} \rightarrow \kappa_{Att}$, so that the ratio between the gluon-gluon fusion cross section for X_0 and for the SM Higgs prediction can be written as

$$\frac{\sigma_{NLO}^{gg \rightarrow X_0}}{\sigma_{NLO,SM}^{gg \rightarrow H}} = c_\alpha^2 \kappa_{Htt}^2 + s_\alpha^2 \left(\kappa_{Att} \frac{g_{Agg}}{g_{Hgg}} \right)^2. \quad (2.65)$$

If the re-scaling parameters are set to

$$\kappa_{Htt} = 1, \quad \kappa_{Att} = \left| \frac{g_{Hgg}}{g_{Agg}} \right| = \frac{2}{3}. \quad (2.66)$$

the gluon-fusion SM cross section is reproduced for every value of the CP-mixing angle α ; therefore, by imposing that condition to the Lagrangian density 2.63, the CP-mixing angle is not constrained by current data. Figure 2.17 shows the NLO cross sections for t-channel tX_0 (blue) and $t\bar{t}X_0$ (red) associated production processes as a function of the CP-mixing angle α . X_0 is a generic spin-0 particle with top quark CP-violating coupling. Re-scaling factors κ_{Htt} and κ_{Att} have been set to reproduce the SM gluon-fusion cross sections.

It is interesting to notice that the tX_0 cross section is enhanced, by a factor of about 10, when a continuous rotation in the scalar-pseudoscalar plane is applied; this enhancement is similar to the enhancement produced when the H-t coupling is flipped in sign with respect to the SM ($y_t = -y_{t,SM}$ in the plot), as showed in Section 2.5. In contrast, the degeneracy in the $t\bar{t}X_0$ cross section is still present given that it depends quadratically on the H-t coupling, but more interesting is to notice that $t\bar{t}X_0$ cross section is exceeded by tX_0 cross section after $\alpha \sim 60^\circ$.

A similar parametrization can be used to investigate the tHW process sensitivity to CP-violating H-t coupling. As said in 2.5, the interference in the W-associated channel is more complicated because there are more than two contributions and also there is interference with the $t\bar{t}H$ production process.

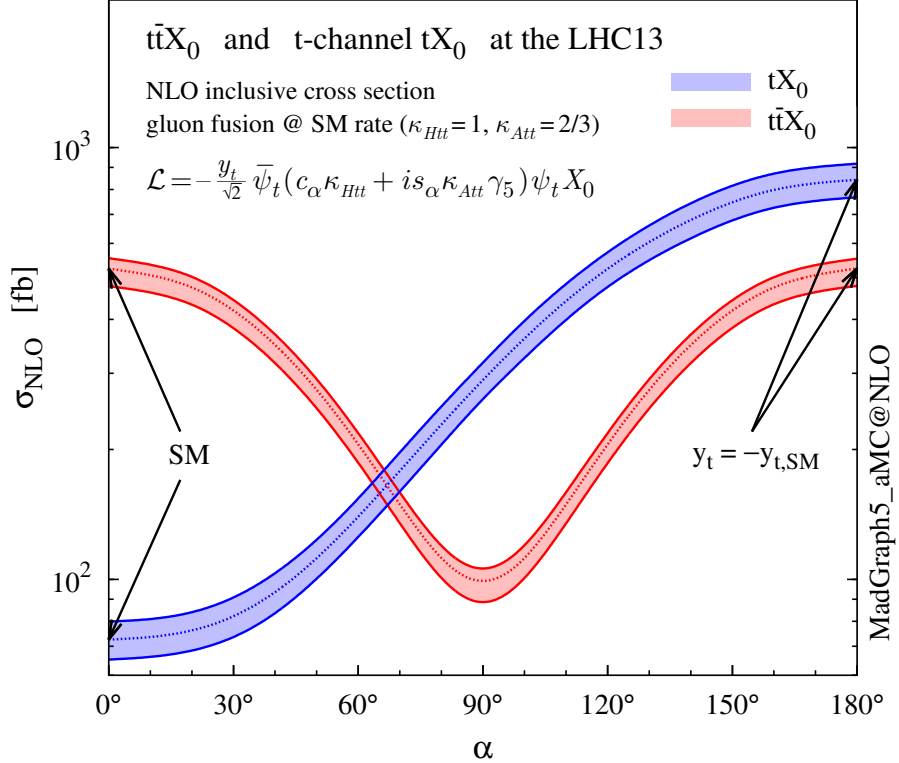


Figure 2.17: NLO cross sections for t-channel tX_0 (blue) and $t\bar{t}X_0$ (red) associated production processes as a function of the CP-mixing angle α . X_0 is a generic spin-0 particle with top quark CP-violating coupling [48].

943 Figure 2.18 shows the NLO cross sections for t-channel tX_0 (blue), $t\bar{t}X_0$ (red)
 944 associated production and for the combined $tWX_0+t\bar{t}X_0+interference$ (orange) as
 945 a function of the CP-mixing angle. It is clear that the effect of the interference in the
 946 combined case is the lifting of the degeneracy present in the $t\bar{t}X_0$ production. The
 947 constructive interference enhances the cross section from about 500 fb at SM ($\alpha = 0$)
 948 to about 600 fb ($\alpha = 180^\circ \rightarrow y_t = -y_{t,SM}$).

949 An analysis combining tHq and tHW processes will be made in this thesis taking
 950 advantage of the sensitivity improvement.

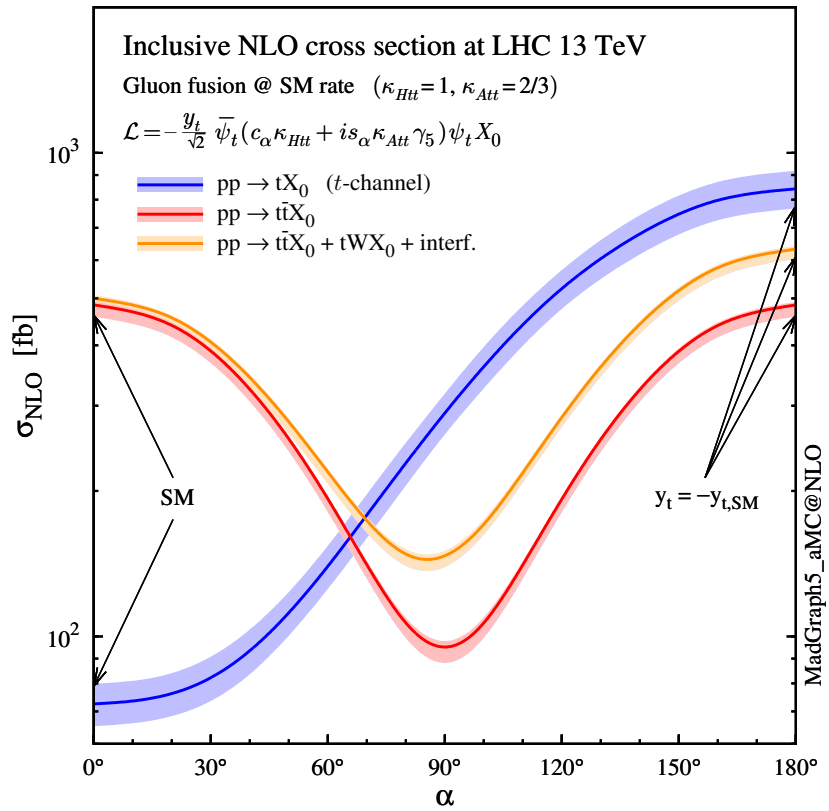


Figure 2.18: NLO cross sections for t-channel tX_0 (blue), $t\bar{t}X_0$ (red) associated production processes and combined $tWX_0 + t\bar{t}X_0$ (including interference) production as a function of the CP-mixing angle α [48].

951 **Chapter 3**

952 **The CMS experiment at the LHC**

953 **3.1 Introduction**

954 Located on the Swiss-French border, the European Council for Nuclear Research
955 (CERN) is the largest scientific organization leading particle physics research. About
956 13000 people in a broad range of roles including users, students, scientists, engineers,
957 among others, contribute to the data taking and analysis, with the goal of unveiling
958 the secrets of nature and revealing the fundamental structure of the universe. CERN
959 is also the home of the Large Hadron Collider (LHC), the largest particle accelerator
960 around the world, where protons (or heavy ions) traveling close to the speed of light,
961 are made to collide. These collisions open a window to investigate how particles (and
962 their constituents if they are composite) interact with each other, providing clues
963 about the laws of nature. This chapter presents an overview of the LHC structure
964 and operation. A detailed description of the CMS detector is offered, given that the
965 data used in this thesis have been taken with this detector.

966 3.2 The LHC

967 With 27 km of circumference, the LHC is currently the most powerful circular accelerator
 968 in the world. It is installed in the same tunnel where the Large Electron-Positron
 969 (LEP) collider was located, taking advantage of the existing infrastructure. The LHC
 970 is part of the CERN's accelerator complex composed of several successive accelerat-
 971 ing stages before the particles are injected into the LHC ring where they reach their
 972 maximum energy (see Figure 3.1).

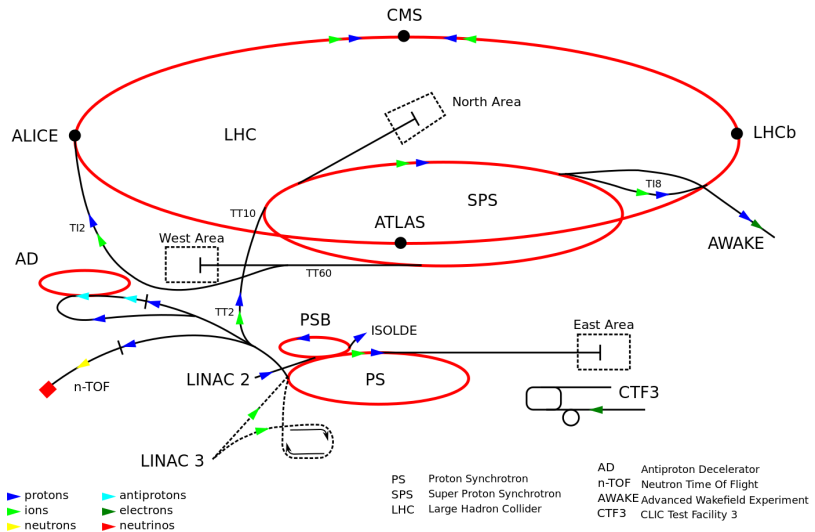


Figure 3.1: CERN accelerator complex. Blue arrows show the path followed by protons along the acceleration process [59].

973 The LHC runs in three collision modes depending on the particles being acceler-
 974 ated

- 975 • Proton-Proton collisions (pp) for multiple physics experiments.
- 976 • Lead-Lead collisions ($Pb-Pb$) for heavy ion experiments.
- 977 • Proton-Lead collisions ($p-Pb$) for quark-gluon plasma experiments.

978 In this thesis only pp collisions will be considered.

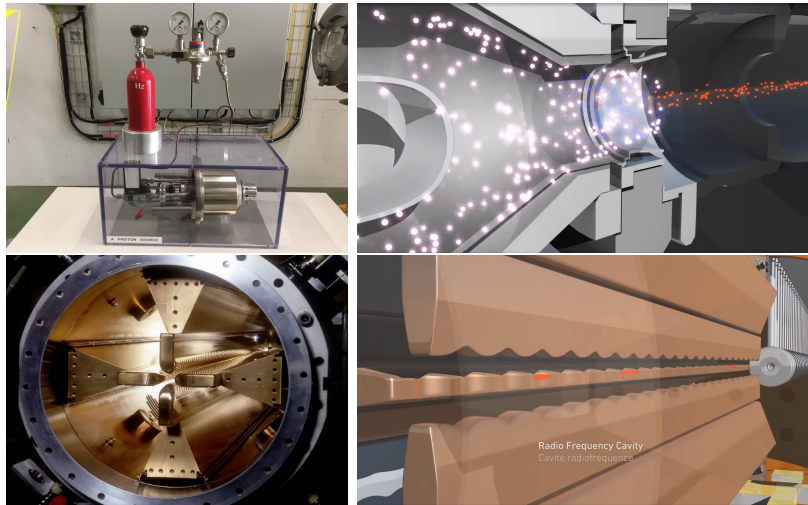


Figure 3.2: LHC protons source and the first acceleration stage. Top: the bottle contains hydrogen gas which is injected into the metal cylinder (white dots) to be broken down into electrons (blue dots) and protons (red dots); Bottom: the obtained protons are directed towards the radio frequency quadrupole which perform the first acceleration, focus the beam and create the bunches of protons. Left images are real pictures while right images are drawings [63, 64].

979 Collection of protons starts with hydrogen atoms taken from a bottle, containing
 980 hydrogen gas, and injecting them in a metal cylinder; hydrogen atoms are broken
 981 down into electrons and protons by an intense electric field (see Figure 3.2 top).
 982 The resulting protons leave the metal cylinder towards a radio frequency quadrupole
 983 (RFQ) that focus the beam, accelerates the protons and creates the packets of protons
 984 called bunches. In the RFQ, an electric field is generated by a RF wave at a frequency
 985 that matches the resonance frequency of the cavity where the electrodes are contained.
 986 The beam of protons traveling on the RFQ axis experiences an alternating electric
 987 field gradient that generates the focusing forces.

988 In order to accelerate the protons, a longitudinal time-varying electric field com-
 989 ponent is added to the system; it is done by giving the electrodes a sine-like profile as
 990 shown in Figure 3.2 bottom. By matching the speed and phase of the protons with
 991 the longitudinal electric field the bunching is performed; protons synchronized with

992 the RFQ (synchronous protons) do not feel an accelerating force, but those protons in
 993 the beam that have more (or less) energy than the synchronous proton (asynchronous
 994 protons) will feel a decelerating (accelerating) force; therefore, asynchronous protons
 995 will oscillate around the synchronous ones forming bunches of protons [61]. From the
 996 RFQ protons emerge with energy 750 keV in bunches of about 1.15×10^{11} protons [62].

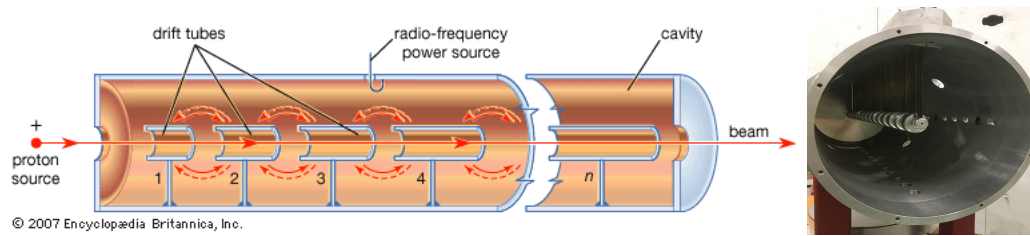


Figure 3.3: Left: drawing of the LINAC2 accelerating system at CERN. Electric fields generated by radio frequency (RF) create acceleration and deceleration zones inside the cavity; deceleration zones are blocked by drift tubes where quadrupole magnets focus the proton beam. Right: picture of a real RF cavity [65].

997 Proton bunches coming from the RFQ go to the linear accelerator 2 (LINAC2)
 998 where they are accelerated to reach 50 MeV energy. In the LINAC2 stage, acceleration
 999 is performed using electric fields generated by radio frequency which create zones
 1000 of acceleration and deceleration as shown in Figure 3.3. In the deceleration zones,
 1001 the electric field is blocked using drift tubes where protons are free to drift while
 1002 quadrupole magnets focus the beam.

1003 The beam coming from LINAC2 is injected into the proton synchrotron booster
 1004 (PSB) to reach 1.4 GeV in energy. The next acceleration is provided at the proton
 1005 synchrotron (PS) up to 26 GeV, followed by the injection into the super proton
 1006 synchrotron (SPS) where protons are accelerated to 450 GeV. Finally, protons are
 1007 injected into the LHC where they are accelerated to the target energy of 6.5 TeV.

1008 PSB, PS, SPS and LHC accelerate protons using the same RF acceleration tech-
 1009 nique described before.

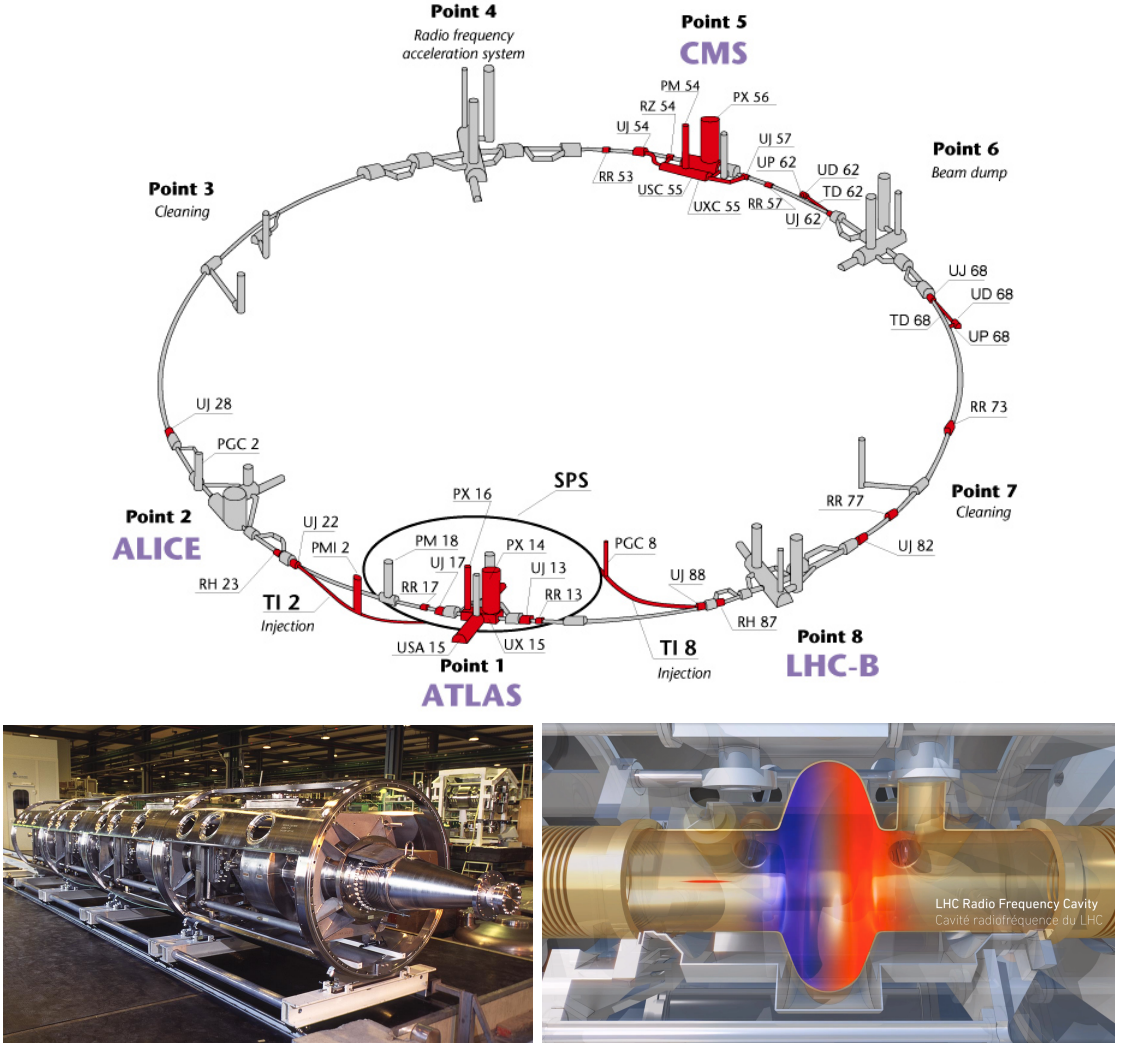


Figure 3.4: Top: LHC layout. The red zones indicate the infrastructure additions to the LEP installations, built to accommodate the ATLAS and CMS experiments which exceed the size of the former experiments located there [60]. Bottom: LHC RF cavities. A module (left picture) accommodates 4 cavities, each like the one in the right drawing, that accelerate protons and preserve the bunch structure of the beam. The color gradient pattern represents the strength of the electric field inside the cavity; red zone corresponds to the maximum of the oscillation electric field while the blue zone corresponds to the minimum. [64, 66]

1010 The LHC has a system of 16 RF cavities located in the so-called point 4, as
 1011 shown in Figure 3.4 top, tuned at a frequency of 400 MHz. The bottom side of
 1012 Figure 3.4 shows a picture of a RF module composed of 4 RF cavities working in a
 1013 superconducting state at 4.5 K; also, a representation of the accelerating electric field

1014 that accelerates the protons in the bunch is shown. The maximum of the oscillating
 1015 electric field (red region) picks the proton bunches at the entrance of the cavity
 1016 and keeps accelerating them through the whole cavity. The protons are carefully
 1017 timed so that in addition to the acceleration effect the bunch structure of the beam
 1018 is preserved.

1019 While protons are accelerated in one section of the LHC ring, where the RF cavities
 1020 are located, in the rest of their path they have to be kept in the curved trajectory
 1021 defined by the LHC ring. Technically, LHC is not a perfect circle; RF, injection, beam
 1022 dumping, beam cleaning and sections before and after the experimental points where
 1023 protons collide are all straight sections. In total, there are 8 arcs 2.45 km long each
 1024 and 8 straight sections 545 m long each. In order to curve the proton's trajectory in
 1025 the arc sections, superconducting dipole magnets are used.

1026 Inside the LHC ring, there are two proton beams traveling in opposite directions
 1027 in two separated beam pipes; the beam pipes are kept at ultra-high vacuum ($\sim 10^{-9}$
 1028 Pa) to ensure that there are no particles that interact with the proton beams. The
 1029 superconducting dipole magnets used in LHC are made of a NbTi alloy, capable of
 1030 transporting currents of about 12000 A when cooled at a temperature below 2K using
 1031 liquid helium (see Figure 3.5).

1032 Protons in the arc sections of LHC feel a centripetal force exerted by the dipole
 1033 magnets; the magnitude of magnetic field needed to keep the protons in the LHC
 1034 curved trayectomy can be found assuming that protons travel at $v \approx c$, using the
 1035 standard values for proton mass and charge and the LHC radius, as

$$F_m = \frac{mv^2}{r} = qBv \rightarrow B = 8.33T \quad (3.1)$$

1036 which is about 100000 times the Earth's magnetic field. A representation of the

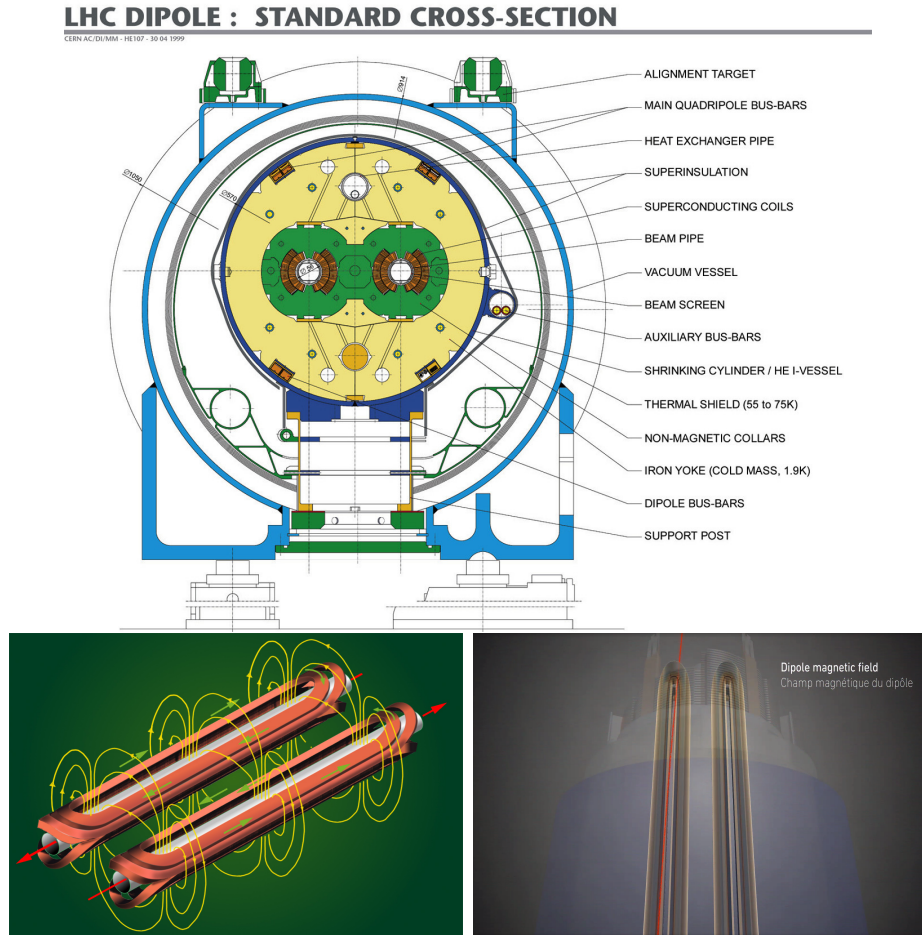


Figure 3.5: Top: LHC dipole magnet transverse view; cooling, shielding and mechanical support are indicated. Bottom left: Magnetic field generated by the dipole magnets; note that the direction of the field inside one beam pipe is opposite with respect to the other beam pipe which guarantee that both proton beams are curved in the same direction towards the center of the ring. The effect of the dipole magnetic field on the proton beam is represented on the bottom right side [64, 67, 68].

1037 magnetic field generated by the dipole magnets is shown on the bottom left side of
 1038 Figure 3.5. The bending effect of the magnetic field on the proton beam is shown on
 1039 the bottom right side of Figure 3.5. Note that the dipole magnets are not curved;
 1040 the arc section of the LHC ring is composed of straight dipole magnets of about 15
 1041 m. In total there are 1232 dipole magnets along the LHC ring.
 1042 In addition to the bending of the beam trajectory, the beam has to be focused. The

1043 focusing is performed by quadrupole magnets installed in a different straight section;
 1044 in total 858 quadrupole magnets are installed along the LHC ring. Other effects like
 1045 electromagnetic interaction among bunches, interaction with electron clouds from the
 1046 beam pipe, the gravitational force on the protons, differences in energy among protons
 1047 in the same bunch, among others, are corrected using sextupole and other magnetic
 1048 multipoles.

1049 The two proton beams inside the LHC ring are made of bunches with a cylindrical
 1050 shape of about 7.5 cm long and about 1 mm in diameter; when bunches are close to the
 1051 interaction point (IP), the beam is focused up to a diameter of about 16 μm in order
 1052 to maximize the probability of collisions between protons. The number of collisions
 1053 per second is proportional to the cross section of the bunches with the *luminosity* (L)
 1054 as the proportionality factor, thus, the luminosity can be calculated using

$$L = fn \frac{N_1 N_2}{4\pi\sigma_x\sigma_y} \quad (3.2)$$

1055 where f is the revolution frequency, n is the number of bunches per beam, N_1 and N_2
 1056 are the numbers of protons per bunch, σ_x and σ_y are the gaussian transverse sizes of
 1057 the bunches. With the expected parameters, the LHC expected luminosity is about

$$f = \frac{v}{2\pi r_{LHC}} \approx \frac{3 \times 10^8 \text{ m/s}}{27 \text{ km}} \approx 11.1 \text{ kHz},$$

$$n = 2808$$

$$N_1 = N_2 \sim 1.5 \times 10^{11}$$

$$\sigma_x = \sigma_y = 16 \mu\text{m}$$

1058

$$L = 1.28 \times 10^{34} \text{ cm}^{-2} \text{ s}^{-1} = 1.28 \times 10^{-5} \text{ fb}^{-1} \text{ s}^{-1} \quad (3.3)$$

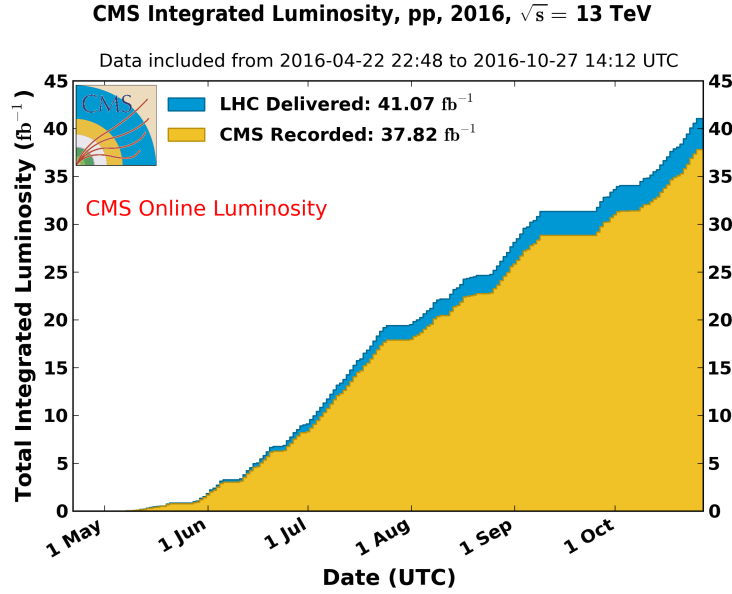


Figure 3.6: Integrated luminosity delivered by LHC and recorded by CMS during 2016. The difference between the delivered and the recorded luminosity is due to fails and issues occurred during the data taking in the CMS experiment [69].

1059 Luminosity is a fundamental aspect of LHC given that the bigger luminosity the
 1060 bigger number of collisions, which means that for processes with a very small cross
 1061 section the number of expected occurrences is increased and so the chances of being
 1062 detected. The integrated luminosity, collected by the CMS experiment during 2016
 1063 is shown in Figure 3.6; the data analyzed in this thesis corresponds to an integrated
 1064 luminosity of 35.9 fb^{-1} at a center of mass-energy $\sqrt{s} = 13 \text{ TeV}$.

1065 One way to increase L is increasing the number of bunches in the beam. Cur-
 1066 rently, the separation between two consecutive bunches in the beam is 7.5 m which
 1067 corresponds to a time separation of 25 ns. In the full LHC ring the allowed number
 1068 of bunches is $n = 27\text{km}/7.5\text{m} = 3600$; however, there are some gaps in the bunch pat-
 1069 tern intended for preparing the dumping and injection of the beam, thus, the proton
 1070 beams are composed of 2808 bunches.

1071 Once the proton beams reach the desired energy, they are brought to cross each

1072 other producing pp collisions. The bunch crossing happens in precise places where
 1073 the four LHC experiments are located, as seen in the top of Figure 3.7. In 2008 pp
 1074 collisions of $\sqrt{s} = 7$ TeV were performed; the energy was increased to 8 TeV in 2012
 1075 and to 13 TeV in 2015.

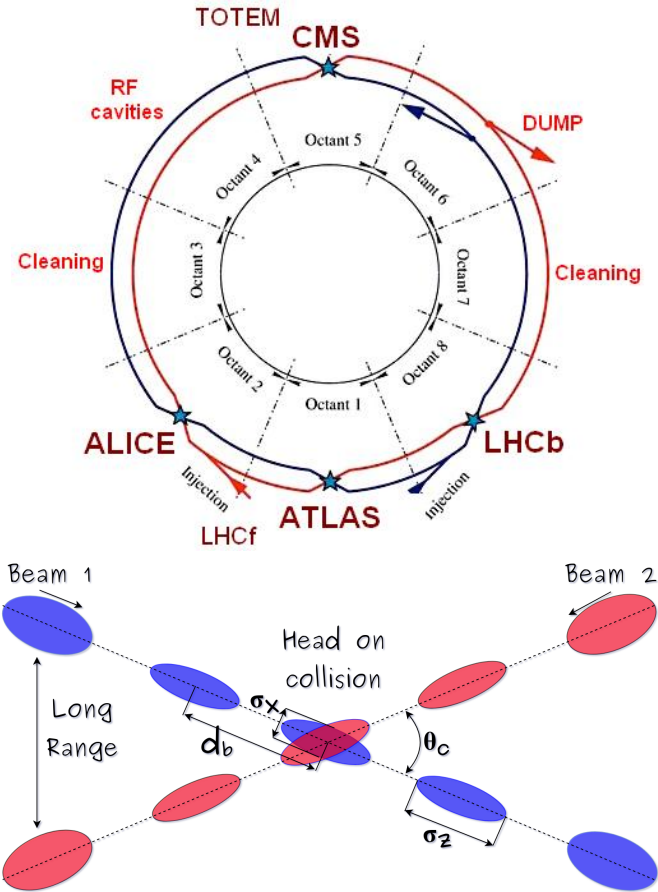


Figure 3.7: Top: LHC interaction points. Bunch crossing occurs where the LHC experiments are located [70]. Sections indicated as cleaning are dedicated to collimate the beam in order to protect the LHC ring from collisions with protons in very spreaded bunches. Bottom: bunch crossing scheme. Since the bunch crossing is not perfectly head-on, the luminosity is reduced in a factor of 17%; adapted from Reference [84].

1076 The CMS and ATLAS experiments are multi-purpose experiments, hence, they
 1077 are enabled to explore physics in any of the LHC collision modes. LHCb experiment
 1078 is optimized to explore bottom quark physics, while ALICE is optimized for heavy

1079 ion collisions searches; TOTEM and LHCf are dedicated to forward physics studies;
 1080 MoEDAL (not indicated in the Figure) is intended for monopole or massive pseudo
 1081 stable particles searches.

1082 At the IP there are two interesting details that need to be addressed. The first
 1083 one is that the bunch crossing does not occur head-on but at a small crossing angle θ_c
 1084 (280 μ rad in CMS and ATLAS) as shown in the bottom side of Figure 3.7, affecting
 1085 the overlapping between bunches; the consequence is a reduction of about 17% in
 1086 the luminosity (represented by a factor not included in eqn. 3.2). The second one
 1087 is the occurrence of multiple pp collisions in the same bunch crossing; this effect is
 1088 called *pileup* (PU). A fairly simple estimation of the PU follows from estimating the
 1089 probability of collision between two protons, one from each of the bunches in the
 1090 course of collision; it depends roughly on the ratio of proton size and the cross section
 1091 of the bunch in the IP, i.e.,

$$P(pp\text{-}collision) \sim \frac{d_{proton}^2}{\sigma_x \sigma_y} = \frac{(1\text{fm})^2}{(16\mu\text{m})^2} \sim 4 \times 10^{-21} \quad (3.4)$$

1092 however, there are $N = 1.15 \times 10^{11}$ protons in a bunch, thus the estimated number of
 1093 collisions in a bunch crossing is

$$PU = N^2 * P(pp\text{-}collision) \sim 50pp \text{ collision per bunch crossing}, \quad (3.5)$$

1094 about 20 of which are inelastic. A multiple pp collision event in a bunch crossing at
 1095 CMS is shown in Figure 3.8.

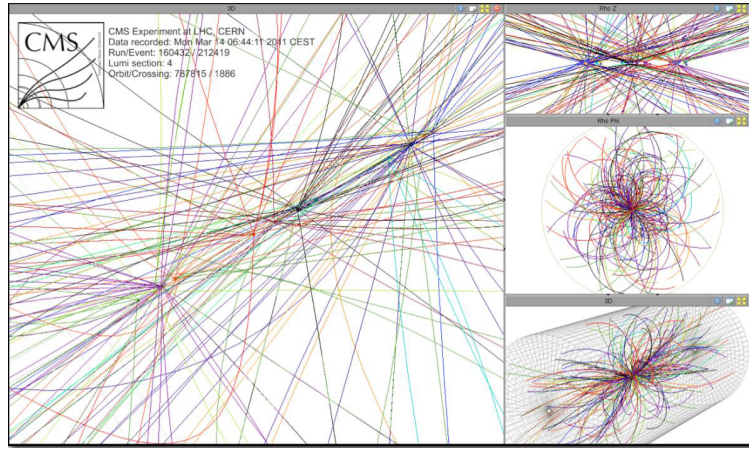


Figure 3.8: Multiple pp collision bunch crossing at CMS. [71].

1096 3.3 The CMS experiment

1097 CMS is a general-purpose detector designed to conduct research in a wide range
 1098 of physics from the standard model to new physics like extra dimensions and dark
 1099 matter. Located at Point 5 in the LHC layout as shown in Figure 3.4, CMS is
 1100 composed of several detection systems distributed in a cylindrical structure; in total,
 1101 CMS weights about 12500 tons in a very compact 21.6 m long and 14.6 m diameter
 1102 cylinder. It was built in 15 separate sections at the ground level and lowered to the
 1103 cavern individually to be assembled. A complete and detailed description of the CMS
 1104 detector and its components is given in Reference [72] on which this section is based.
 1105 Figure 3.9 shows the layout of the CMS detector. The detection system is composed
 1106 of (from the innermost to the outermost)

- 1107 • Pixel detector.
- 1108 • Silicon strip tracker.
- 1109 • Preshower detector.
- 1110 • Electromagnetic calorimeter.

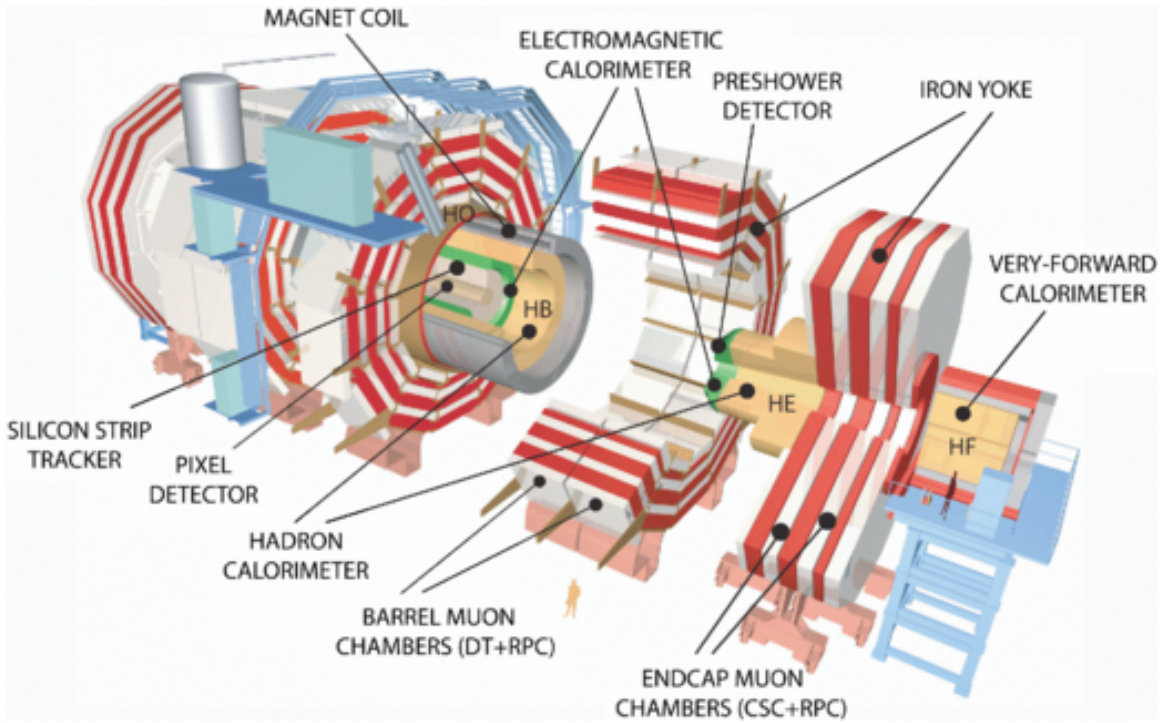


Figure 3.9: Layout of the CMS detector. The several subdetectors are indicated. The central region of the detector is referred as the barrel section while the endcaps are referred as the forward sections. [73].

1111 • Hadronic calorimeter.

1112 • Muon chambers (barrel and endcap)

1113 The central region of the detector is commonly referred as the barrel section while
 1114 the endcaps are referred as the forward sections of the detector; thus, each subdetector
 1115 is composed of a barrel section and a forward section.

1116 When a pp collision happens inside the CMS detector, many different particles are
 1117 produced, but only some of them live long enough to be detected; they are electrons,
 1118 photons, pions, kaons, protons, neutrons and muons; neutrinos are not detected by
 1119 the CMS detector. Thus, the CMS detector was designed to detect those particles and
 1120 measure their properties. Figure 3.10 shows a transverse slice of the CMS detector.
 1121 The silicon tracker (pixel detector + strip tracker) is capable to register the track of

the charged particles traversing it, while calorimeters (electromagnetic and hadronic) measure the energy of the particles that are absorbed by their materials. Considering the detectable particles, mentioned above, emerging from the IP, a basic description of the detection process is as follows.

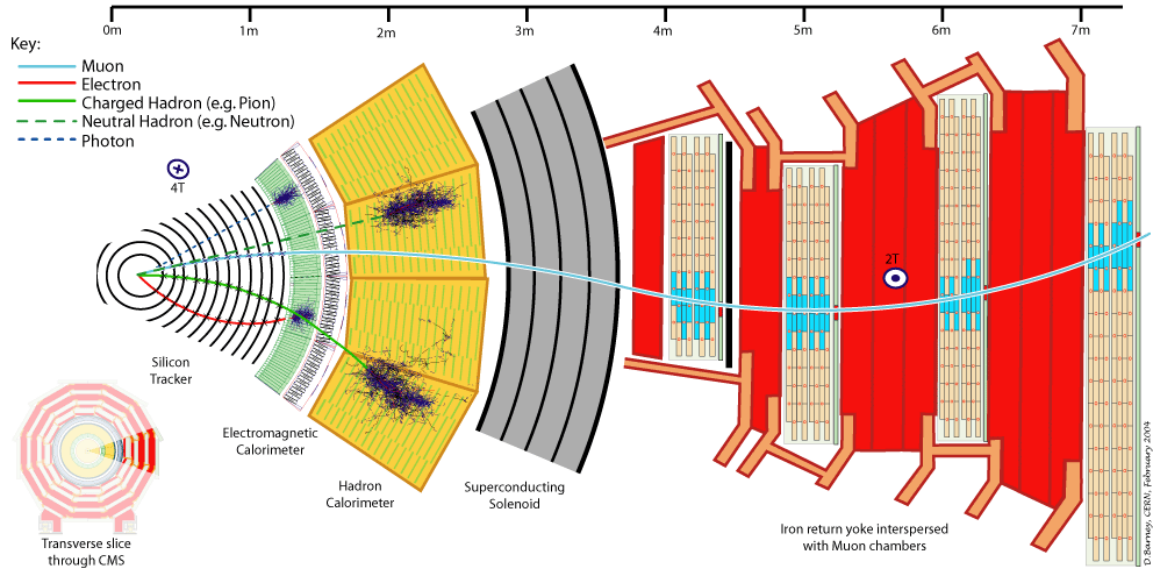


Figure 3.10: CMS detector transverse slice [74].

A muon emerging from the IP, will create a track on the silicon tracker and on the muon chambers. The design of the CMS detector is driven by the requirements on the identification, momentum resolution and unambiguous charge determination of the muons; therefore, a large bending power is provided by the solenoid magnet made of superconducting cable capable of generating a 3.8 T magnetic field. The muon track is bent twice since the magnetic field inside the solenoid is directed along the z -direction but outside its direction is reversed. Muons interact very weakly with the calorimeters, therefore, it is not absorbed but escape away from the detector.

An electron emerging from the IP will create a track along the tracker which will be bent due to the presence of the magnetic field, later, it will be absorbed in the electromagnetic calorimeter where its energy is measured.

1137 A photon will not leave a track because it is neutral, but it will be absorbed in
 1138 the electromagnetic calorimeter.

1139 A neutral hadron, like the neutron, will not leave a track either but it will lose a
 1140 small amount of its energy during its passage through the electromagnetic calorimeter
 1141 and then it will be absorbed in the hadron calorimeter depositing the rest of its energy.

1142 A charged hadron, like the proton or π^\pm , will leave a curved track on the silicon
 1143 tracker, some of its energy in the electromagnetic calorimeter and finally will be
 1144 absorbed in the hadronic calorimeter.

1145 A more detailed description of each detection system will be presented in the
 1146 following sections.

1147 3.3.1 CMS coordinate system

1148 The coordinate system used by CMS is centered on the geometrical center of the
 1149 detector which is the nominal IP as shown in Figure 3.11¹. The z -axis is parallel
 1150 to the beam direction, while the Y -axis pointing vertically upward, and the X -axis
 1151 pointing radially inward toward the center of the LHC.

1152 In addition to the common cartesian and cylindrical coordinate systems, two co-
 1153 ordinates are of particular utility in particle physics: rapidity (y) and pseudorapidity
 1154 (η), defined in connection to the polar angle θ , energy and longitudinal momentum
 1155 component (momentum along the z -axis) according to

$$y = \frac{1}{2} \ln \frac{E + p_z}{E - p_z} \quad \eta = -\ln \left(\tan \frac{\theta}{2} \right) \quad (3.6)$$

1156 Rapidity is related to the angle between the XY -plane and the direction in which
 1157 the products of a collision are emitted; it has the nice property that the difference

¹ Not all the pp interaction occur at the nominal IP because of the bunch lenght, therefore, each pp collision has its own IP location

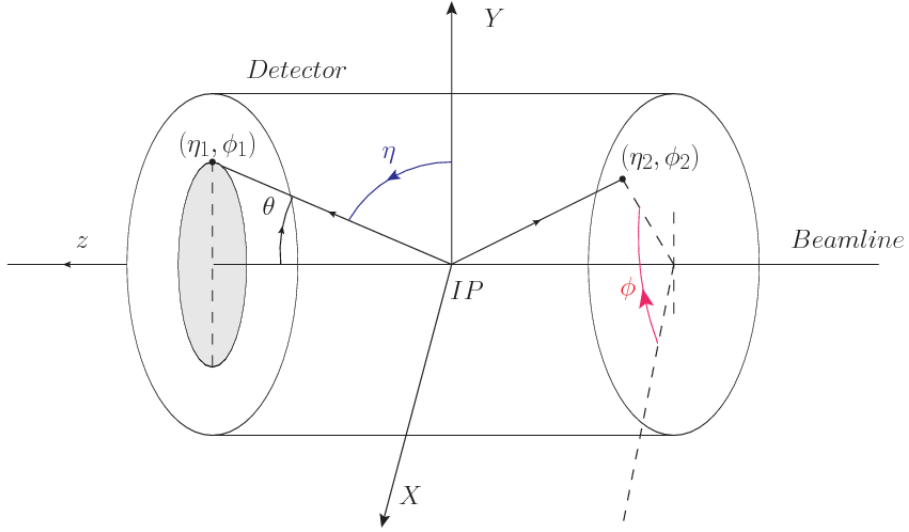


Figure 3.11: CMS detector coordinate system.

1158 between the rapidities of two particles is invariant with respect to Lorentz boosts
 1159 along the z -axis, hence, data analysis becomes more simple when based on rapid-
 1160 ity; however, it is not simple to measure the rapidity of highly relativistic particles,
 1161 as those produced after pp collisions. Under the highly relativistic motion approxi-
 1162 mation, y can be rewritten in terms of the polar angle, concluding that rapidity is
 1163 approximately equal to the pseudorapidity defined above, i.e., $y \approx \eta$. Note that η
 1164 is easier to measure than y given the direct relationship between the former and the
 1165 polar angle.

1166 The angular distance between two objects in the detector (ΔR) is commonly used
 1167 to judge the isolation of those object; it is defined in terms of their coordinates (η_1, ϕ_1) ,
 1168 (η_2, ϕ_2) as

$$\Delta R = \sqrt{(\Delta\eta)^2 - (\Delta\phi)^2} \quad (3.7)$$

1169 3.3.2 Tracking system

1170 The CMS tracking system is designed to provide a precise measurement of the trajectories (*track*) followed by the charged particles created after the pp collisions; also, the
 1171 precise reconstruction of the primary and secondary origins of the tracks (*vertices*) is
 1172 expected in an environment where, each 25 ns, the bunch crossing produces about 20
 1173 inelastic collisions and about 1000 particles.
 1174

1175 Physics requirements guiding the tracking system performance include the precise characterization of events involving gauge bosons, W and Z, and their leptonic
 1176 decays for which an efficient isolated lepton and photon reconstruction is of capital
 1177 importance, given that isolation is required to suppress background events to a level
 1178 that allows observations of interesting processes like Higgs boson decays or beyond
 1179 SM events.

1181 The ability to identify and reconstruct b -jets and B-hadrons within these jets is also
 1182 a fundamental requirement, achieved through the ability to reconstruct accurately
 1183 displaced vertices, given that b -jets are part of the signature of top quark physics, like
 1184 the one treated in this thesis.

1185 An schematic view of the CMS tracking system is shown in Figure 3.12

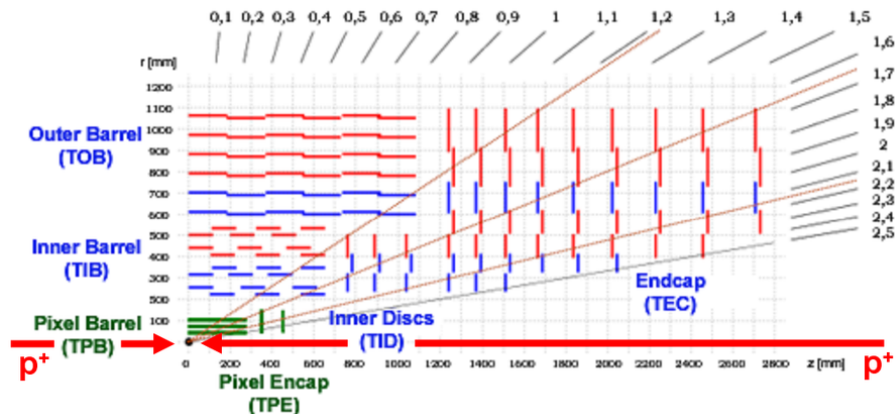


Figure 3.12: CMS tracking system schematic view [76].

1186 In order to satisfy these performance requirements, the tracking system uses two
 1187 different detector subsystems arranged in concentric cylindrical volumes, the pixel
 1188 detector and the silicon strip tracker; the pixel detector is located in the high particle
 1189 density region ($r < 20\text{cm}$) while the silicon strip tracker is located in the medium and
 1190 lower particle density regions $20\text{cm} < r < 116\text{cm}$.

1191 **Pixel detector**

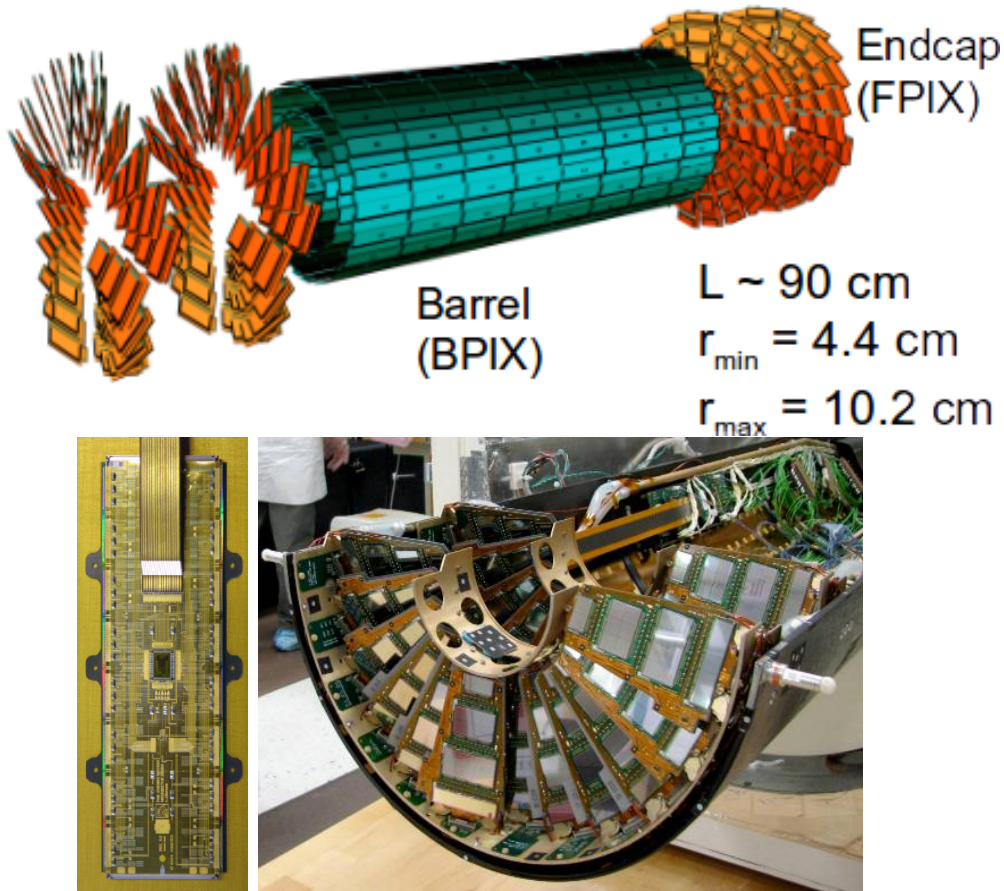


Figure 3.13: CMS pixel detector. Top: schematic view; Bottom: pictures of a barrel(BPIX) module(left) and forward modules(right) [72].

1192 The pixel detector was replaced during the 2016-2017 extended year-end technical
 1193 stop, due to the increasingly challenging operating conditions like the higher particle

flux and more radiation harsh environment, among others. The new one is responding as expected, reinforcing its crucial role in the successful way to fulfill the new LHC physics objectives after the discovery of the Higgs boson. Since the data sets used in this thesis were produced using the previous version of the pixel detector, it will be the subject of the description in this section. The last chapter of this thesis is dedicated to describe my contribution to the *Forward Pixel Phase 1 upgrade*.

The pixel detector was composed of 1440 silicon pixel detector modules organized in three-barrel layers in the central region (BPix) and two disks in the forward region (FPix) as shown in the top side of Figure 3.13; it was designed to record efficiently and with high precision, up to $20\mu\text{m}$ in the XY -plane and $20\mu\text{m}$ in the z -direction, the first three space-points (*hits*) nearest to the IP region in the range $|\eta| \leq 2.5$. The first barrel layer was located at a radius of 44 mm from the beamline, while the third layer was located at a radius of 102 mm, closer to the strip tracker inner barrel layer (see Section 3.3.3) in order to reduce the rate of fake tracks. The high granularity of the detector is represented in its about 66 Mpixels, each of size $100 \times 150\mu\text{m}^2$. The transverse momentum resolution of tracks can be measured with a resolution of 1-2% for muons of $p_T = 100$ GeV.

A charged particle passing through the pixel sensors produce ionization in them, giving energy for electrons to be removed from the silicon atoms, hence, creating electron-hole pairs. The collection of charges in the pixels generates an electrical signal that is read out by an electronic readout chip (ROC); each pixel has its own electronics which amplifies the signal. Combining the signal from the pixels activated by a traversing particle in the several layers of the detector allows one to reconstruct the particle's trajectory in 3D.

Commonly, the charge produced by traversing of a particle is collected by and shared among several pixels; by interpolating between pixels, the spatial resolution

is improved. In the barrel section the charge sharing in the $r\phi$ -plane is due to the Lorentz effect. In the forward pixels the charge sharing is enhanced by arranging the blades in the turbine-like layout as shown in Figure 3.13 bottom left.

3.3.3 Silicon strip tracker

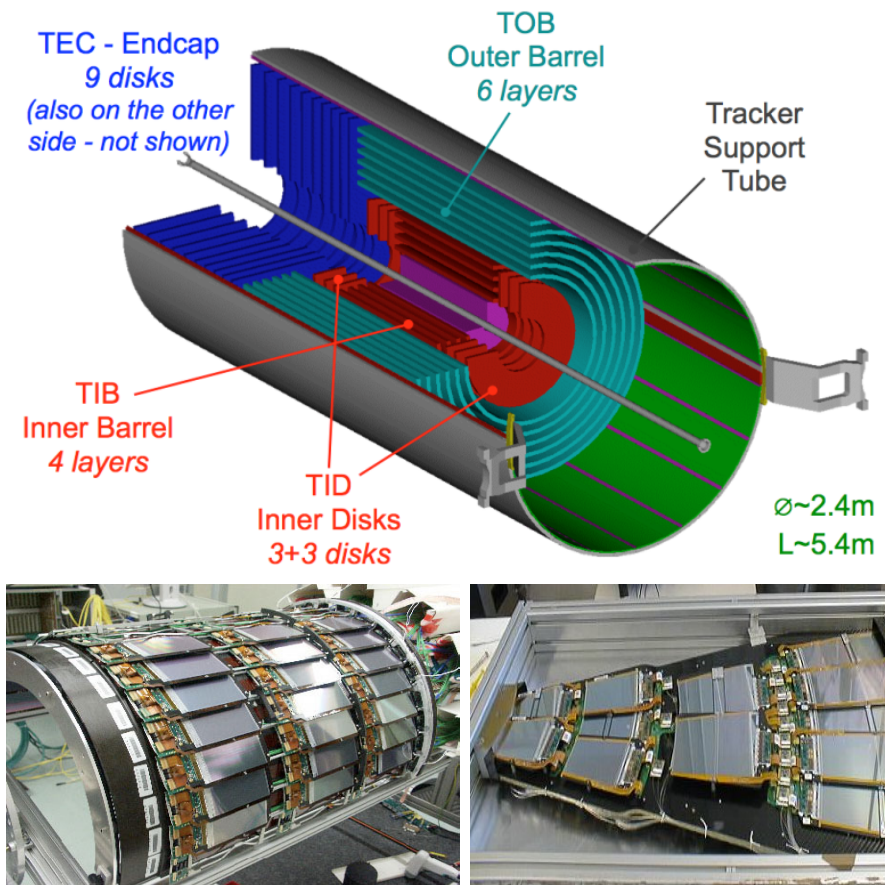


Figure 3.14: Top: CMS Silicon Strip Tracker (SST) schematic view. The SST is composed of the tracker inner barrel (TIB), the tracker inner disks (TID), the tracker outer barrel (TOB) and the tracker endcaps (TEC). Each part is made of silicon strip modules; the modules in blue represent two modules mounted back-to-back and rotated in the plane of the module by a stereo angle of 120 mrad in order to provide a 3-D reconstruction of the hit positions. Bottom: pictures of the TIB (left) and TEC (right) modules [78–80].

The silicon strip tracker (SST) is the second stage in the CMS tracking system. The top side of Figure 3.14 shows a schematic of the SST. The inner tracker region is

1226 composed of the tracker inner barrel (TIB) and the tracker inner disks (TID) covering
 1227 the region $r < 55$ cm and $|z| < 118$ cm. The TIB is composed of 4 layers while the TID
 1228 is composed of 3 disks at each end. The silicon sensors in the inner tracker are 320
 1229 μm thick, providing a resolution of about 13-38 μm in the $r\phi$ position measurement.

1230 The modules indicated in blue in the schematic view of Figure 3.14 are two mod-
 1231 ules mounted back-to-back and rotated in the plane of the module by a *stereo* angle
 1232 of 100 mrad; the hits from these two modules, known as *stereo hits*, are combined to
 1233 provide a measurement of the second coordinate (z in the barrel and r on the disks)
 1234 allowing the reconstruction of hit positions in 3-D.

1235 The outer tracker region is composed of the tracker outer barrel (TOB) and the
 1236 tracker endcaps (TEC). The six layers of the TOB offer coverage in the region $r > 55$
 1237 cm and $|z| < 118$ cm, while the 9 disks of the TEC cover the region $124 < |z| < 282$
 1238 cm. The resolution offered by the outer tracker is about 13-38 μm in the $r\phi$ position
 1239 measurement. The inner four TEC disks use silicon sensors 320 μm thick; those in
 1240 the TOB and the outer three TEC disks use silicon sensors of 500 μm thickness. The
 1241 silicon strips run parallel to the z -axis and the distance between strips varies from 80
 1242 μm in the inner TIB layers to 183 μm in the inner TOB layers; in the endcaps the
 1243 wedge-shaped sensors with radial strips, whose pitch range between 81 μm at small
 1244 radii and 205 μm at large radii.

1245 The whole SST has 15148 silicon modules, 9.3 million silicon strips and cover a
 1246 total active area of about 198 m^2 .

1247 3.3.4 Electromagnetic calorimeter

1248 The CMS electromagnetic calorimeter (ECAL) is designed to measure the energy of
 1249 electrons and photons. It is composed of 75848 lead tungstate crystals which have a

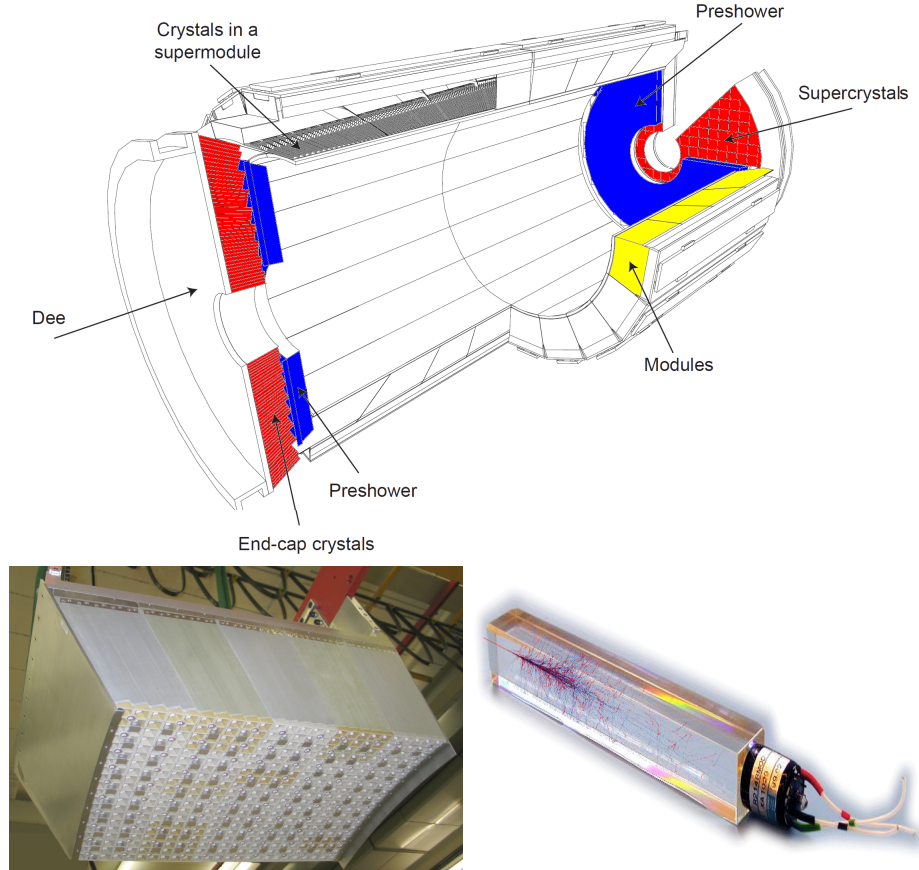


Figure 3.15: Top: CMS ECAL schematic view. Bottom: Module equipped with the crystals (left); ECAL crystal(right) with an artistic representation of an electromagnetic shower [72].

1250 short radiation length (0.89 cm) and fast response, since 80% of the light is emitted
 1251 within 25 ns; however, they are combined with Avalanche photodiodes (APDs) as
 1252 photodetectors given that crystals themselves have a low light yield ($30\gamma/\text{MeV}$). A
 1253 schematic view of the ECAL is shown in Figure 3.15.

1254 Energy is measured when electrons and photons are absorbed by the crystals
 1255 which generates an electromagnetic *shower*, as seen in bottom right picture of the
 1256 Figure 3.15; the shower is seen as a *cluster* of energy which depending on the amount
 1257 of energy deposited can involve several crystals. The ECAL barrel (EB) covers the
 1258 region $|\eta| < 1.479$, using crystals of depth of 23 cm and $2.2 \times 2.2 \text{ cm}^2$ transverse

1259 section; the ECAL endcap (EE) covers the region $1.479 < |\eta| < 3.0$ using crystals of
 1260 depth 22 cm and transverse section of $2.86 \times 2.86 \text{ cm}^2$; the photodetectors used are
 1261 vacuum phototriodes (VPTs). Each EE is divided in two structures called *Dees*.

1262 The preshower detector (ES) is installed in front of the EE and covers the region
 1263 $1.653 < |\eta| < 2.6$. The ES provides a precise measurement of the position of electro-
 1264 magnetic showers, which allows to distinguish electrons and photon signals from π^0
 1265 decay signals. The ES is composed of a layer of lead radiators followed by a layer of
 1266 silicon strip sensors. The lead radiators initiate electromagnetic showers when reached
 1267 by photons and electrons, then, the strip sensors measure the deposited energy and
 1268 the transverse shower profiles. The full ES thickness is 20 cm.

1269 3.3.5 Hadronic calorimeter

1270 Hadrons are not absorbed by the ECAL² but by the hadron calorimeter (HCAL),
 1271 which is made of a combination of alternating brass absorber layers and silicon photo-
 1272 multiplier(SiPM) layers; therefore, particles passing through the scintillator material
 1273 produce showers, as in the ECAL, as a result of the inelastic scattering of the hadrons
 1274 with the detector material. Since the particles are not absorbed in the scintillator,
 1275 their energy is sampled; therefore the total energy is not measured but estimated from
 1276 the energy clusters, which reduces the resolution of the detector. Brass was chosen
 1277 as the absorber material due to its short interaction length ($\lambda_I = 16.42\text{cm}$) and its
 1278 non-magnetivity. Figure 3.16 shows a schematic view of the CMS HCAL.

1279 The HCAL is divided into four sections; the Hadron Barrel (HB), the Hadron
 1280 Outer (HO), the Hadron Endcap (HE) and the Hadron Forward (HF) sections. The
 1281 HB covers the region $0 < |\eta| < 1.4$, while the HE covers the region $1.3 < |\eta| < 3.0$.
 1282 The HF, made of quartz fiber scintillator and steel as absorption material, covers the

² Most hadrons are not absorbed, but few low-energy ones might be.

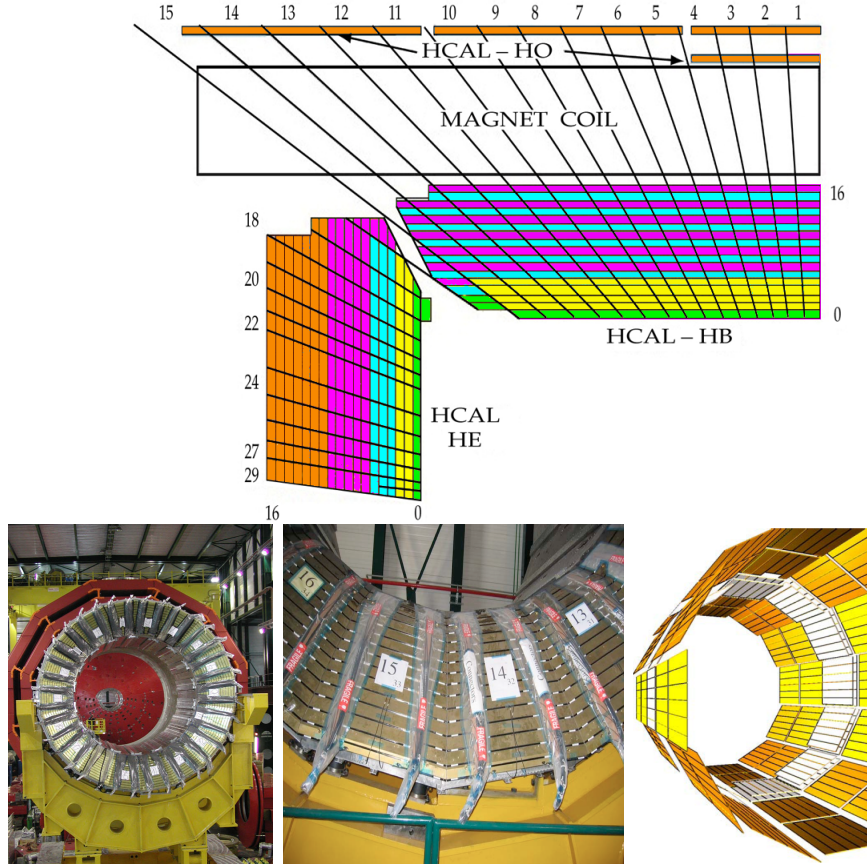


Figure 3.16: Top: CMS HCAL schematic view, the colors indicate the layers that are grouped into the same readout channels. Bottom: picture of a section of the HB; the absorber material is the golden region and scintillators are placed in between the absorber material (left and center). Schematic view of the HO (right). [81,82]

1283 forward region $3.0 < |\eta| < 5.2$. Both the HB and HF are located inside the solenoid.
 1284 The HO is placed outside the magnet as an additional layer of scintillators with the
 1285 purpose of measure the energy tails of particles passing through the HB and the
 1286 magnet (see Figure 3.16 top and bottom right).

1287 3.3.6 Superconducting solenoid magnet

1288 The superconducting magnet installed in the CMS detector is designed to provide
 1289 an intense and highly uniform magnetic field in the central part of the detector.

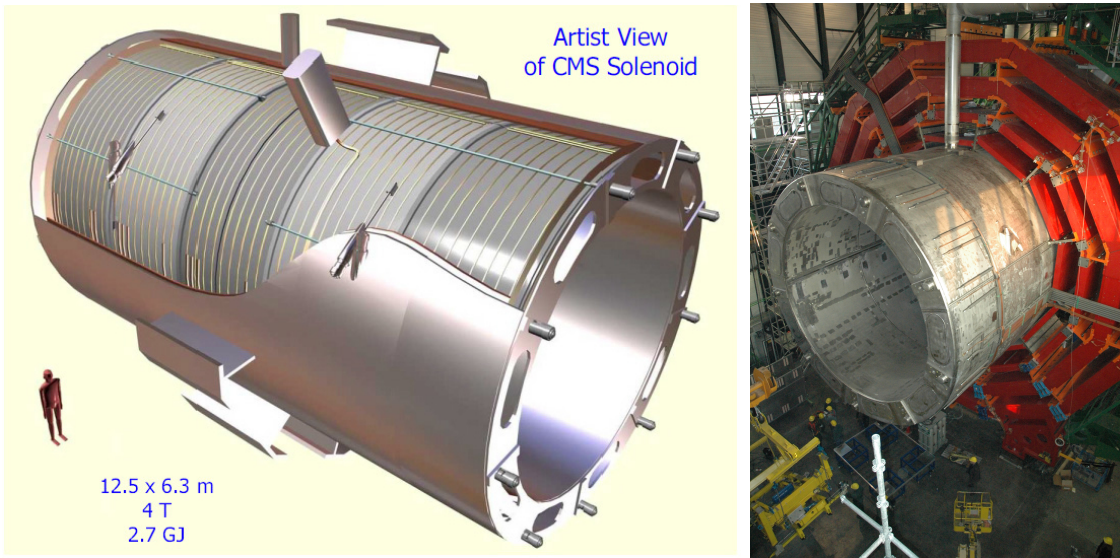


Figure 3.17: Artistic representation of the CMS solenoid magnet(left). The magnet is supported on an iron yoke (right) which also serves as the house of the muon detector and as mechanical support for the whole CMS detector [75].

1290 In fact, the tracking system takes advantage of the bending power of the magnetic
 1291 field to measure with precision the momentum of the particles that traverse it; the
 1292 unambiguous determination of the sign for high momentum muons was a driving
 1293 principle during the design of the magnet. The magnet has a diameter of 6.3 m, a
 1294 length of 12.5 m and a cold mass of 220 t; the generated magnetic field reaches a
 1295 strength of 3.8T. Since it is made of Ni-Tb superconducting cable it has to operate at
 1296 a temperature of 4.7 K by using a helium cryogenic system; the current circulating in
 1297 the cables reaches 18800 A under normal running conditions. The left side of Figure
 1298 3.17 shows an artistic view of the CMS magnet, while the right side shows a transverse
 1299 view of the cold mass where the winding structure is visible.

1300 The yoke (see Figure 3.17), composed of 5 barrel wheels and 6 endcap disks made
 1301 of iron, serves not only as the media for magnetic flux return but also provides housing
 1302 for the muon detector system and structural stability to the full detector.

1303 **3.3.7 Muon system**

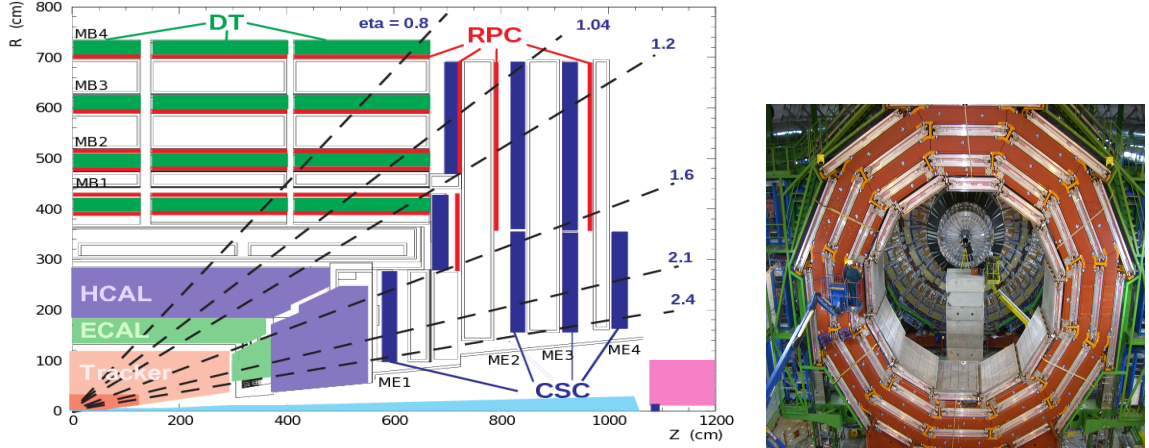


Figure 3.18: Left: CMS muon system schematic view; Right: one of the yoke rings with the muon DTs and RPCs installed; in the back it is possible to see the muon endcap [83].

1304 Muons are the only charged particles able to pass through all the CMS detector
 1305 due to their low ionization energy loss; thus, muons can be separated easily from the
 1306 high amount of particles produced in a pp collision. Also, muons are expected to be
 1307 produced in the decay of several new particles; therefore, good detection of muons
 1308 was one of the leading principles when designing the CMS detector.

1309 The CMS muon detection system (muon spectrometer) is embedded in the return
 1310 yoke as seen in Figure 3.18. It is composed of three different detector types, the drift
 1311 tube chambers (DT), cathode strip chambers (CSC), and resistive plate chambers
 1312 (RPC); DT are located in the central region $\eta < 1.2$ arranged in four layers of drift
 1313 chambers filled with an Ar/CO₂ gas mixture.

1314 The muon endcaps are made of CSCs covering the region $\eta < 2.4$ and filled with
 1315 a mixture of Ar/CO₂/CF₄. The reason behind using a different detector type lies on
 1316 the different conditions in the forward region like the higher muon rate and higher
 1317 residual magnetic field compared to the central region.

1318 The third type of detector used in the muon system is a set of four disks of RPCs

1319 working in avalanche mode. The RPCs provide good spatial and time resolutions. The
 1320 track of high- p_T muon candidates is built combining information from the tracking
 1321 system and the signal from up to six RPCs and four DT chambers.

1322 The muon tracks are reconstructed from the hits in the several layers of the muon
 1323 system.

1324 **3.3.8 CMS trigger system**

1325 CMS expects pp collisions every 25 ns, i.e., an interaction rate of 40 MHz for which
 1326 it is not possible to store the recorded data in full. In order to handle this high event
 1327 rate data, an online event selection, known as triggering, is performed; triggering
 1328 reduces the event rate to 100 Hz for storage and further offline analysis.

1329 The trigger system starts with a reduction of the event rate to 100 kHz in the
 1330 so-called *the level 1 trigger* (L1). L1 is based on dedicated programmable hardware
 1331 like Field Programmable Gate Arrays (FPGAs) and Application Specific Integrated
 1332 Circuits (ASICs), partly located in the detector itself; another portion is located in
 1333 the CMS underground cavern. Hit pattern information from the muon chambers
 1334 and the energy deposits in the calorimeter are used to decide if an event is accepted
 1335 or rejected, according to selection requirements previously defined, which reflect the
 1336 interesting physics processes. Figure 3.19 shows the L1 trigger architecture.

1337 The second stage in the trigger system is called *the high-level trigger* (HLT); events
 1338 accepted by L1 are passed to HLT in order to make an initial reconstruction of them.
 1339 HLT is software based and runs on a dedicated server farm, using selection algorithms
 1340 and high-level object definitions; the event rate at HLT is reduced to 100 Hz. The
 1341 first HLT stage takes information from the muon detectors and the calorimeters to
 1342 make the initial object reconstruction; in the next HLT stage, information from the

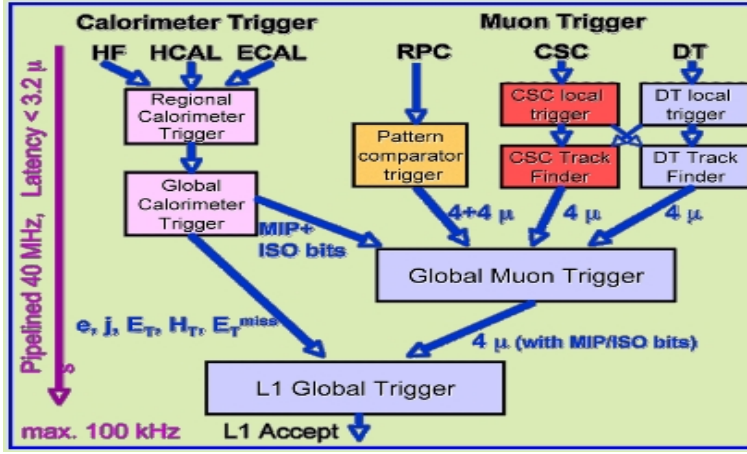


Figure 3.19: CMS Level-1 trigger architecture [84].

pixel and strip detectors is used to do first fast tracking and then full tracking online.

This initial object reconstruction is used in further steps of the trigger system.

Events and preliminary reconstructed physics objects from HLT are sent to be fully reconstructed at the CERN computing center known also as Tier-0 facility. Again, the pixel detector information provides high-quality seeds for the track reconstruction algorithm offline, primary vertex reconstruction, electron and photon identification, muon reconstruction, τ identification, and b-tagging. After full reconstruction, data sets are made available for offline analyses.

3.3.9 CMS computing

Data coming from the experiment have to be stored and made available for further analysis; in order to cope with all the tasks implied in the offline data processing, like transfer, simulation, reconstruction and reprocessing, among others, a large computing power is required. The CMS computing system is based on the distributed architecture concept, where users of the system and physical computer centers are distributed worldwide and interconnected by high-speed networks.

The worldwide LHC computing grid (WLCG) is the mechanism used to provide

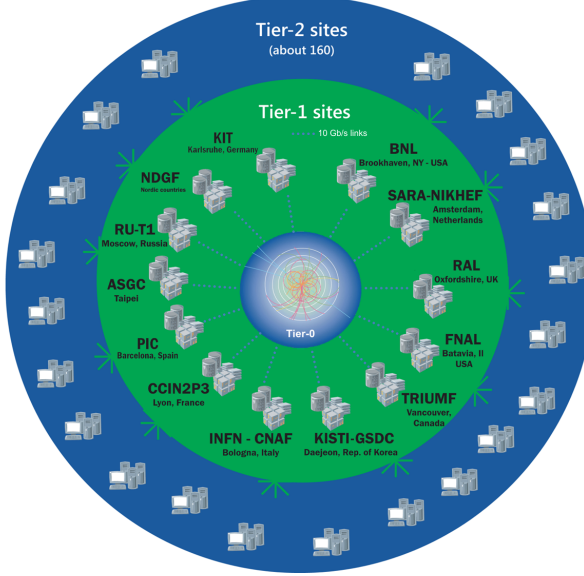


Figure 3.20: WLCG structure. The primary computer centers (Tier-0) are located at CERN (data center) and at the Wigner datacenter in Budapest. Tier-1 is composed of 13 centers and Tier-2 is composed of about 160 centers. [85].

1359 that distributed environment. WLCG is a tiered structure connecting computing
 1360 centers around the world, which provides the necessary storage and computing facil-
 1361 ities. The primary computing centers of the WLCG are located at the CERN and
 1362 the Wigner datacenter in Budapest and are known as Tier-0 as shown in Figure 3.20.
 1363 The main responsibilities for each tier level are [85]

- 1364 • **Tier-0:** initial reconstruction of recorded events and storage of the resulting
 1365 datasets, the distribution of raw data to the Tier-1 centers.
- 1366 • **Tier-1:** provide storage capacity, support for the Grid, safe-keeping of a pro-
 1367 portional share of raw and reconstructed data, large-scale reprocessing and safe-
 1368 keeping of corresponding output, generation of simulated events, distribution
 1369 of data to Tier 2s, safe-keeping of a share of simulated data produced at these
 1370 Tier 2s.
- 1371 • **Tier-2:** store sufficient data and provide adequate computing power for spe-

1372 cific analysis tasks and proportional share of simulated event production and
1373 reconstruction.

1374 Aside from the general computing strategy to manage the huge amount of data
1375 produced by experiments, CMS uses a software framework to perform a variety of
1376 processing, selection and analysis tasks. The central concept of the CMS data model
1377 referred to as *event data model* (EDM) is the *Event*; therefore, an event is the unit
1378 that contains the information from a single bunch crossing, any data derived from
1379 that information like the reconstructed objects, and the details of the derivation.

1380 Events are passed as the input to the *physics modules* that obtain information
1381 from them and create new information; for instance, *event data producers* add new
1382 data into the events, *analyzers* produce an information summary from an event set,
1383 *filters* perform selection and triggering.

1384 CMS uses several event formats with different levels of detail and precision

1385 • **Raw format:** events in this format contain the full recorded information from
1386 the detector as well as trigger decision and other metadata. An extended version
1387 of raw data is used to store information from the CMS Monte Carlo simulation
1388 tools (see Chapter 4). Raw data are stored permanently, occupying about
1389 2MB/event

1390 • **RECO format:** events in this format correspond to raw data that have been
1391 submitted to reconstruction algorithms like primary and secondary vertex re-
1392 construction, particle ID, and track finding. RECO events contain physics ob-
1393 jects and all the information used to reconstruct them; average size is about 0.5
1394 MB/event.

- 1395 • **AOD format:** Analysis Object Data (AOD) is the data format used in the
 1396 physics analyses given that it contains the parameters describing the high-level
 1397 physics objects in addition to enough information to allow a kinematic refitting if
 1398 needed. AOD events are filtered versions of the RECO events to which skimming
 1399 or other filtering have been applied, hence AOD events are subsets of RECO
 1400 events. Requires about 100 kB/event.
- 1401 • **Non-event data** are data needed to interpret and reconstruct events. Some
 1402 of the non-event data used by CMS contains information about the detector
 1403 contraction and condition data like calibrations, alignment, and detector status.

1404 Figure 3.21 shows the data flow scheme between CMS detector and tiers.

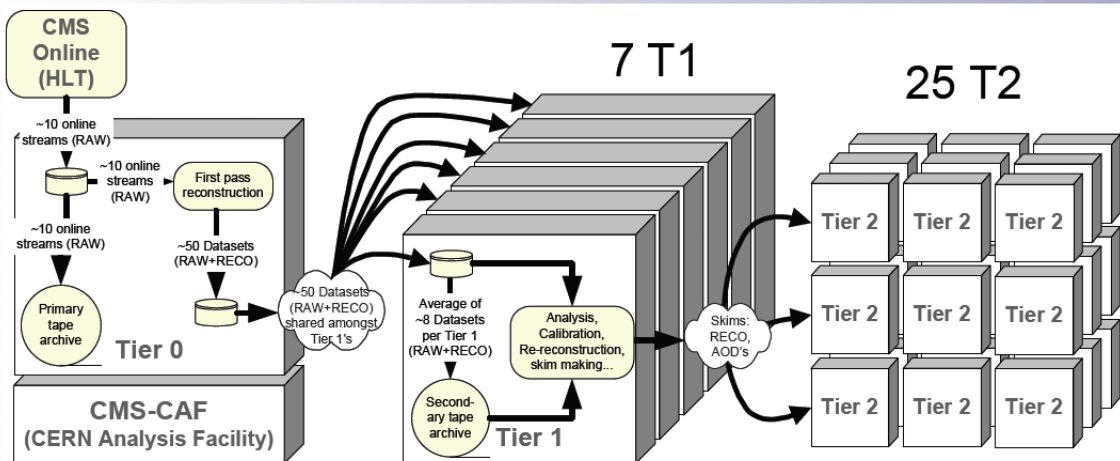


Figure 3.21: Data flow from CMS detector through tiers.

1405 The whole collection of software built as a framework is referred to as *CMSSW*. This
 1406 framework provides the services needed by the simulation, calibration and alignment,
 1407 and reconstruction modules that process event data, so that physicists can perform
 1408 analysis. The CMSSW event processing model is composed of one executable, called
 1409 `cmsRun`, and several plug-in modules which contains all the tools (calibration, recon-

1410 struction algorithms) needed to process an event. The same executable is used for
1411 both detector data and Monte Carlo simulations [86].

1412 **Chapter 4**

1413 **Event generation, simulation and
1414 reconstruction**

1415 The analysis of data recorded by the CMS experiment involves several stages of
1416 data processing in order to interpret the information provided by all the detection
1417 systems; in those stages, the particles produced after the pp collision are identified by
1418 reconstructing their trajectories and measuring their features. In addition, the SM
1419 provides a set of predictions that have to be compared with the experimental results;
1420 however, in most of the cases, theoretical predictions are not directly comparable
1421 to experimental results due to the diverse source of uncertainties introduced by the
1422 experimental setup and theoretical approximations, among others.

1423 The strategy to face these conditions consists of the implementation of theoretical
1424 models and statistical methods in computational algorithms to produce numerical
1425 results that can be compared with the experimental results. These computational
1426 algorithms are commonly known as Monte Carlo (MC) methods and, in the case of
1427 particle physics, they are designed to apply the SM rules and produce predictions
1428 about the physical observables measured in the experiments. Since particle physics is

1429 governed by quantum mechanics principles, predictions cannot be made from single
 1430 events; therefore, a high number of events are *generated* and predictions are produced
 1431 in the form of statistical distributions for the observables. Effects of the detector
 1432 presence are included in the predictions by introducing simulations of the detector
 1433 itself.

1434 This chapter presents a description of the event generation strategy and the tools
 1435 used to perform the detector simulation and physics object reconstruction. A com-
 1436 prehensive review of event generators for LHC physics can be found in Reference [87]
 1437 on which this chapter is based.

1438 4.1 Event generation

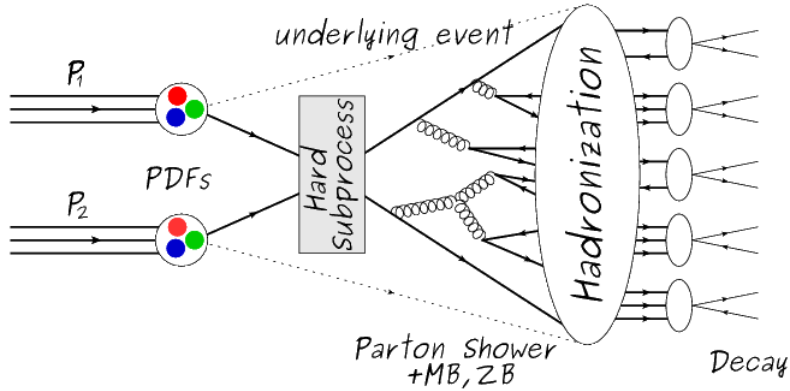


Figure 4.1: Event generation process. The actual interaction is generated in the hard subprocess while the parton shower describes the evolution of the partons from the hard subprocess. Modified from Reference [88].

1439 The event generation is intended to simulate events that mimic the behavior of
 1440 actual events produced in collisions; they obey a sequence of steps from the particle
 1441 collision hard process to the decay process into the final state. Figure 4.1 shows a
 1442 schematic view of the event generation process; the fact that the full process can be
 1443 treated as several independent steps is motivated by the QCD factorization theorem.

1444 Generation starts by taking into account the PDFs of the incoming particles.
 1445 Event generators offer the option to chose from several PDF sets depending on the
 1446 particular process under simulation¹; in the following, pp collisions will be consid-
 1447 ered. The *hard subprocess* describes the actual interaction between partons from the
 1448 incoming protons; it is represented by the matrix element connecting the initial and
 1449 final states of the interaction. Normally, the matrix element can be written as a sum
 1450 over Feynman diagrams with interferences between terms considered in the summa-
 1451 tion. During the generation of the hard subprocess, the production cross section is
 1452 calculated.

1453 The order of the Feynman diagrams involved in the calculation, i.e. the order in
 1454 the perturbation series, determine the order to which the cross section is calculated;
 1455 therefore, radiative corrections are included by considering higher order Feynman
 1456 diagrams where QCD radiation dominates. Currently, cross sections calculated to LO
 1457 do not offer a satisfactory description of the processes, i.e., the results are only reliable
 1458 for the shape of distributions; therefore, NLO calculations have to be performed with
 1459 the implication that the computing time needed is highly increased due to increment
 1460 in the number of diagrams involved and their complexity.

1461 The final parton content of the hard subprocess is subjected to the *parton shower*
 1462 which generates the gluon radiation. Parton showering evolves the partons, i.e., gluons
 1463 split into quark-antiquark pairs and quarks with enough energy radiate gluons giv-
 1464 ing rise to further parton multiplication, following the DGLAP (Dokshitzer-Gribov-
 1465 Lipatov-Altarelli-Parisi) equations [90–92]. Showering continues until the energy scale
 1466 is low enough to reach the non-perturbative limit.

1467 In the simulation of LHC processes that involve b quarks, like the single top quark
 1468 or Higgs associated production, it is necessary to consider that the b quark is heavier

¹ Different PDF sets under customizable conditions can be plotted using the tool in Reference [89].

1469 than the proton; hence, the QCD interaction description is made in two different
 1470 schemes [93]

- 1471 • four-flavor (4F) scheme. b quarks appear only in the final state because they
 1472 are heavier than the proton and therefore they can be produced only from the
 1473 splitting of a gluon into pairs or singly in association with a t quark in high
 1474 energy-scale interactions; hence, during the simulation, the b -PDFs are set to
 1475 zero. Calculations in this scheme are more complicated due to the presence
 1476 of the second b quark but the full kinematics is considered already at LO and
 1477 therefore the accuracy of the description is better.

- 1478 • five-flavor (5F) scheme. b quarks are considered massless, therefore they can
 1479 appear in both initial and final states since they can now be part of the proton;
 1480 thus, during the simulation b -PDFs are not set to zero. In this scheme, calcula-
 1481 tions are simpler than in the 4F scheme and possible logarithmic divergences
 1482 are absorbed by the PDFs through the DGLAP evolution.

1483 In this thesis, the tHq events are generated using the 4F scheme in order to reduce
 1484 uncertainties, while the tHW events are generated using the 5F scheme to eliminate
 1485 LO interference with $t\bar{t}H$ process [53].

1486 Partons involved in the pp collision are the focus of the simulation, however, the
 1487 rest of the partons inside the incoming protons are also affected because the remnants
 1488 are colored objects; also, multiple parton interactions can occur. The hadronization
 1489 of the remnants and multiple parton interactions are known as *underlying event* and
 1490 it has to be included in the simulation. In addition, multiple pp collisions in the same
 1491 bunch crossing (pile-up mentioned in 3.2) occurs, actually in two forms

1492 • *in-time PU* which refers to multiple pp collision in the bunch crossing but that
 1493 are not considered as primary vertices.

1494 • *out-of-time PU* which refers to overlapping pp collisions from consecutive bunch
 1495 crossings; this can occur due to the time delays in the detection systems where
 1496 information from one bunch crossing is assigned to the next or previous one.

1497 While the underlying event effects are included in generation using generator-
 1498 specific tools, PU effects are added to the generation by overlaying minimum-bias
 1499 (MB) and zero-bias (ZB) events to the generated events. MB events are inelastic
 1500 events from real detector data selected by using a loose trigger with as little bias as
 1501 possible, therefore accepting a large fraction of the overall inelastic event; ZB events
 1502 correspond to random events recorded by the detector when collisions are likely. MB
 1503 models in-time PU and ZB models out-of-time PU.

1504 The next step in the generation process is called *hadronization*. Since particles
 1505 with a net color charge are not allowed to exits in isolation, they have to recombine
 1506 to form bound states. This is precisely the process by which the partons resulting
 1507 from the parton shower arrange themselves as color singlets to form hadrons. At
 1508 this step, the energy-scale is low and the strong coupling constant is large, therefore
 1509 hadronization process is non-perturbative and the evolution of the partons is described
 1510 using phenomenological models. Most of the baryons and mesons produced in the
 1511 hadronization are unstable and hence they will decay in the detector.

1512 The last step in the generation process corresponds to the decay of the unstable
 1513 particles generated during hadronization; it is also simulated in the hadronization
 1514 step, based on the known branching ratios.

1515 The generated MC sample is characterized by the number of events in the sample
 1516 and the cross section of the simulated process, related by the luminosity as $\sigma =$

1517 $N_{events}L$; since the cross section of the process is fixed, the luminosity of the MC
 1518 sample varies with the number of events in it. In order to perform a simulation
 1519 at a given luminosity, it is necessary to *weight* the MC sample to the corresponding
 1520 experimental luminosity of interest, such that it would be possible to make predictions
 1521 like the number of events of signal or background that will be produced in a data
 1522 sample corresponding to that luminosity. In this sense, the weight is the ratio between
 1523 the desired luminosity and the original MC sample luminosity. In some cases, a
 1524 similar weighting strategy is used to evaluate the matching between the observed and
 1525 expected yields in a sample.

1526 **4.2 Monte Carlo Event Generators**

1527 The event generation described in the previous section has been implemented in
 1528 several software packages for which a brief description is given in the following.

- 1529 • **PYTHIA 8.** This program is designed to perform the generation of high
 1530 energy physics events that describes the collisions between particles such as
 1531 electrons and protons. Several theories and models are implemented in it, in
 1532 order to describe physical aspects like hard and soft interactions, parton dis-
 1533 tributions, initial and final-state parton showers, multiple parton interactions,
 1534 beam remnants, hadronization² and particle decay. Thanks to extensive test-
 1535 ing, several optimized parametrizations, known as *tunings*, have been defined
 1536 in order to improve the description of actual collisions to a high degree of pre-
 1537 cision; for analysis at $\sqrt{s} = 13$ TeV, the underlying event CUETP8M1 tune is
 1538 employed [95]. The calculation of the matrix element is performed at LO which
 1539 is not enough for the current required level of precision; therefore, PYTHIA

² based in the Lund string model [94]

1540 is often used for parton shower, hadronization and decays, while other event
 1541 generators are used to generate the matrix element at NLO.

- 1542 • **MadGraph5_aMC@NLO.** MadGraph is a matrix element generator which
 1543 calculates the amplitudes for all contributing Feynman diagrams of a given
 1544 process but does not provide a parton shower while MC@NLO incorporates
 1545 NLO QCD matrix elements consistently into a parton shower framework; thus,
 1546 MadGraph5_aMC@NLO, as a merger of the two event generators MadGraph5
 1547 and aMC@NLO, is an event generator capable to calculate tree-level and NLO
 1548 cross sections and perform the matching of those with the parton shower. It is
 1549 one of the most frequently used matrix element generators; however, it has the
 1550 particular feature of the presence of negative event weights which reduce the
 1551 number of events used to reproduce the properties of the objects generated [96].

- 1552 • **POWHEG.** It is an NLO matrix element generator where the hardest emis-
 1553 sion of color charged particles is generated in such a way that the negative event
 1554 weights issue of MadGraph5_aMC@NLO is overcome; however, the method re-
 1555 quires an interface with a parton shower generator where this highest emission
 1556 can be vetoed in order to avoid double counting of this highest-energetic emis-
 1557 sion. PYTHIA is a commonly matched to POWHEG event generator [97].

1558 Events resulting from the whole generation process are known as MC events.

1559 4.3 CMS detector simulation

1560 After generation, MC events contain the physics of the collisions but they are not
 1561 ready to be compared to the events recorded by the experiment since these recorded
 1562 events correspond to the response of the detection systems to the interaction with

1563 the particles traversing them. The simulation of the CMS detector has to be applied
1564 on top of the event generation; it is simulated with a MC toolkit for the simulation
1565 of particles passing through matter called Geant4 [98] which is also able to simulate
1566 the electronic signals that would be measured by all detectors inside CMS.

1567 The simulation takes the generated particles contained in the MC events as input,
1568 makes them pass through the simulated geometry, and models physics processes that
1569 particles experience during their passage through matter. The full set of results from
1570 particle-matter interactions corresponds to the *simulated hit*, which contains informa-
1571 tion about the energy loss, momentum, and position. Particles of the input event are
1572 called *primary*, while the particles originating from GEANT4-modeled interactions
1573 of primary particles with matter are called *secondary*. Simulated hits are the input
1574 of subsequent modules that emulate the response of the detector readout system and
1575 triggers. The output from the emulated detection systems and triggers is known as
1576 digitization [98, 99].

1577 The modeling of the CMS detector corresponds to the accurate modeling of the
1578 interaction among particles, the detector material, and the magnetic field. This
1579 simulation procedure includes the following standard steps

- 1580 • Modeling of the Interaction Region.
- 1581 • Modeling of the particle passage through the hierarchy of volumes that compose
1582 CMS detector and of the accompanying physics processes.
- 1583 • Modeling of the effect of multiple interactions per beam crossing and/or the
1584 effect of events overlay (pile-up simulation).
- 1585 • Modeling of the detector's electronics response, signal shape, noise, calibration
1586 constants (digitization).

1587 In addition to the full simulation, i.e., a detailed detector simulation, a faster
 1588 simulation (FastSim) have been developed, that may be used where much larger
 1589 statistics are required. In FastSim, detector material effects are parametrized and
 1590 included in the hits; those hits are used as input of the same higher-level algorithms³
 1591 used to analyze the recorded events. In this way, comparisons between fast and full
 1592 simulations can be performed [101].

1593 After the full detector simulation, the output events can be directly compared
 1594 to events actually recorded in the CMS detector. The collection of MC events that
 1595 reproduces the expected physics for a given process is known as MC sample.

1596 4.4 Event reconstruction

1597 The CMS experiment use the *particle-flow event reconstruction algorithm (PF)* to do
 1598 the reconstruction of particles produced in pp collisions. Next sections will present
 1599 a basic description of the *elements* used by PF (tracker tracks, energy clusters, and
 1600 muon tracks), based on the References [102, 103] where more detailed descriptions can
 1601 be found.

1602 4.4.1 Particle-Flow Algorithm

1603 Each of the several subdetector systems of the CMS detector is dedicated to identify
 1604 a specific type of particle, i.e., photons and electrons are absorbed by the ECAL
 1605 and their reconstruction is based on ECAL information; hadrons are reconstructed
 1606 from clusters in the HCAL while muons are reconstructed from hits in the muon
 1607 chambers. PF is designed to correlate signals from all the detector layers (tracks and

³ track fitting, calorimeter clustering, b tagging, electron identification, jet reconstruction and calibration, trigger algorithms which will be considered in the next sections

1608 energy clusters) in order to reconstruct and identify each final state particle and its
 1609 properties as sketched in Figure 4.2.

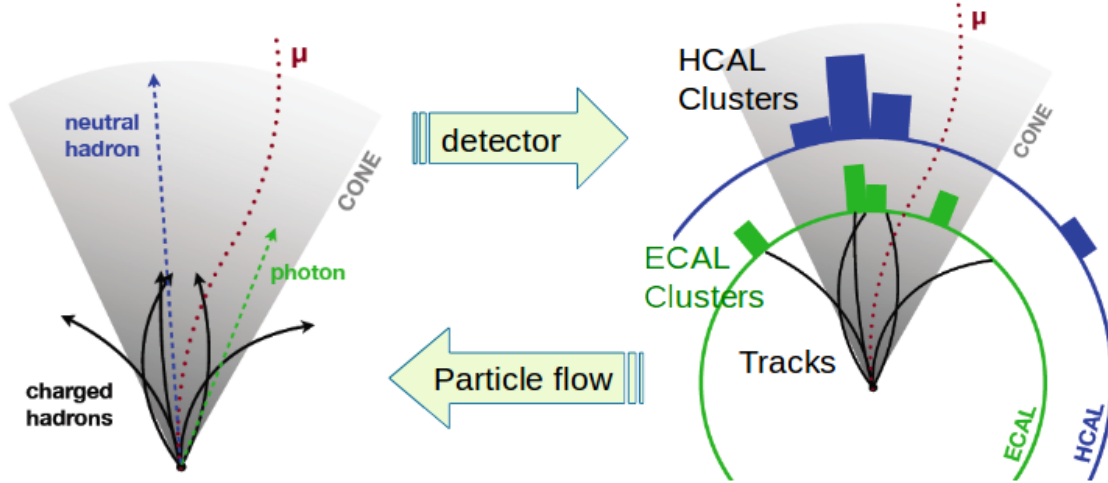


Figure 4.2: Particle flow algorithm. Information from the several CMS detection systems is provided as input to the algorithm which then combines it to identify and reconstruct all the particles in the final state and their properties. Reconstruction of simulated events is also performed by providing information from MC samples, detector and trigger simulation [104].

1610 For instance, a charged hadron is identified by a geometrical connection, known
 1611 as *link*, between one or more calorimeter clusters and a track in the tracker, provided
 1612 there are no hits in the muon system; combining several measurements allows a better
 1613 determination of the energy and charge sign of the charged hadron.

1614 Charged-particle track reconstruction

1615 The strategy used by PF in order to reconstruct tracks is called *Iterative Tracking*
 1616 which occurs in four steps:

- 1617 • Seed generation where initial track candidates are found by looking for a combi-
 1618 nation of hits in the pixel detector, strip tracker, and muon chambers. In total
 1619 ten iterations are performed, each one with a different seeding requirement.

1620 Seeds are used to estimate the trajectory parameters and uncertainties at the
 1621 time of the full track reconstruction. Seeds are also considered track candidates.

- 1622 ● Track finding using a tracking software known as Combinatorial Track Finder
 (CTF) [105]. The seed trajectories are extrapolated along the expected flight
 path of a charged particle, in agreement to the trajectory parameters obtained
 in the first step, in an attempt to find additional hits that can be assigned to
 the track candidates.
- 1627 ● Track fitting where the found tracks are passed as input to a module which
 provides the best estimate of the parameters of each trajectory.
- 1629 ● Track selection where track candidates are submitted to a selection which dis-
 cards those that fail a set of defined quality criteria.

1631 Iterations differ in the seeding configuration and the final track selection as elab-
 1632 orated in References [102, 103]. In the first iteration, high- p_T tracks and tracks pro-
 duced near to the interaction region are identified and those hits are masked thereby
 reducing the combinatorial complexity. Next, iterations search for more complicated
 tracks, like low- p_T tracks and tracks from b hadron decays, which tend to be displaced
 from the interaction region.

1637 Vertex reconstruction

1638 During the track reconstruction, an extrapolation toward to the calorimeters is per-
 1639 formed in order to match energy deposits; that extrapolation is also performed toward
 the beamline in order to find the origin of the track known as *vertex*. The vertex re-
 construction is performed by selecting from the available reconstructed tracks those
 1642 that are consistent with being originated in the interaction region where pp collisions

1643 are produced. The selection involves a requirement on the number of tracker (pixel
 1644 and strip) hits and the goodness of the track fit.

1645 Selected tracks are clustered using a *deterministic annealing algorithm* (DA)⁴. A
 1646 set of candidate vertices and their associated tracks, resulting from the DA, are then
 1647 fitted with an *adaptive vertex fitter* (AVF) to produce the best estimate of the vertices
 1648 locations.

1649 The p_T of the tracks associated to a reconstructed vertex is added, squared and
 1650 used to organize the vertices; the vertex with the highest squared sum is designated
 1651 as the *primary vertex* (*PV*) while the rest are designated as PU vertices.

1652 Calorimeter clustering

1653 After traversing the CMS tracker system, electrons, photons and hadrons deposit their
 1654 energy in the ECAL and HCAL cells. The PF clustering algorithm aims to provide
 1655 a high detection efficiency even for low-energy particles and an efficient distinction
 1656 between close energy deposits. The clustering runs independently in the ECAL barrel
 1657 and endcaps, HCAL barrel and endcaps, and the two preshower layers, following two
 1658 steps:

1659 • cells with an energy larger than a given seed threshold and larger than the energy
 1660 of the neighboring cells are identified as cluster seeds. The neighbor cells are
 1661 those that either share a side with the cluster seed candidate, or the eight closest
 1662 cells including cells that only share a corner with the seed candidate.

1663 • cells with at least a corner in common with a cell already in the cluster seed
 1664 and with an energy above a cell threshold are grouped into topological clusters.

⁴ DA algorithm and AVF are described in detail in References [107, 108]

1665 Clusters formed in this way are known as *particle-flow clusters*. With this cluster-
 1666 ing strategy, it is possible to detect and measure the energy and direction of photons
 1667 and neutral hadrons as well as differentiate these neutral particles from the charged
 1668 hadron energy deposits. In cases involving charged hadrons for which the track pa-
 1669 rameters are not determined accurately, for instance, low-quality and high- p_T tracks,
 1670 clustering helps in the energy measurements.

1671 Electron track reconstruction

1672 Although the charged-particle track reconstruction described above works for elec-
 1673 trons, they lose a significant fraction of their energy via bremsstrahlung photon radi-
 1674 ation before reaching the ECAL; thus, the reconstruction performance depends on the
 1675 ability to measure also the radiated energy. The reconstruction strategy, in this case,
 1676 requires information from the tracking system and from the ECAL. Bremsstrahlung
 1677 photons are emitted at similar η values to that of the electron but at different values
 1678 of ϕ ; therefore, the radiated energy can be recovered by grouping ECAL clusters in a
 1679 η window over a range of ϕ around the electron direction. The group is called ECAL
 1680 supercluster.

1681 Electron candidates from the track-seeding and ECAL super clustering are merged
 1682 into a single collection which is submitted to a full electron tracking fit with a
 1683 Gaussian-sum filter (GSF) [106]. The electron track and its associated ECAL su-
 1684 percluster form a *particle-flow electron*.

1685 Muon track reconstruction

1686 Given that the CMS detector is equipped with a muon spectrometer capable of iden-
 1687 tifying and measuring the momentum of the muons traversing it, the muon recon-
 1688 struction is not specific to PF; therefore, three different muon types are defined:

- 1689 • *Standalone muon.* A clustering of the DTs or CSCs hits is performed to form
 1690 track segments; those segments are used as seeds for the reconstruction in the
 1691 muon spectrometer. All DTs, CSCs, and RPCs hits along the muon trajectory
 1692 are combined and fitted to form the full track. The fitting output is called a
 1693 *standalone-muon track*.
- 1694 • *Tracker muon.* Each track in the inner tracker with p_T larger than 0.5 GeV and
 1695 a total momentum p larger than 2.5 GeV is extrapolated to the muon system.
 1696 A *tracker muon track* corresponds to a extrapolated track that matches at least
 1697 one muon segment.
- 1698 • *Global muon.* When tracks in the inner tracker (inner tracks) and standalone-
 1699 muon tracks are matched and turn out to be compatible, their hits are combined
 1700 and fitted to form a *global-muon track*.
- 1701 Global muons sharing the same inner track with tracker muons are merged into
 1702 a single candidate. PF muon identification uses the muon energy deposits in ECAL,
 1703 HCAL, and HO associated with the muon track to improve the muon identification.

1704 Particle identification and reconstruction

1705 PF elements are connected by a linker algorithm that tests the connection between
 1706 any pair of elements; if they are found to be linked, a geometrical distance that
 1707 quantifies the quality of the link is assigned. Two elements may be linked indirectly
 1708 through common elements. Linked elements form *PF blocks* and each PF block may
 1709 contain elements originating from one or more particles. Links can be established
 1710 between tracks, between calorimeter clusters, and between tracks and calorimeter
 1711 clusters. The identification and reconstruction start with a PF block and proceed as
 1712 follows:

1713 • Muons. An *isolated global muon* is identified by evaluating the presence of
 1714 inner track and energy deposits close to the global muon track in the (η, ϕ)
 1715 plane, i.e., at a particular point of the global muon track, inner tracks and
 1716 energy deposits are sought within a radius of $\Delta R = 0.3$ (see eqn. 3.7) from the
 1717 muon track; if they exit and the p_T of the found track added to the E_T of the
 1718 found energy deposit does not exceed 10% of the muon p_T then the global muon
 1719 is an isolated global muon. This isolation condition is stringent enough to reject
 1720 hadrons misidentified as muons.

1721 *Non-isolated global muons* are identified using additional selection requirements
 1722 on the number of track segments in the muon system and energy deposits along
 1723 the muon track. Muons inside jets are identified with more stringent criteria
 1724 in isolation and momentum as described in Reference [109]. The PF elements
 1725 associated with an identified muon are masked from the PF block.

1726 • Electrons are identified and reconstructed as described above plus some addi-
 1727 tional requirements on fourteen variables like the amount of energy radiated,
 1728 the distance between the extrapolated track position at the ECAL and the po-
 1729 sition of the associated ECAL supercluster, among others, which are combined
 1730 in an specialized multivariate analysis strategy that improves the electron iden-
 1731 tification. Tracks and clusters used to identify and reconstruct electrons are
 1732 masked in the PF block.

1733 • Isolated photons are identified from ECAL superclusters with E_T larger than 10
 1734 GeV, for which the energy deposited at a distance of 0.15, from the supercluster
 1735 position on the (η, ϕ) plane, does not exceed 10% of the supercluster energy;
 1736 note that this is an isolation requirement. In addition, there must not be links
 1737 to tracks. Clusters involved in the identification and reconstruction are masked

1738 in the PF block.

- 1739 ● Bremsstrahlung photons and prompt photons tend to convert to electron-positron
 1740 pairs inside the tracker, therefore, a dedicated finder algorithm is used to link
 1741 tracks that seem to originate from a photon conversion; in case those two tracks
 1742 are compatible with the direction of a bremsstrahlung photon, they are also
 1743 linked to the original electron track. Photon conversion tracks are also masked
 1744 in the PF block.
- 1745 ● The remaining elements in the PF block are used to identify hadrons. In the
 1746 region $|\eta| \leq 2.5$, neutral hadrons are identified with HCAL clusters not linked
 1747 to any track while photons from neutral pion decays are identified with ECAL
 1748 clusters without links to tracks. In the region $|\eta| > 2.5$ ECAL clusters linked to
 1749 HCAL clusters are identified with a charged or neutral hadron shower; ECAL
 1750 clusters with no links are identified with photons. HCAL clusters not used yet,
 1751 are linked to one or more unlinked tracks and to an unlinked ECAL in order to
 1752 reconstruct charged-hadrons or a combination of photons and neutral hadrons
 1753 according to certain conditions on the calibrated calorimetric energy.
- 1754 ● Charged-particle tracks may be linked together when they converge to a *sec-
 1755 ondary vertex (SV)* displaced from the IP where the PV and PU vertices are
 1756 reconstructed; at least three tracks are needed in that case, of which at most
 1757 one has to be a track with hits in tracker region between a PV and the SV.

1758 The linker algorithm, as well as the whole PF algorithm, has been validated and
 1759 commissioned; results from that validation are presented in Reference [102].

1760 **Jet reconstruction**

1761 Quarks and gluons may be produced in the pp collisions, therefore, their hadronization
 1762 will be seen in the detector as a shower of hadrons and their decay products in the
 1763 form of a *jet*. The anti- k_t algorithm [110] is used to perform the jet reconstruction
 1764 by clustering those PF particles within a cone (see Figure 4.3); previously, isolated
 1765 electrons, isolated muons, and charged particles associated with other interaction
 1766 vertices were excluded from the clustering.

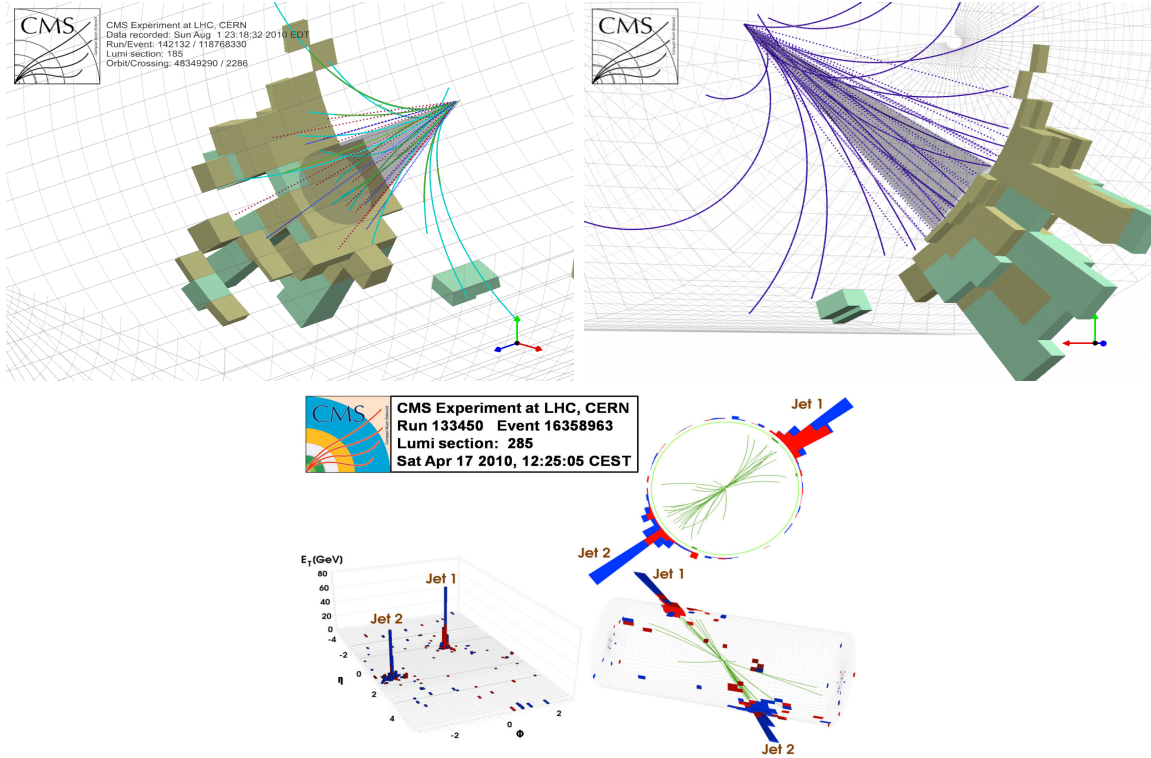


Figure 4.3: Jet reconstruction performed by the anti- k_t algorithm. Top: Two different views of a CMS recorded event are presented. Continuous lines correspond to tracks left by charged particles in the tracker while dotted lines are the imaginary paths followed by neutral particles. The green cubes represent the ECAL cells while the blue ones represent the HCAL cells; in both cases, the height of the cube represent the amount of energy deposited in the cells [111]. Bottom: Reconstruction of a recorded event with two jets [112].

1767 The anti- k_t algorithm proceeds in a sequential recombination of PF particles; the
 1768 distance between particles i and j (d_{ij}) and the distance between particles and the

1769 beam are defined as

$$d_{ij} = \min \left(\frac{1}{k_{ti}^2}, \frac{1}{k_{tj}^2} \right) \frac{\Delta_{ij}^2}{R^2}$$

$$d_{iB} = \frac{1}{k_{ti}^2} \quad (4.1)$$

1770 where $\Delta_{ij}^2 = (y_i - y_j)^2 + (\phi_i - \phi_j)^2$, k_{ti}, y_i and ϕ_i are the transverse momentum, ra-
 1771 pidity and azimuth of particle i respectively and R is the called jet radius. For all
 1772 the remaining PF particles, after removing the isolated ones, d_{ij} and d_{iB} are calcu-
 1773 lated⁵ and the smallest is identified; if it is a d_{ij} , particles i and j are replaced with
 1774 a new object whose momentum is the vectorial sum of the combined particles. If the
 1775 smallest distance is a d_{iB} the clustering process ends, the object i (which at this stage
 1776 should be a combination of several PF particles) is declared as a *Particle-flow-jet* (PF
 1777 jet) and all the associated PF particles are removed from the detector. The clustering
 1778 process is repeated until no PF particles remain.

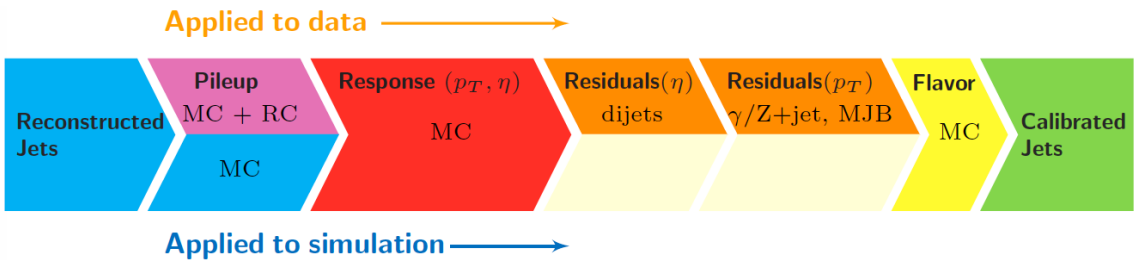


Figure 4.4: Jet energy correction diagram. Correction levels are applied sequentially in the indicated fixed order [114].

1779 Even though jets can be reconstructed efficiently, there are some effects that
 1780 are not included in the reconstruction that lead to discrepancies between the re-
 1781 constructed results and the predicted results; in order to overcome these discrep-

⁵ Notice that this is a combinatorial calculation.

1782 ancies, a factorized model has been designed in the form of jet energy corrections
 1783 (JEC) [113, 114] applied sequentially as shown in the diagram of Figure 4.4.

1784 At each level, the jet four-momentum is multiplied by a scale factor based on jet
 1785 properties, i.e., η , flavor, etc.

- 1786 • Level 1 correction removes the energy coming from pile-up. The scale factor is
 1787 determined using a MC sample of QCD dijet (2 jets) events with and without
 1788 pileup overlay; it is parametrized in terms of the offset energy density ρ , jet
 1789 area A , jet η and jet p_T . Different corrections are applied to data and MC due
 1790 to the detector simulation.
- 1791 • MC-truth correction accounts for differences between the reconstructed jet en-
 1792 ergy and the MC particle-level energy. The correction is determined on a QCD
 1793 dijet MC sample and is parametrized in terms of the jet p_T and η .
- 1794 • Residuals correct remaining small differences within jet response in data and
 1795 MC. The Residuals η -dependent correction compares jets of similar p_T in the
 1796 barrel reference region. The Residuals p_T -dependent corrects the jet absolute
 1797 scale (JES vs p_T).
- 1798 • Jet-flavor corrections are derived in the same way as MC-truth corrections but
 1799 using QCD pure flavor samples.

1800 ***b*-tagging of jets**

1801 A particular feature of the hadrons containing bottom quarks (b-hadrons) is that
 1802 their lifetime is long enough to travel some distance before decaying, but it is not as
 1803 long as those of light quark hadrons; therefore, when looking at the hadrons produced
 1804 in pp collisions, b-hadrons decay typically inside the tracker rather than reaching the

1805 calorimeters as some light-hadrons do. As a result, a b-hadron decay gives rise to a
 1806 displaced vertex (secondary vertex) with respect to the primary vertex as shown in
 1807 Figure 4.5; the SV displacement is in the order of a few millimeters. A jet resulting
 1808 from the decay of a b-hadron is called *b* jet; other jets are called light jets.

1809

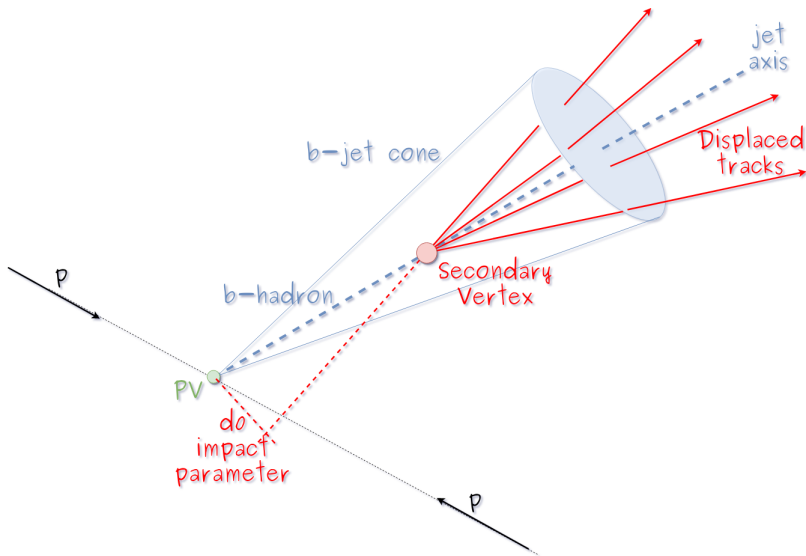


Figure 4.5: Secondary vertex in a b-hadron decay.

1810 Several methods to identify *b*-jets (*b*-tagging) have been developed; the method
 1811 used in this thesis is known as *Combined Secondary Vertex* algorithm in its second
 1812 version (CSVv2) [115]. By using information of the impact parameter, the recon-
 1813 structed secondary vertices, and the jet kinematics as input in a multivariate analysis
 1814 that combines the discrimination power of each variable in one global discrimina-
 1815 tor variable, three working points (references): loose, medium and tight, are defined
 1816 which quantify the probabilities of mistag jets from light quarks as jets from *b* quarks;
 1817 10, 1 and 0.1 % respectively. Although the mistagging probability decreases with the
 1818 working point strength, the efficiency to correctly tag *b*-jets also decreases as 83, 69
 1819 and 49 % for the respective working point; therefore, a balance needs to be achieved

1820 according to the specific requirements of the analysis.

1821 **4.4.1.1 Missing transverse energy**

1822 The fact that proton bunches carry momentum along the z -axis implies that for
 1823 each event it is expected that the momentum in the transverse plane is balanced.
 1824 Imbalances are quantified by the missing transverse energy (MET) and are attributed
 1825 to several sources including particles escaping undetected through the beam pipe,
 1826 neutrinos produced in weak interactions processes which do not interact with the
 1827 detector and thus escaping without leaving a sign, or even undiscovered particles
 1828 predicted by models beyond the SM.

1829 The PF algorithm assigns the negative sum of the momenta of all reconstructed
 1830 PF particles to the *particle-flow MET* according to

$$\vec{E}_T = - \sum_i \vec{p}_{T,i} \quad (4.2)$$

1831 JEC are propagated to the calculation of the \vec{E}_T as described in Reference [116].

1832 **4.4.2 Event reconstruction examples**

1833 Figures 4.6-4.8 show the results of the reconstruction performed on three recorded
 1834 events. Descriptions are taken directly from the source.

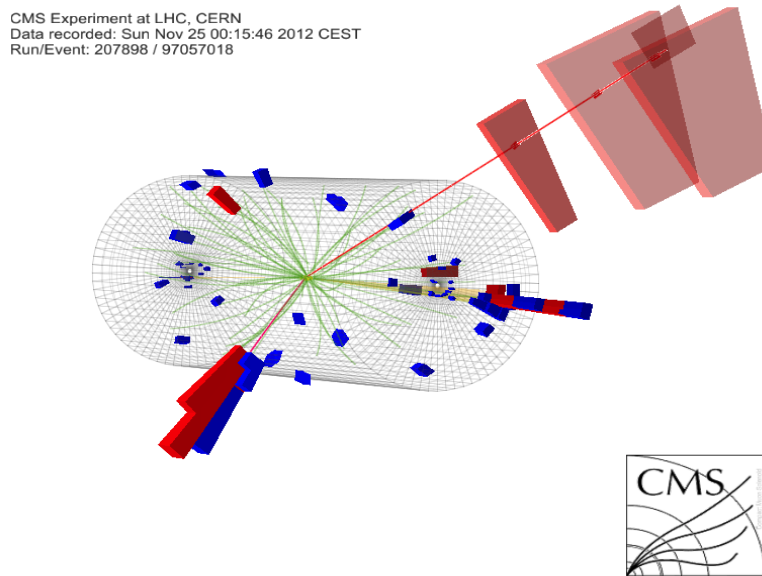


Figure 4.6: HIG-13-004 Event 1 reconstruction results; “HIG-13-004 Event 1: Event recorded with the CMS detector in 2012 at a proton-proton center-of-mass energy of 8 TeV. The event shows characteristics expected from the decay of the SM Higgs boson to a pair of τ leptons. Such an event is characterized by the production of two forward-going jets, seen here in opposite endcaps. One of the τ decays to a muon (red lines on the right) and neutrinos, while the other τ decays into a charged hadron and a neutrino.” [117].

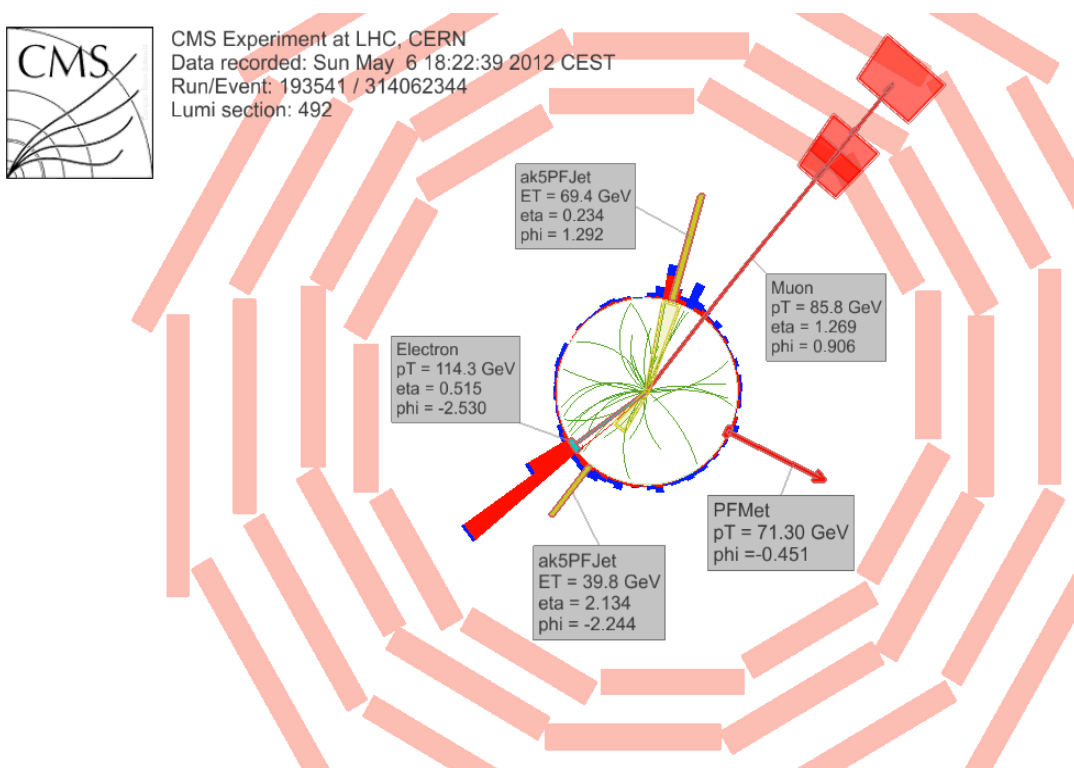


Figure 4.7: $e\mu$ event reconstruction results; “An $e\mu$ event candidate selected in 8 TeV data, as seen from the direction of the proton beams. The kinematics of the main objects used in the event selection are highlighted: two isolated leptons and two particle-flow jets. The reconstructed missing transverse energy is also displayed for reference” [118].

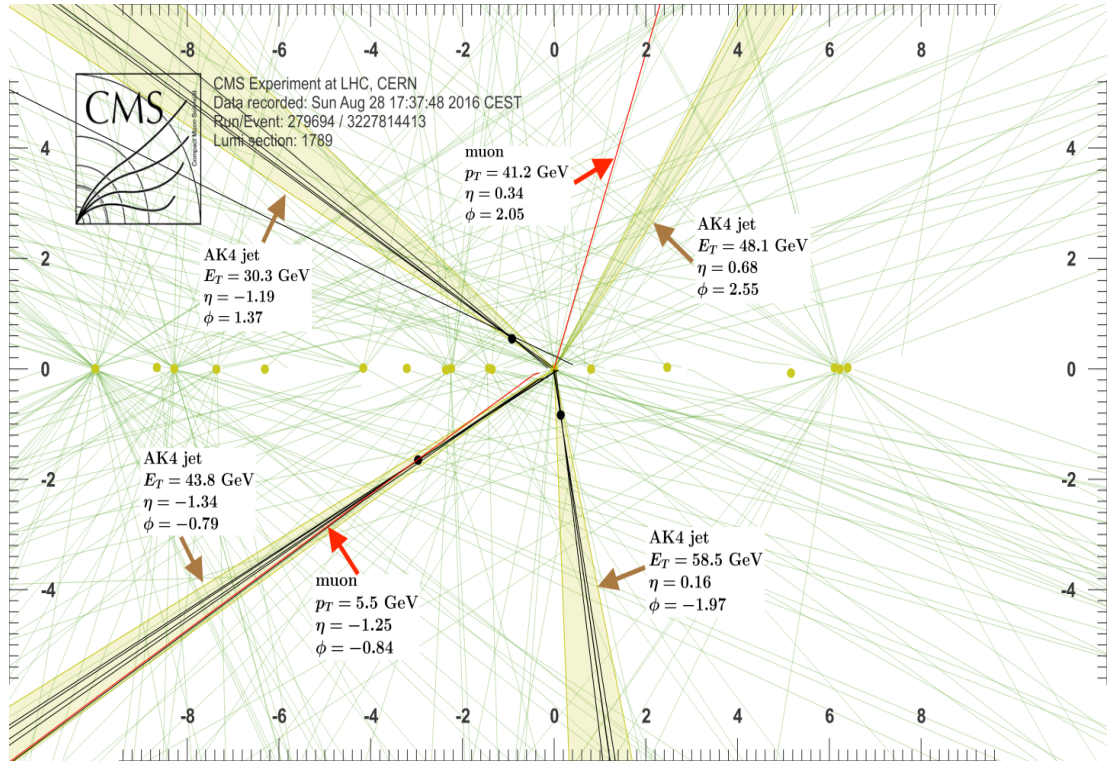


Figure 4.8: Recorded event reconstruction results;“Recorded event (ρ - z projection) with three jets with $p_T > 30$ GeV with one displaced muon track in 2016 data collected at 13 TeV. Each of the three jets has a displaced reconstructed vertex. The jet with $p_T(j) = 43.8$ GeV, $\eta(j) = -1.34$, $\phi(j) = -0.79$ contains muon with $p_T(\mu) = 5.5$ GeV, $\eta(\mu) = -1.25$, $\phi(\mu) = -0.84$. Event contains reconstructed isolated muon with $p_T(\mu) = 41.2$ GeV, $\eta(\mu) = 0.34$, $\phi(\mu) = 2.05$ and MET with $p_T = 72.5$ GeV, $\phi = -0.32$. Jet candidates for a b -jet from top quark leptonic and hadronic decays are tagged by CSVv2T algorithm. One of the other two jets is tagged by CharmT algorithm. Tracks with $p_T > 0.5$ GeV are shown. The number of reconstructed primary vertices is 18. Reconstructed $m_T(W)$ is 101.8 GeV. Beam spot position correction is applied. Reconstructed primary vertices are shown in yellow color, while reconstructed displaced vertices and associated tracks are presented in black color. Dimensions are given in cm” [119].

1835 **Chapter 5**

1836 **Statistical methods**

1837 In the course of analyzing the data sets provided by the CMS experiment and used in
1838 this thesis, several statistical tools have been employed; in this chapter, a description
1839 of these tools will be presented, starting with the general statement of the multivariate
1840 analysis method, followed by the particularities of the Boosted Decision Trees (BDT)
1841 method and its application to the classification problem. Statistical inference methods
1842 used will also be presented. This chapter is based mainly on the references [120–122].

1843 **5.1 Multivariate analysis**

1844 Multivariate data analysis (MVA) makes reference to statistical techniques that an-
1845 alyze data containing information of more than one variable, commonly taking into
1846 account the effects of all variables on the response of the particular variable under
1847 investigation, i.e., considering all the correlations between variables. MVA is em-
1848 ployed in a variety of fields like consumer and market research, quality control and
1849 process optimization. From a MVA it is possible to identify the dominant patterns
1850 in the data, like groups, outliers and trends, and determine to which group a set of

1851 values belong; in the particle physics context, MVA methods are used to perform the
 1852 selection of certain type of events, from a large data set, using a potentially large
 1853 number of measurable properties for each event.

1854 Processes with small cross section, as the tHq process, normally are hidden behind
 1855 more common processes; therefore, the data set results in a subset of events with
 1856 characteristic features of interest (signal) mixed in randomly with a much larger
 1857 number of SM events that can mimic these features of interest (background) which
 1858 implies that it is not possible to say with certainty that a given event is signal or
 1859 background. In that sense, the problem can be formulated as one where a set of
 1860 events have to be classified according to some features; these features correspond to
 1861 the measurements of several parameters like energy or momentum, organized in a
 1862 set of *input variables*. The measurements for each event can be written in a vector
 1863 $\mathbf{x} = (x_1, \dots, x_n)$ for which

- 1864 • Signal hypotheses $\rightarrow f(\mathbf{x}|s)$ is the probability density (*likelihood function*) that
 1865 \mathbf{x} is the set of measured values given that the events is a signal event.
- 1866 • Background hypotheses $\rightarrow f(\mathbf{x}|b)$ is the probability density (*likelihood function*)
 1867 that \mathbf{x} is the set of measured values given that the event is a background event.

1868 Figure 5.1 shows three ways to perform a classification of events for which mea-
 1869 surements of two properties, two input variables, have been performed; blue circles
 1870 represent signal events while red triangles represent background events. The classi-
 1871 fication on (a) is *cut-based* requiring $x_1 < c_1$ and $x_2 < c_2$; usually the cut values are
 1872 chosen according to some knowledge about the event process. In (b), the classification
 1873 is performed by stating a cut involving a linear function of the input variables and
 1874 so the boundary, while in (c) the the relationship between the input variables is not
 1875 linear thus the boundary is not linear either.

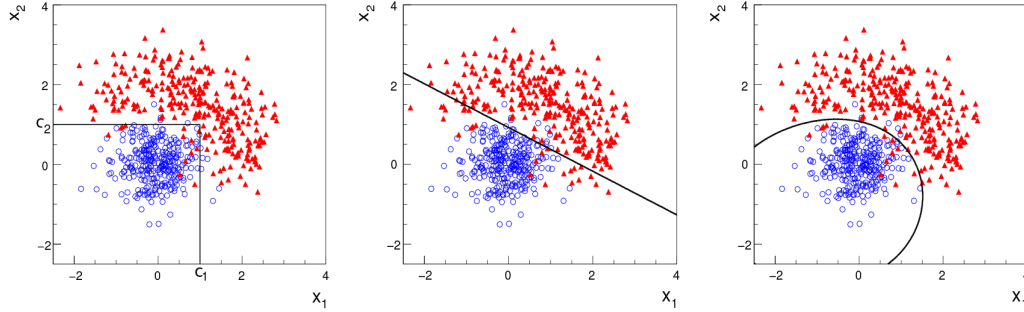


Figure 5.1: Scatter plots-MVA event classification. Distribution of two input variables x_1 and x_2 measured for a set of events; blue circles represent signal events and red triangles represent background events. The classification is based on (a) cuts, (b) linear boundary, and (c) nonlinear boundary [120]

1876 The boundary can be parametrized in terms of the input variables such that the
 1877 cut is set on the parametrization instead of on the variables, i.e., $y(\mathbf{x}) = y_{cut}$ with
 1878 y_{cut} a constant; thus, the acceptance or rejection of an event is based on what side
 1879 of the boundary is the event located. If $y(\mathbf{x})$ has functional form, it can be used to
 1880 determine the probability distribution functions $p(y|s)$ and $p(y|b)$ and then perform
 1881 a scalar test statistic with a single cut on the scalar variable y .

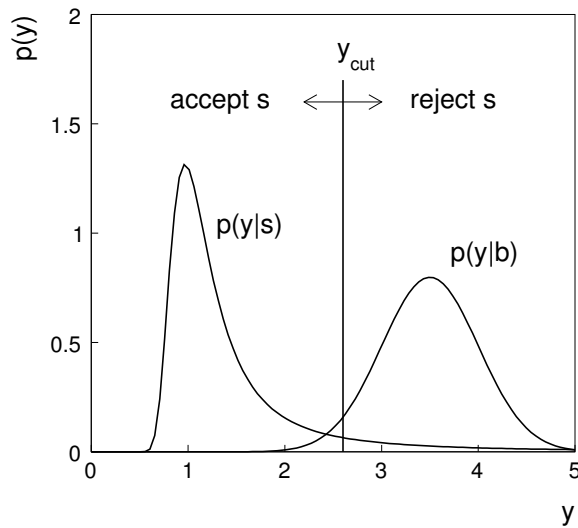


Figure 5.2: Distributions of the scalar test statistic $y(\mathbf{x})$ under the signal and background hypotheses. [120]

1882 Figure 5.2 illustrates what would be the probability distribution functions under
 1883 the signal and background hypotheses for a scalar test statistic with a cut on the
 1884 classifier y . Notice that the tails of the distributions indicate that some signal events
 1885 fall on the rejection region and some background events fall on the acceptance region;
 1886 therefore, it is convenient to define the *efficiency* with which events of a given type
 1887 are accepted, thus, the signal and background efficiencies are given by

$$\varepsilon_s = P(\text{accept event}|s) = \int_A f(\mathbf{x}|s) d\mathbf{x} = \int_{-\infty}^{y_{\text{cut}}} p(y|s) dy , \quad (5.1)$$

$$\varepsilon_b = P(\text{accept event}|b) = \int_A f(\mathbf{x}|b) d\mathbf{x} = \int_{-\infty}^{y_{\text{cut}}} p(y|b) dy , \quad (5.2)$$

1888 where A is the acceptance region. Under these conditions, the background hypothesis
 1889 corresponds to the *null hypothesis* (H_0), the signal hypothesis corresponds to the
 1890 *alternative hypothesis* (H_1), the background efficiency is the significance level of the
 1891 test, and signal efficiency is the power of the test; what is sought in an analysis is to
 1892 maximize the power of the test relative to the significance level.

1893 5.1.1 Decision trees

1894 For this thesis, the implementation of the MVA strategy, described above, is per-
 1895 formed through decision trees by using the TMVA software package [121] included in
 1896 the the ROOT analysis framework [123]. In a simple picture, a decision tree classifies
 1897 events according to their input variables values by setting a cut on each input variable
 1898 and checking which events are on which side of the cut, just as proposed in the MVA
 1899 strategy, but in addition, as a machine learning algorithm, decision trees offer the
 1900 possibility to be trained and then perform the classification efficiently.

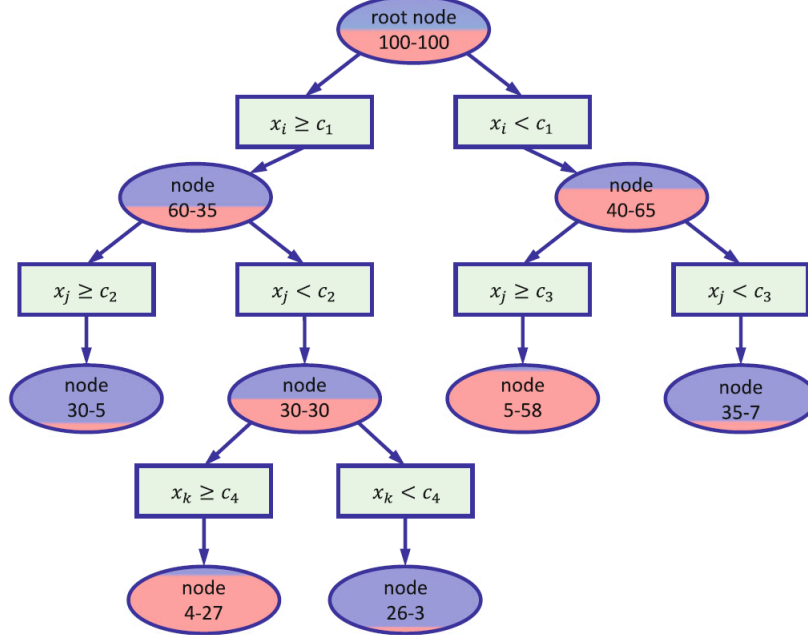


Figure 5.3: Example of a decision tree. Each node is fed with a MC sample mixing signal and background events (left-right numbers); nodes colors represent the relative amount of signal/background events [122].

1901 The training or growing of a decision tree is the process that defines the rules for
 1902 classifying events; this process is represented in figure5.3 and consist of several steps

1903 • take MC samples of signal and background events and split them into two parts
 1904 each; first parts form the training sample which will be used in the decision tree
 1905 training, while the second parts form the test sample which will be used for
 1906 testing the final classifier obtained from the training. Each event has associated
 1907 a set of input variables $\mathbf{x} = (x_1, \dots, x_n)$ which serve to distinguish between signal
 1908 and background events. The training sample is taken in at the root *node*.

1909 • pick one variable, say x_i
 1910 • pick one value of x_i , each event has its own value of x_i , and split the training
 1911 sample into two subsamples B_1 and B_2 ; B_1 contains events for which $x_i < c_1$

- 1912 while B_2 contains the rest of the training events;
- 1913 • scan all possible values of x_i and find the splitting value that provides the *best*
 1914 classification¹, i.e., B_1 is mostly made of signal events while B_2 is mostly made
 1915 of background events.
- 1916 • It is possible that variables other than the picked one produce a better classi-
 1917 fication, hence, all the variables have to be evaluated. Pick the next variable,
 1918 say x_j , and repeat the scan over its possible values.
- 1919 • At the end, all the variables and their values will have been scanned, the *best*
 1920 variable and splitting value will have been identified, say x_1, c_1 , and there will
 1921 be two nodes fed with the subsamples B_1 and B_2 .
- 1922 Nodes are further split by repeating the decision process until: a given number of
 1923 final nodes is obtained, nodes are largely dominated by either signal or background
 1924 events, or nodes has too few events to continue. Final nodes are called *leaves* and they
 1925 are classified as signal or background leaves according to the class of the majority of
 1926 events in them. Each *branch* in the tree corresponds to a sequence of cuts.
- 1927 The quality of the classification at each node is evaluated through a separation
 1928 criteria; there are several of them but the *Gini Index* (G) is the one used in the
 1929 decision trees trained for the analysis in this thesis. G is written in terms of the
 1930 purity (P), i.e. the fraction of signal events, of the samples after the separation is
 1931 made; it is given by

$$G = P(1 - P) \quad (5.3)$$

¹ Quality of the classification will be treated in the next paragraph.

1932 notice that $P=0.5$ at the root node while $G=0$ for pure leaves. For a node A split
 1933 into two nodes B_1 and B_2 the G gain is

$$\Delta G = G(A) - G(B_1) - G(B_2) \quad (5.4)$$

1934 the *best* classification corresponds to that for which the gain of G is maximized; hence,
 1935 the scanning over all event's variables and their values is of capital importance.

1936 In order to provide a numerical output for the classification, events in a sig-
 1937 nal(background) leaf are assigned an score of 1(-1) each, defining in this way the
 1938 decision tree *classifier or weak learner* as

$$f(\mathbf{x}) = \begin{cases} 1 & \mathbf{x} \text{ in signal region,} \\ -1 & \mathbf{x} \text{ in background region.} \end{cases}$$

1939 Figure 5.4 shows an example of the classification of a sample of events, containing
 1940 two variables, performed by a decision tree.

1941 5.1.2 Boosted decision trees (BDT).

1942 Event misclassification occurs when a training event ends up in the wrong leaf, i.e., a
 1943 signal event ends up in a background leaf or a background event ends up in a signal
 1944 leaf. A way to correct it is to assign a weight to the misclassified events and train
 1945 a second tree using the reweighted events; the event reweighting is performed by a
 1946 boosting algorithm, events with increased weight are known as *boosted* events, in such
 1947 a way that when used in the training of a new decision tree they get correctly classified.
 1948 The process is repeated iteratively adding a new tree to a forest and creating a set
 1949 of classifiers which are combined to create the next classifier; the final classifier offers

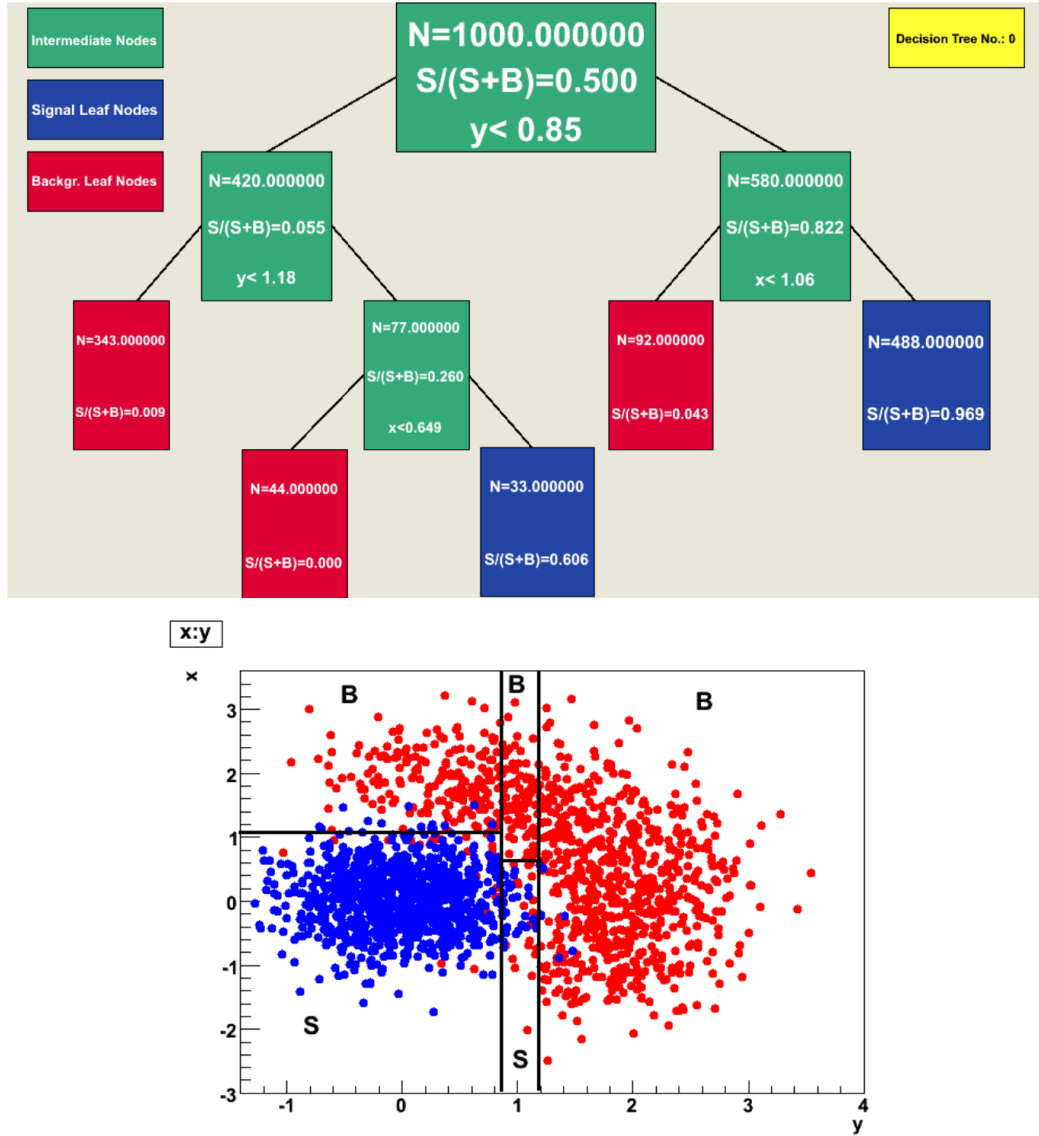


Figure 5.4: Example of a decision tree output. Each leaf, blue for signal events and red for background events, represent a region in the variables phase space [124].

1950 more stability² and has a smaller misclassification rate than any individual ones. The
 1951 resulting tree collection is known as a *boosted decision tree (BDT)*.
 1952 Thus, purity of the sample is generalized to

² Decision trees suffer from sensitivity to statistical fluctuations in the training sample which may leads to very different results with an small change in the training samples.

$$P = \frac{\sum_s w_s}{\sum_s w_s + \sum_b w_b} \quad (5.5)$$

1953 where w_s and w_b are the weights of the events; the Gini index is also generalized

$$G = \left(\sum_i^n w_i \right) P(1 - P) \quad (5.6)$$

1954 with n the number of events in the node. The final score of an event, after pass-
 1955 ing through the forest, is calculated as the renormalized sum of all the individual
 1956 (possibly weighted) scores; thus, high(low) score implies that the event is most likely
 1957 signal(background).

1958 The boosting procedure, implemented in the *Gradient boosting* algorithm used
 1959 in this thesis, produce a classifier $F(\mathbf{x})$ which is the weighted sum of the individual
 1960 classifiers obtained after each iteration,i.e.,

$$F(\mathbf{x}) = \sum_{m=1}^M \beta_m f(\mathbf{x}; a_m) \quad (5.7)$$

1961 where M is the number of trees in the forest. The *loss function* $L(F, y)$ represent the
 1962 deviation between the classifier $F(\mathbf{x})$ response and the true value y obtained from the
 1963 training sample (1 for signal events and -1 for background event), according to

$$L(F, y) = \ln(1 + e^{-2F(\mathbf{x})y}) \quad (5.8)$$

1964 thus, the reweighting is employed to ensure the minimization of the loss function;
 1965 a more detailed description of the minimization procedure can be found in reference
 1966 [125]. The final classifier output is later used as a final discrimination variable, labeled
 1967 as *BDT output/response*.

1968 **5.1.3 Overtraining.**

1969 Decision trees offer the possibility to have as many nodes as wished in order to
 1970 reduce the misclassification to zero (in theory); however, when a classifier is too much
 1971 adjusted to a particular training sample, the classifier response to a slightly different
 1972 sample may leads to a completely different classification results; this effect is know
 1973 as *overtraining*.

1974 An alternative to reduce the overtraining in BDTs consist in pruning the tree by
 1975 removing statistically insignificant nodes after the tree growing is completed but this
 1976 option is not available for BDTs with gradient boosting in the TMVA-toolkit, there-
 1977 fore, the overtraining has to be reduced by tuning the algorithm, number of nodes,
 1978 minimum number of events in the leaves, etc. The overtraining can be evaluated
 1979 by comparing the responses of the classifier when running over the training and test
 1980 samples.

1981 **5.1.4 Variable ranking.**

1982 BDTs have the couple of particular advantages related to the input variables; on one
 1983 side, they are relatively insensitive to the number of input variables used in the vector
 1984 \mathbf{x} . The ranking of the BDT input variables is determined by counting the number of
 1985 times a variable is used to split decision tree nodes; in addition, the separation gain-
 1986 squared achieved in the splitting and the number of events in the node are accounted
 1987 by applying a weighting to that number. Thus, those variables with small or no power
 1988 to separate signal and background events are rarely chosen to split the nodes,i.e., are
 1989 effectively ignored.

1990 On the other side, variables correlations play an important role for some MVA
 1991 methods like the Fisher discriminant algorithm in which the first step consist of

1992 performing a linear transformation to a phase space where the correlations between
 1993 variables are removed; in case of BDT algorithm, correlations do not affect the per-
 1994 formance.

1995 **5.1.5 BDT output example.**

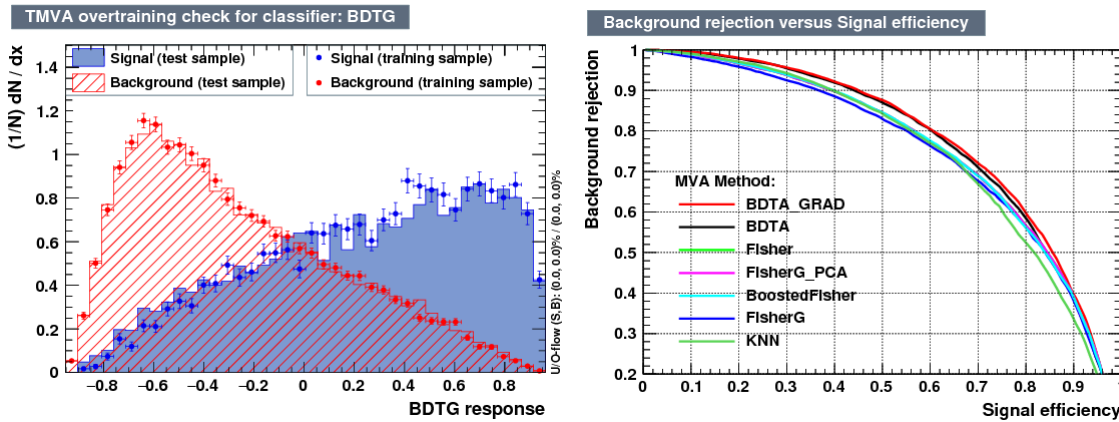


Figure 5.5: Left: Output distributions for the gradient boosted decision tree (BDTG) classifier using a sample of signal($pp \rightarrow tHq$) and background($pp \rightarrow t\bar{t}$) events. Right: Background rejection vs signal efficiency (ROC curves) for various MVA classifiers running over the same sample used to produce the plot on the left.

1996 Left side of figure 5.5 shows the BDT output distributions for signal($pp \rightarrow tHq$)
 1997 and background($pp \rightarrow t\bar{t}$) events; this plot is the equivalent to the one showed in
 1998 figure 5.2. A forest with 800 trees, maximum depth per tree = 3, and gradient
 1999 boosting have been used as training parameters. The BDTG classifier offers a good
 2000 separation power; while there is a small overtraining in the signal distribution, the
 2001 background distribution seems to be well predicted which might indicate that the
 2002 sample is composed of more background than signal events.

2003 Right side of figure 5.5 shows the background rejection vs signal efficiency curves
 2004 for several combinations of MVA classifiers-boosting algorithms; these curves are
 2005 known as ROC curves and give an indication of the performance of the classifier. The

2006 best performance is achieved with the BDTG classifier (BDTA_GRAD).

2007 5.2 Statistical inference.

2008 Once events are classified, the next step consists in finding the parameters that define
 2009 the likelihood functions $f(\mathbf{x}|s), f(\mathbf{x}|b)$ for signal and background events respectively.
 2010 In general, likelihood functions depend not only on the measurements but also on
 2011 parameters (θ_m) that define their shapes; the process of estimating these *unknown*
 2012 *parameters* and their uncertainties from the experimental data is called *inference*.
 2013 The likelihood function for N the events the in a sample is the combination of all the
 2014 likelihoods functions

$$L(\boldsymbol{\theta}) = \prod_{i=1}^N f(\mathbf{x}^i | \boldsymbol{\theta}) = \prod_{i=1}^N f(x_1^i, \dots, x_n^i; \theta_1, \dots, \theta_m) \quad (5.9)$$

2015 Thus, the estimation of the unknown parameters from experimental data samples
 2016 is written in terms of a central value using the notation

$$\theta = \hat{\theta} \pm \delta\theta \quad (5.10)$$

2017 where the interval $[\hat{\theta} + \delta\theta, \hat{\theta} - \delta\theta]$ is called *confidence interval*; it is usually inter-
 2018 preted, in the limit of infinite number of experiments, as the interval where the true
 2019 value of the unknown parameter θ is contained with a probability of 0.6827 (if no
 2020 other convention is stated).

2021 5.2.1 Nuisance parameters.

2022 The unknown parameter vector $\boldsymbol{\theta}$ is made of two types of parameters: on one side,
 2023 those parameters that provide information about the physical observables of interest

2024 for the experiment (*parameters of interest*); on the other side, the *nuisance parameters*
 2025 that are not of direct interest for the experiment but that needs to be included in
 2026 the analysis in order to achieve a satisfactory description of the data. They represent
 2027 effects of the detector response like the finite resolutions of the detection systems,
 2028 miscalibrations, and in general any source of uncertainty introduced in the analysis.

2029 In some cases the nuisance parameters are estimated using dedicated data samples,
 2030 for instance data from test beams for calibration purposes, when MC samples are
 2031 not suitable. The nuisance parameter uncertainties produce *systematic uncertainties*
 2032 while the uncertainties associated to fluctuations in data and related to the estimation
 2033 of the parameters of interest produce *statistical uncertainties*.

2034 5.2.2 Maximum likelihood estimation method

2035 The function that produce the estimate of a parameter is called *estimator*, there-
 2036 fore, estimators are usually constructed using mathematical procedures encoded in
 2037 algorithms. The estimation method used in this thesis is the *Maximum Likelihood*
 2038 *Estimation* method (MLE); it is based on the combined likelihood function defined
 2039 by eqn. 5.9 and the procedure seeks for the parameter set that corresponds to the
 2040 maximum value of the combined likelihood function, i.e., the *maximum likelihood*
 2041 *estimator* of the unknown parameter vector $\boldsymbol{\theta}$ is the function that produce the vec-
 2042 tor $\hat{\boldsymbol{\theta}}$ for which the likelihood function $L(\boldsymbol{\theta})$ evaluated at the measured sample \mathbf{x} is
 2043 maximum.

2044 Usually, the logarithm of the likelihood function is used in the numerical algo-
 2045 rithms implementations in order to avoid underflow the numerical precision of the
 2046 computers due to the product of low likelihoods. In addition, it is usual minimize the
 2047 negative logarithm of the likelihood function instead of maximizing the logarithm of

2048 it because in this way the procedure consist of differentiate a sum of therms and set
 2049 the sum to zero; therefore

$$F(\boldsymbol{\theta}) = -\ln L(\boldsymbol{\theta}) = -\sum_{i=1}^N f(\mathbf{x}^i | \boldsymbol{\theta}). \quad (5.11)$$

2050 The minimization process is performed by the software MINUIT [126] imple-
 2051 mented in the ROOT analysis framework. In case of large data samples the compu-
 2052 tational resources needed to calculate the likelihood function are too big; therefore,
 2053 the parameter estimation is performed using binned distributions of the variables of
 2054 interest for which the *binned likelihood function* is given by

$$L(data|\mu, \theta) = \prod_{i=1} \frac{(\mu s_i(\theta) + b_i(\theta))^{n_i}}{n_i!} e^{-\mu s_i(\theta) - b_i(\theta)}, \quad (5.12)$$

2055 with s_i and b_i the expected number of signal and background yields for bin i respec-
 2056 tively, n_i is the observed number of events in the bin i and $\mu = \sigma/\sigma_{SM}$ is the signal
 2057 strength. Notice that the number of entries per bin follows a Poisson distribution.
 2058 The analysis presented in this thesis is based on the binned distribution of the ratio
 2059 signal/background obtained from the BDT outputs.

2060 5.2.3 Hypothesis test

2061 The test statistic mentioned in section 5.1 involving
 2062 ; it is achieved, according to the Neyman-Pearson lemma [127],
 2063 by defining the acceptance region such that, for \mathbf{x} inside the region, the likelihood
 2064 ratio, i.e., the ratio of probability distribution functions for signal and background,

2065 **5.3 exclusion limits**

2066 **5.4 asymptotic limits**

2067 **Chapter 6**

2068 **Search for production of a Higgs**
2069 **boson and a single top quark in**
2070 **multilepton final states in pp**
2071 **collisions at $\sqrt{s} = 13$ TeV**

2072 **6.1 Introduction**

2073 The Higgs boson discovery, supported on experimental observations and theoretical
2074 predictions made about the SM, gives the clue of the way in that elementary particles
2075 acquire mass through the Higgs mechanism; therefore, knowing the Higgs mass, the
2076 Higgs-boson and Higgs-fermion couplings can be tested. In order to test the Higgs-top
2077 coupling, several measurements have been performed, as stated in the chapter 2, but
2078 they are limited to measure the square of the coupling; however, the production of a
2079 Higgs boson in association with a single top quark (tH) not only offers access to the
2080 sign of the coupling, but also, to the CP phase of the Higgs couplings.

2081 This chapter presents the search for the associated production of a Higgs boson
 2082 and a single top quark events, focusing on leptonic signatures provided by the Higgs
 2083 decay modes to WW , ZZ , and $\tau\tau$; the 13 TeV dataset produced in 2016, which
 2084 corresponds to an integrated luminosity of 35.9fb^{-1} , is used. Constraints on the sign
 2085 of the Higgs-top coupling (y_t) have been derived from the decay rate of Higgs boson
 2086 to photon pairs [45] and from the cross section for associated production of Higgs and
 2087 Z bosons via gluon fusion [128], with recent results disfavoring negative signs of the
 2088 coupling [56, 58, 129]. It expands previous analyses performed at 8 TeV [130, 131] and
 2089 searches for associated production of $t\bar{t}$ pair and a Higgs boson in the multilepton final
 2090 state channel [132]; it also complements searches in other decay channels targeting
 2091 $H \rightarrow b\bar{b}$ [133].

2092 As shown in section 2.5, the SM cross section of the associated production of a
 2093 Higgs boson and a single top quark (tHq) process is driven by a destructive interfer-
 2094 ence between two contributions (see Figure 2.14), where the Higgs couples to either
 2095 the W boson or the top quark; however, if the sign of the Higgs-top coupling is flipped
 2096 with respect to the SM prediction, a large enhancement of the cross section occurs,
 2097 making this analysis sensitive to such deviation. A second process, where the Higgs
 2098 boson and top quark are accompanied by a W boson (tHW) has similar behavior,
 2099 albeit with a weaker interference pattern and lower contribution to the tH cross sec-
 2100 tion, therefore, a combination of both processes would increase the sensitivity; in
 2101 this analysis both contributions are combined and referred as tH channel. A third
 2102 contribution comes from $t\bar{t}H$ process. The purpose of this analysis is to investigate
 2103 the exclusion of the presence of the $tH + t\bar{t}H$ processes under the assumption of the
 2104 anomalous Higgs-top coupling modifier ($\kappa_t = -1$). The analysis exploits signatures
 2105 with two leptons of the same sign (*2lss channel*) and three leptons (*3l channel*) in
 2106 the final state.

2107 The first sections present the characteristic tHq signature as well as the expected
 2108 backgrounds. The MC samples, data sets, and the physics object definitions are
 2109 then defined. Following, the background predictions, the signal extraction, and the
 2110 statistical treatment of the selected events as well as the systematic uncertainties are
 2111 described. The final section present the results for the exclusion limits as a function
 2112 of the ratio of κ_t and the dimensionless modifier of the Higgs-vector boson κ_V .

2113 **6.2 tHq signature**

2114 In order to select events of tHq process, its features are translated into a set of
 2115 selection rules; figure 6.1 shows the Feynman diagram and an schematic view of the
 2116 tHq process from the pp collision to the final state configuration. A single top quark
 2117 is produced accompanied by a light quark, denoted as q ; this light quark is produced
 2118 predominantly in the forward region of the detector. The Higgs boson which can
 2119 be either emitted by the exchanged W boson or directly by the singly produced top
 2120 quark.

2121 The top quark and Higgs boson decay after their production in the detector due to
 2122 their high masses/low lifetimes. The Higgs boson is required to decay into a W boson
 2123 pair¹. The top quark almost always decays into a bottom quark and a W boson, as
 2124 encoded in the CMK matrix. The W bosons are required to decay hadronically in
 2125 the 2lss channel case and leptonically in the 3l channel case, while τ leptons are not
 2126 reconstructed separately and only their leptonic decays into either electrons or muons
 2127 are considered in this analysis.

2128 In summary, the signal process is characterized by a the final state with

- 2129 • one light-flavored forward jet,

¹ ZZ and $\tau\tau$ decays are also include in the analysis but they are not separately reconstructed

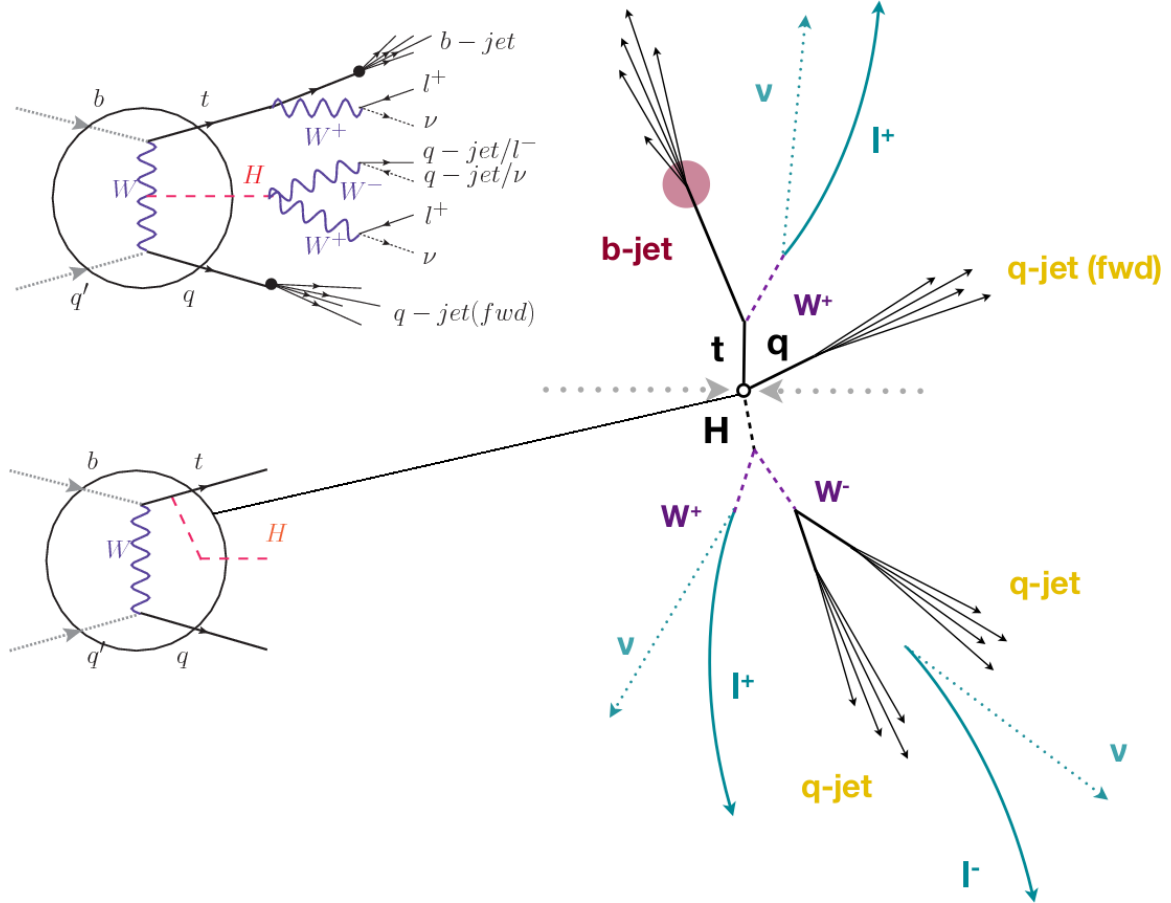


Figure 6.1: tHq event signature. Left: Feynman diagram including the whole evolution up to the final state for the case of the Higgs boson emitted by the W boson (top); Feynman diagram for the case where the Higgs boson is emitted by the top quark. Right: Schematic view as it would be seen in the detector; the circle in the Feynman diagrams on the left corresponds to the circle in the center of the schematic view as indicated by the line connecting them. In the 2lss channel, one of the W bosons from the Higgs boson decays to two light-quark jets while in the 3l channel both W bosons decays to leptons.

- 2130 • one central b-jet,
 - 2131 • 2lss channel \rightarrow two leptons of the same sign, two neutrinos and two light (often
2132 soft) jets,
 - 2133 • 3l channel \rightarrow three leptons, three neutrinos and no central light-flavored jets,
- 2134 The presence of neutrinos is inferred from the presence of MET. The analysis has

2135 been made public by CMS as a Physics Analysis Summary [134] combining the result
 2136 for the three lepton and two lepton same-sign channels. Currently, an effort to turn
 2137 the analysis into a paper is ongoing.

2138 **6.3 Background processes**

2139 The background processes are those that can mimic the signal signature or at least
 2140 can be reconstructed as that as a result of certain circumstances. The backgrounds
 2141 can be classified as

2142 • Irreducible backgrounds where genuine prompt leptons are produced in on-
 2143 shell W and Z boson decays; they can be reliably estimated directly from MC
 2144 simulated events, using higher-order cross sections or data control regions for
 2145 the overall normalization.

2146 • Reducible backgrounds where at least one of the leptons is *non-prompt*, i.e., pro-
 2147 duced within a hadronic jet, either a genuine lepton from heavy flavor decays.
 2148 misreconstructed jets, also known as *mis-ID leptons* or *fake leptons*, are consid-
 2149 ered non-prompt leptons as well. These non-prompt leptons leave tracks and
 2150 hits in the detection systems as would a prompt lepton, but correlating those
 2151 hits with nearby jets could be a way of removing them. Reducible backgrounds
 2152 are not well predicted by simulation, and are estimated using data-driven meth-
 2153 ods.

2154 The main sources of background events in the case of tHq process are $t\bar{t}$ process
 2155 and $t\bar{t} + X(X = W, Z, \gamma)$ processes, here represented together as $t\bar{t}V$ process. Figure
 2156 6.2 shows the signature for $t\bar{t}$ and $t\bar{t}W$ processes;

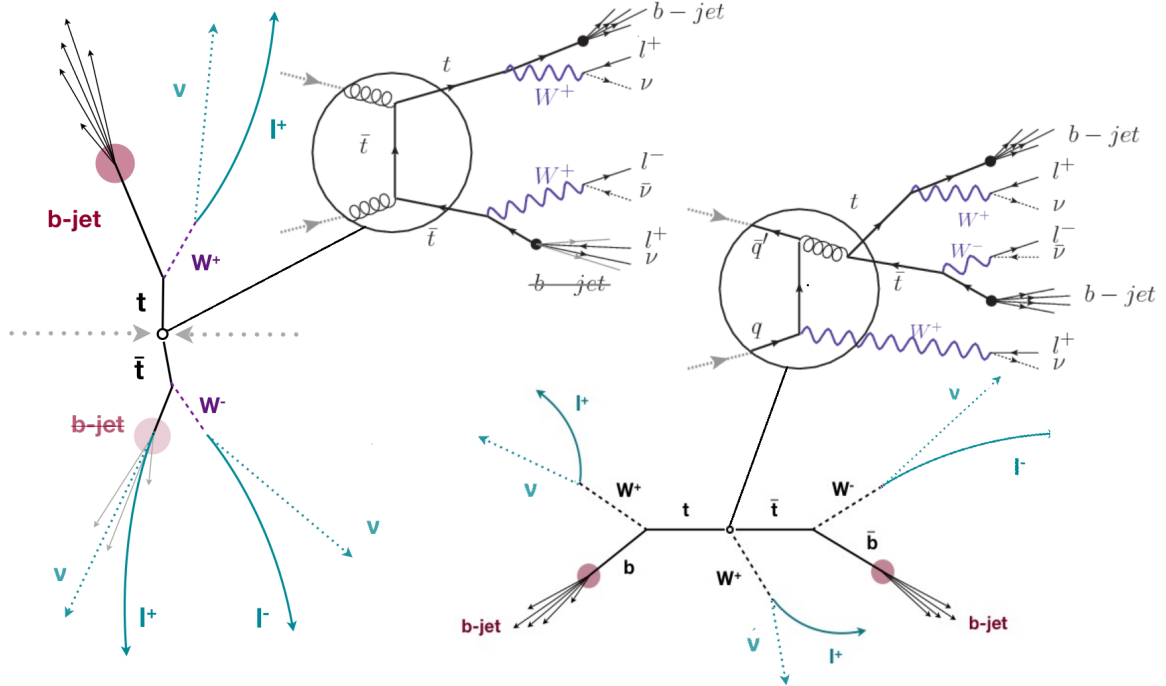


Figure 6.2: $t\bar{t}$ (left) and $t\bar{t}W$ (right) events signature as they would be seen in the detector; the Feynman diagrams including the whole evolution up to the final state are also showed. The $t\bar{t}$ process signature is very similar to that of the signal process with one fake lepton and non forward activity. The $t\bar{t}W$ process present a higher b-jet multiplicity compared to the signal process, a prompt lepton and no forward activity.

2157 The largest contribution to irreducible backgrounds involving prompt leptons
 2158 comes from $t\bar{t}W$, $t\bar{t}Z$, processes for which the number of ($b-$)jets (($b-$)jet multiplicity)
 2159 is higher than that of the signal events, while for other contributing background
 2160 events, WZ , ZZ , and rare SM processes like $W^\pm W^\pm qq$, $t\bar{t}t\bar{t}$, tZq , tZW , WWW ,
 2161 WWZ , WZZ , ZZZ , the ($b-$)jet multiplicity is lower compared to that of the signal
 2162 events. None of the irreducible backgrounds present activity in the forward region of
 2163 the detector.

2164 On the side of the reducible backgrounds, the largest contribution comes from the
 2165 $t\bar{t}$ events which have a very similar signature to the signal events but does no present
 2166 activity in the forward region of the detector either; A particular feature of the $t\bar{t}$
 2167 events is their charge-symmetry which is also a difference with the signal events.

2168 The charge misidentification plays an important role in the the 2lss channel since
 2169 leptons in processes like $t\bar{t}$ + jets or Z + jets can be charge misidentified, leading to
 2170 backgrounds increments. An identification variable have been designed in order to
 2171 reject this type of background events.

2172 6.4 Data and MC Samples

2173 Technical developments on the event generator side allow for an event-wise reweight-
 2174 ing that can change the event kinematics based on specific generation parameters.
 2175 This way not only the case of $C_t = \sqrt{2}$, but a whole range of κ_t and κ_V values can
 2176 be investigated.

2177 The data considered in this analysis were collected by the CMS experiment dur-
 2178 ing 2016 and correspond to a total integrated luminosity of $35.9 fb^{-1}$. Only periods
 2179 when the CMS magnet was on were considered when selecting the data samples, that
 2180 corresponds to the 23 Sep 2016 (Run B to G) and PromptReco (Run H) versions
 2181 of the datasets. The MC samples used in this analysis correspond to the RunI-
 2182 ISummer16MiniAODv2 campaign produced with CMSSW 80X. The two signal sam-
 2183 ples (for tHq and tHW) were produced with MG5_aMC@NLO (version 5.222), in
 2184 leading-order order mode, and are normalized to next-to-leading-order cross sections,
 2185 see Tab. 6.1. Each sample is generated with a set of event weights corresponding to
 2186 different values of κ_t and κ_V couplings as shown in Tab. 6.2.

2187 6.4.1 Full 2016 dataset and MC samples

2188 Different MC generators were used to generate the background processes. The dom-
 2189 inant sources ($t\bar{t}$, $t\bar{t}W$, $t\bar{t}Z$, $t\bar{t}H$) were produced using AMC@NLO interfaced to
 2190 PYTHIA8, and are scaled to NLO cross sections. Other processes are simulated us-

Sample	σ [pb]	BF
/THQ_Hincl_13TeV-madgraph-pythia8_TuneCUETP8M1/	0.7927	0.324
/THW_Hincl_13TeV-madgraph-pythia8_TuneCUETP8M1/	0.1472	1.0

Table 6.1: Signal samples and their cross section and branching fraction used in this analysis. See Ref. [143] for more details.

ing POWHEG interfaced to PYTHIA, or bare PYTHIA (see table 6.3 and [132] for more details).

6.4.2 Triggers

We consider online-reconstructed events triggered by one, two, or three leptons. Single-lepton triggers are included to boost the acceptance of events where the p_T of the sub-leading lepton falls below the threshold of the double-lepton triggers. Additionally, by including double-lepton triggers in the ≥ 3 lepton category, as well as single-lepton triggers in all categories, we increase the efficiency, considering the logical “or” of the trigger decisions of all the individual triggers in a given category. Tab. 6.5 shows the lowest-threshold non-prescaled triggers present in the High-Level Trigger (HLT) menus for both Monte-Carlo and data in 2016.

Trigger efficiency scale factors

The efficiency of events to pass the trigger is measured in simulation (trivially using generator information) and in the data (using event collected by an uncorrelated MET trigger). Small differences between the data and MC efficiencies are corrected by applying scale factors as shown in Tab. 6.6. The exact procedure and control plots are documented in [137] for the current analysis.

		<i>tHq</i>		<i>tHW</i>		
κ_V	κ_t	sum of weights	cross section [pb]	sum of weights	cross section [pb]	LHE weights
1.0	-3.0	35.700022	2.991	11.030445	0.6409	LHEweight_wgt[446]
1.0	-2.0	20.124298	1.706	5.967205	0.3458	LHEweight_wgt[447]
1.0	-1.5	14.043198	1.205	4.029093	0.2353	LHEweight_wgt[448]
1.0	-1.25	11.429338	0.9869	3.208415	0.1876	LHEweight_wgt[449]
1.0	-1.0		0.7927		0.1472	
1.0	-0.75	7.054998	0.6212	1.863811	0.1102	LHEweight_wgt[450]
1.0	-0.5	5.294518	0.4723	1.339886	0.07979	LHEweight_wgt[451]
1.0	-0.25	3.818499	0.3505	0.914880	0.05518	LHEweight_wgt[452]
1.0	0.0	2.627360	0.2482	0.588902	0.03881	LHEweight_wgt[453]
1.0	0.25	1.719841	0.1694	0.361621	0.02226	LHEweight_wgt[454]
1.0	0.5	1.097202	0.1133	0.233368	0.01444	LHEweight_wgt[455]
1.0	0.75	0.759024	0.08059	0.204034	0.01222	LHEweight_wgt[456]
1.0	1.0	0.705305	0.07096	0.273617	0.01561	LHEweight_wgt[457]
1.0	1.25	0.936047	0.0839	0.442119	0.02481	LHEweight_wgt[458]
1.0	1.5	1.451249	0.1199	0.709538	0.03935	LHEweight_wgt[459]
1.0	2.0	3.335034	0.2602	1.541132	0.08605	LHEweight_wgt[460]
1.0	3.0	10.516125	0.8210	4.391335	0.2465	LHEweight_wgt[461]
1.5	-3.0	45.281492	3.845	13.426212	0.7825	LHEweight_wgt[462]
1.5	-2.0	27.606715	2.371	7.809713	0.4574	LHEweight_wgt[463]
1.5	-1.5	20.476088	1.784	5.594971	0.3290	LHEweight_wgt[464]
1.5	-1.25	17.337465	1.518	4.635978	0.2749	LHEweight_wgt[465]
1.5	-1.0	14.483302	1.287	3.775902	0.2244	LHEweight_wgt[466]
1.5	-0.75	11.913599	1.067	3.014744	0.1799	LHEweight_wgt[467]
1.5	-0.5	9.628357	0.874	2.352505	0.1410	LHEweight_wgt[468]
1.5	-0.25	7.627574	0.702	1.789184	0.1081	LHEweight_wgt[469]
1.5	0.0	5.911882	0.5577	1.324946	0.08056	LHEweight_wgt[470]
1.5	0.25	4.479390	0.4365	0.959295	0.05893	LHEweight_wgt[471]
1.5	0.5	3.331988	0.3343	0.692727	0.04277	LHEweight_wgt[472]
1.5	0.75	2.469046	0.2558	0.525078	0.03263	LHEweight_wgt[473]
1.5	1.0	1.890565	0.2003	0.456347	0.02768	LHEweight_wgt[474]
1.5	1.25	1.596544	0.1689	0.486534	0.02864	LHEweight_wgt[475]
1.5	1.5	1.586983	0.1594	0.615638	0.03509	LHEweight_wgt[476]
1.5	2.0	2.421241	0.2105	1.170602	0.06515	LHEweight_wgt[477]
1.5	3.0	7.503280	0.5889	3.467546	0.1930	LHEweight_wgt[478]
0.5	-3.0	27.432685	2.260	8.929074	0.5136	LHEweight_wgt[479]
0.5	-2.0	13.956013	1.160	4.419093	0.2547	LHEweight_wgt[480]
0.5	-1.5	8.924438	0.7478	2.757611	0.1591	LHEweight_wgt[481]
0.5	-1.25	6.835341	0.5726	2.075247	0.1204	LHEweight_wgt[482]
0.5	-1.0	5.030704	0.4273	1.491801	0.08696	LHEweight_wgt[483]
0.5	-0.75	3.510528	0.2999	1.007273	0.05885	LHEweight_wgt[484]
0.5	-0.5	2.274811	0.1982	0.621663	0.03658	LHEweight_wgt[485]
0.5	-0.25	1.323555	0.1189	0.334972	0.01996	LHEweight_wgt[486]
0.5	0.0	0.656969	0.06223	0.147253	0.008986	LHEweight_wgt[487]
0.5	0.25	0.274423	0.02830	0.058342	0.003608	LHEweight_wgt[488]
0.5	0.5	0.176548	0.01778	0.068404	0.003902	LHEweight_wgt[489]
0.5	0.75	0.363132	0.03008	0.177385	0.009854	LHEweight_wgt[490]
0.5	1.0	0.834177	0.06550	0.385283	0.02145	LHEweight_wgt[491]
0.5	1.25	1.589682	0.1241	0.692099	0.03848	LHEweight_wgt[492]
0.5	1.5	2.629647	0.2047	1.097834	0.06136	LHEweight_wgt[493]
0.5	2.0	5.562958	0.4358	2.206057	0.1246	LHEweight_wgt[494]
0.5	3.0	14.843102	1.177	5.609519	0.3172	LHEweight_wgt[495]

Table 6.2: κ_V and κ_t combinations generated for the two signal samples and their NLO cross sections. The *tHq* cross section is multiplied by the branching fraction of the enforced leptonic decay of the top quark (0.324). See also Ref. [143].

Sample	σ [pb]
TTWJetsToLNu_TuneCUETP8M1_13TeV-amcatnloFXFX-madspin-pythia8	0.2043
TTZToLLNuNu_M-10_TuneCUETP8M1_13TeV-amcatnlo-pythia8	0.2529
ttHJetToNonbb_M125_13TeV_amcatnloFXFX_madspin_pythia8_mWCutfix /store/cmst3/group/susy/gpetrucc/13TeV/u/TTLL_m1to10_LO_NoMS_for76X/	0.2151 0.0283
WGToLNuG_TuneCUETP8M1_13TeV-madgraphMLM-pythia8	585.8
ZGTo2LG_TuneCUETP8M1_13TeV-amcatnloFXFX-pythia8	131.3
TGJets_TuneCUETP8M1_13TeV_amcatnlo_madspin_pythia8	2.967
TGJets_TuneCUETP8M1_13TeV_amcatnlo_madspin_pythia8	2.967
TTGJets_TuneCUETP8M1_13TeV-amcatnloFXFX-madspin-pythia8	3.697
WpWpJJ_EWK-QCD_TuneCUETP8M1_13TeV-madgraph-pythia8	0.03711
ZZZ_TuneCUETP8M1_13TeV-amcatnlo-pythia8	0.01398
WWZ_TuneCUETP8M1_13TeV-amcatnlo-pythia8	0.1651
WZZ_TuneCUETP8M1_13TeV-amcatnlo-pythia8	0.05565
WW_DoubleScattering_13TeV-pythia8	1.64
tZq_ll_4f_13TeV-amcatnlo-pythia8_TuneCUETP8M1	0.0758
ST_tWll_5f_LO_13TeV-MadGraph-pythia8	0.01123
TTTT_TuneCUETP8M1_13TeV-amcatnlo-pythia8	0.009103
WZTo3LNu_TuneCUETP8M1_13TeV-powheg-pythia8	4.4296
ZZTo4L_13TeV_powheg_pythia8	1.256
TTJets_SingleLeptFromTbar_TuneCUETP8M1_13TeV-madgraphMLM-pythia8	182.1754
TTJets_SingleLeptFromT_TuneCUETP8M1_13TeV-madgraphMLM-pythia8	182.1754
TTJets_DiLept_TuneCUETP8M1_13TeV-madgraphMLM-pythia8	87.3
DYJetsToLL_M-10to50_TuneCUETP8M1_13TeV-amcatnloFXFX-pythia8	18610
DYJetsToLL_M-50_TuneCUETP8M1_13TeV-madgraphMLM-pythia8	6024
WJetsToLNu_TuneCUETP8M1_13TeV-amcatnloFXFX-pythia8	61526.7
ST_tW_top_5f_inclusiveDecays_13TeV-powheg-pythia8_TuneCUETP8M1	35.6
ST_tW_antitop_5f_inclusiveDecays_13TeV-powheg-pythia8_TuneCUETP8M1	35.6
ST_t-channel_4f_leptonDecays_13TeV-amcatnlo-pythia8_TuneCUETP8M1	70.3144
ST_t-channel_antitop_4f_leptonDecays_13TeV-powheg-pythia8_TuneCUETP8M1	26.2278
ST_s-channel_4f_leptonDecays_13TeV-amcatnlo-pythia8_TuneCUETP8M1	3.68064
WWTo2L2Nu_13TeV-powheg	10.481

Table 6.3: List of background samples used in this analysis (CMSSW 80X). In the first section of the table are listed the samples of the processes for which we use the simulation to extract the final yields and shapes, in the second section the samples of the processes we will estimate from data. The MC simulation is used to design the data driven methods and derive the associated systematics.

Sample	σ [pb]
ttWJets_13TeV_madgraphMLM	0.6105
ttZJets_13TeV_madgraphMLM	0.5297/0.692

Table 6.4: Leading-order $t\bar{t}W$ and $t\bar{t}Z$ samples used in the signal BDT training.

Same-sign dilepton (==2 muons)
HLT_Mu17_TrkIsoVVL_Mu8_TrkIsoVVL_DZ_v*
HLT_Mu17_TrkIsoVVL_TkMu8_TrkIsoVVL_DZ_v*
HLT_IsoMu22_v*
HLT_IsoTkMu22_v*
HLT_IsoMu22_eta2p1_v*
HLT_IsoTkMu22_eta2p1_v*
HLT_IsoMu24_v*
HLT_IsoTkMu24_v*
Same-sign dilepton (==2 electrons)
HLT_Ele23_Ele12_CaloIdL_TrackIdL_IsoVL_DZ_v*
HLT_Ele27_eta2p1_WP Loose_Gsf_v*
HLT_Ele27_WPTight_Gsf_v*
HLT_Ele25_eta2p1_WPTight_Gsf_v*
Same-sign dilepton (==1 muon, ==1 electron)
HLT_Mu23_TrkIsoVVL_Ele8_CaloIdL_TrackIdL_IsoVL_v*
HLT_Mu8_TrkIsoVVL_Ele23_CaloIdL_TrackIdL_IsoVL_v*
HLT_Mu23_TrkIsoVVL_Ele8_CaloIdL_TrackIdL_IsoVL_DZ_v*
HLT_Mu8_TrkIsoVVL_Ele23_CaloIdL_TrackIdL_IsoVL_DZ_v*
HLT_IsoMu22_v*
HLT_IsoTkMu22_v*
HLT_IsoMu22_eta2p1_v*
HLT_IsoTkMu22_eta2p1_v*
HLT_IsoMu24_v*
HLT_IsoTkMu24_v*
HLT_Ele27_WPTight_Gsf_v*
HLT_Ele25_eta2p1_WPTight_Gsf_v*
HLT_Ele27_eta2p1_WP Loose_Gsf_v*
Three lepton and Four lepton
HLT_DiMu9_Ele9_CaloIdL_TrackIdL_v*
HLT_Mu8_DiEle12_CaloIdL_TrackIdL_v*
HLT_TripleMu_12_10_5_v*
HLT_Ele16_Ele12_Ele8_CaloIdL_TrackIdL_v*
HLT_Mu23_TrkIsoVVL_Ele8_CaloIdL_TrackIdL_IsoVL_v*
HLT_Mu23_TrkIsoVVL_Ele8_CaloIdL_TrackIdL_IsoVL_DZ_v*
HLT_Mu8_TrkIsoVVL_Ele23_CaloIdL_TrackIdL_IsoVL_v*
HLT_Mu8_TrkIsoVVL_Ele23_CaloIdL_TrackIdL_IsoVL_DZ_v*
HLT_Ele23_Ele12_CaloIdL_TrackIdL_IsoVL_DZ_v*
HLT_Mu17_TrkIsoVVL_Mu8_TrkIsoVVL_DZ_v*
HLT_Mu17_TrkIsoVVL_TkMu8_TrkIsoVVL_DZ_v*
HLT_IsoMu22_v*
HLT_IsoTkMu22_v*
HLT_IsoMu22_eta2p1_v*
HLT_IsoTkMu22_eta2p1_v*
HLT_IsoMu24_v*
HLT_IsoTkMu24_v*
HLT_Ele27_WPTight_Gsf_v*
HLT_Ele25_eta2p1_WPTight_Gsf_v*
HLT_Ele27_eta2p1_WP Loose_Gsf_v*

Table 6.5: Table of high-level triggers that we consider in the analysis.

Category	Scale Factor
ee	1.01 ± 0.02
e μ	1.01 ± 0.01
$\mu\mu$	1.00 ± 0.01
3l	1.00 ± 0.03

Table 6.6: Trigger efficiency scale factors and associated uncertainties, shown here rounded to the nearest percent.

2208 6.5 Object Identification

2209 In this section, the specific definitions of the physical objects in terms of the numerical
 2210 values assigned to the reconstruction parameters are presented; thus, the provided
 2211 details summarize and complement the descriptions presented in previous chapters.
 2212 The object reconstruction and selection strategy used in this thesis is inherited from
 2213 the analyses in references [132, 137], thus, the information provided in this section is
 2214 extracted from those documents unless other references are stated.

2215 6.5.1 Jets and b -jet tagging.

2216 In this analysis, jets are reconstructed by clustering PF candidates using the anti- k_t
 2217 algorithm with parameter distance $\Delta R = 0.4$; those charged hadrons that are not
 2218 consistent with the selected primary vertex are discarded from the clustering. The
 2219 jet energy is then corrected for the varying response of the detector as a function
 2220 of transverse momentum p_T and pseudorapidity η . Jets are selected for use in the
 2221 analysis only if they have $p_T > 25$ GeV and are separated from any selected leptons
 2222 by $\Delta R > 0.4$.

2223 Jets coming from the primary vertex and jets coming from pile-up vertices are
 2224 distinguished using a MVA discriminator based on the differences in the jet shapes,
 2225 in the relative multiplicity of charged and neutral components, and in the different
 2226 fraction of transverse momentum which is carried by the hardest components. Jet

2227 tracks are also required to be compatible with the primary vertex.

2228 Jets originated from the hadronization of a b quark are selected using a MVA
 2229 likelihood discriminant which uses track-based lifetime information and reconstructed
 2230 secondary vertices (CSV algorithm). Only jets within the CMS tracker acceptance
 2231 ($\eta < 2.4$) are identified with this tool. Data samples are used to measure the efficiency
 2232 of the b -jet tagging and the probability to misidentify jets from light quarks or gluons;
 2233 in both cases the measurements are parametrized as a function of the jet p_T and η
 2234 and later used to correct differences between the data and MC simulation in the b
 2235 tagging performance, by applying per-jet weights to the simulation, dependent on
 2236 the jet p_T , η , b tagging discriminator, and flavor (from simulation truth) [135]. The
 2237 per-event weight is taken as the product of the per-jet weights, including those of the
 2238 jets associated to the leptons. The weights are derived on $t\bar{t}$ and Z+jets events.

2239 Two working points are defined, based on the CSV algorithm output: *loose*' work-
 2240 ing point (CSV>0.46) with a b signal tagging efficiency of about 83% and a mistagging
 2241 rate of about 8%; and *medium* working point (CSV>0.80) with b -tagging efficiency of
 2242 about 69% and mistagging rate of order 1% [136]. Tagging of jets from charm quarks
 2243 have efficiencies of about 40% and 18% for loose and medium working points re-
 2244 spectively. Separate scale factors are applied to jets originating from bottom/charm
 2245 quarks and from light quarks in simulated events to match the tagging efficiencies
 2246 measured in the data.

2247 6.5.2 Missing Energy MET.

2248 As stated in section 4.4.1.1, the MET vector is calculated as the negative of the vector
 2249 sum of transverse momenta of all PF candidates in the event and its magnitude is
 2250 referred to as E_T^{miss} . Due to pile-up interactions, the performance in determining

2251 MET is degraded; in order to correct for that, the energy from the selected jets and
 2252 leptons that compose the event is assigned to the variable H_T^{miss} . It is calculated in
 2253 the same way as E_T^{miss} and although it has worse resolution than E_T^{miss} , it is more
 2254 robust in the sense that it does not rely on the soft part of the event. The event
 2255 selection uses a linear discriminator based on the two variables given by

$$E_T^{miss} LD = 0.00397 * E_T^{miss} + 0.00265 * H_T^{miss} \quad (6.1)$$

2256 taking advantage of the fact that the correlation between E_T^{miss} and H_T^{miss} is less
 2257 for events with instrumental missing energy than for events with real missing energy.
 2258 The working point $E_T^{miss} LD > 0.2$ was chosen to ensure a good signal efficiency while
 2259 keeping a good background rejection.

2260 6.5.3 Lepton reconstruction and identification

2261 Two types of leptons are defined in this analysis: *signal leptons* are those coming from
 2262 W, Z and τ decays which usually are isolated from other particles; *background leptons*
 2263 are defined as leptons produced in b -jet hadron decays, light-jets misidentification,
 2264 and photon conversions.

2265 The process of reconstruction and identification of electron and muon candidates
 2266 was described in chapter4, hence, the identification variables used in order to retain
 2267 the highest possible efficiency for signal leptons while maximizing the rejection of
 2268 background leptons are listed and described in the following sections ².

2269 The identification variables include not only observables related directly to the re-
 2270 constructed leptons themselves, but also to the clustered energy deposits and charged
 2271 particles in a cone around the lepton direction (jet-related variables); an initial loose

² the studies performed to optimize the identification are far from the scope of this thesis, therefore, only general descriptions are provided

2272 preselection of leptons candidates is performed and then an MVA discriminator, re-
 2273 ferred to as *lepton MVA* discriminator, is used to distinguish signal leptons from
 2274 background leptons.

2275 **Muons.**

2276 The Physics Objects Groups (POG) at CMS, are in charge of studying and defining
 2277 the set of selection criteria applied on the course of reconstruction and identification
 2278 of particles. These selection criteria are implemented in the CMS framework in the
 2279 form of several object identification working points according to the strength of the
 2280 requirements.

2281 The muon candidates are reconstructed by combining information from the tracker
 2282 system and the muon detection system of CMS detector and the POG defined three
 2283 working points for muon identification *MuonID* [138];

- 2284 • *POG Loose Muon ID* is a particle identified as a muon by the PF event re-
 2285 construction and also reconstructed either as a global-muon or as an arbitrated
 2286 tracker-muon. This identification criteria is designed to be highly efficient for
 2287 prompt muons and for muons from heavy and light quark decays; it can be com-
 2288 plemented by applying impact parameter cuts in analyses with prompt muon
 2289 signals.
- 2290 • *POG Medium Muon ID* is a Loose muon with additional track-quality and
 2291 muon-quality (spatial matching between the individual measurements in the
 2292 tracker and the muon system) requirements. This identification criteria is de-
 2293 signed to be highly efficient in the separation of the muons coming from decay
 2294 in flight of heavy quarks and muons coming from B meson decays as well as
 2295 prompt muons. An additional category *MVA Prompt ID* is defined in this iden-

2296 tification criteria directed to discriminated muons from B mesons and prompt
 2297 muons (from W,Z and τ decays). The Medium ID provides the same fake rate as
 2298 the Tight Muon ID but a higher efficiency on prompt and B-decays muons. [139]

- 2299 • *POG Tight Muon ID* is a global muon with additional muon-quality require-
 2300 ments Tight Muon ID selects a subset of the PF muons.

2301 Only muons within the muon system acceptance $|\eta| < 2.4$ and minimum p_T of 5
 2302 GeV are considered.

2303 **Electrons.**

2304 Electrons are reconstructed using information from the tracker and from the electro-
 2305 magnetic calorimeter and identified by an MVA algorithm (*MVA eID* discriminant)
 2306 using the shape of the calorimetric shower variables like the shape in η and ϕ , the clus-
 2307 ter circularity, widths along η and ϕ ; track-cluster matching variables like E_{tot}/p_{in} ,
 2308 E_{Ele}/p_{out} , $\Delta\eta_{in}$, $\Delta\eta_{out}$, $\Delta\phi_{in}$, $1/E - 1/p$; and track quality variables like ξ^2 of the
 2309 GSF tracks, the number of hits used by the GSF filter [140].

2310 A loose selection based on η -dependent cuts on this discriminant is used to prese-
 2311 lect electron candidates, the full shape of the discriminant is used in the lepton MVA
 2312 selection to separate signal leptons from background leptons (described in section
 2313 6.5.3).

2314 In order to reject electrons from photon conversions, electron candidates with
 2315 missing hits in the pixel tracker layers or matched to a conversion secondary vertex
 2316 are discarded. Electrons are selected for the analysis if they have $p_T > 7$ GeV and
 2317 are located within the tracker system acceptance region ($|\eta| < 2.5$).

2318 **Lepton vertexing and pile-up rejection.**

2319 The impact parameter in the transverse plane d_0 , impact parameter along the z
 2320 axis d_z , and the impact parameter significance in the detector space SIP_{3D} , are
 2321 considered to perform the identification and rejection of pile-up, misreconstructed
 2322 tracks, and background leptons from b-hadron decays; pile-up and misreconstructed
 2323 track mitigation is achieved by imposing loose cuts on the impact parameter variables.
 2324 The full shape of the those variables is used in a lepton MVA classifier to achieve the
 2325 best separation between the signal and the background leptons.

2326 **Lepton isolation.**

2327 PF is able to recognize leptons from two different sources: on one side, leptons from
 2328 the decays of heavy particles, such as W and Z bosons, which are normally isolated
 2329 in space from the hadronic activity in the event; on the other side, leptons from the
 2330 decays of hadrons and jets misidentified as leptons, which are not isolated as the
 2331 former. For highly boosted systems, like the lepton and the b -jet generated in the
 2332 semileptonic decay of a boosted top, the decay products tend to be more closer and
 2333 sometimes they even overlap; thus, the PF standard definition of isolation in terms of
 2334 the separation between the lepton candidates and other PF objects in the η - ϕ plane,

$$\Delta R = \sqrt{(\eta^l - \eta^i)^2 + (\phi^l - \phi^i)^2} < 0.3 \quad (6.2)$$

2335 which considers all the neutral, charged hadrons and photons in a cone around the
 2336 leptons, is refocused to the local isolation of the leptons through the mini-isolation
 2337 I_{mini} [141] defined as the sum of particle flow candidates p_T within a cone around

2338 the lepton, corrected for the effects of pileup and divided by the lepton p_T

$$I_{mini} = \frac{\sum_R p_T(h^\pm) - \max \left(0, \sum_R p_T(h^0) + p_T(\gamma) - \rho \mathcal{A} \left(\frac{R}{0.3} \right)^2 \right)}{p_T(l)} \quad (6.3)$$

2339 where ρ is the pileup energy density, h^\pm, h^0, γ, l , represent the charged hadron, neutral
 2340 hadrons, photons, and the lepton, respectively. The radius R of the cone depends on
 2341 the p_T of the lepton according to

$$R = \frac{10\text{GeV}}{\min(\max(p_T(l), 50\text{GeV}), 200\text{GeV})}, \quad (6.4)$$

2342 The p_T dependence of the cone size allows for greater signal efficiency. Setting a
 2343 cut on I_{mini} below a given threshold ensures that the lepton is locally isolated, even
 2344 in boosted systems. The effect of pileup is mitigated using the so-called effective area
 2345 correction \mathcal{A} listed in Table 6.7.

$ \eta $ range	$\mathcal{A}(e)$ neutral/charged	$\mathcal{A}(\mu)$ neutral/charged
0.0 - 0.8	0.1607 / 0.0188	0.1322 / 0.0191
0.8 - 1.3	0.1579 / 0.0188	0.1137 / 0.0170
1.3 - 2.0	0.1120 / 0.0135	0.0883 / 0.0146
2.0 - 2.2	0.1228 / 0.0135	0.0865 / 0.0111
2.2 - 2.5	0.2156 / 0.0105	0.1214 / 0.0091

Table 6.7: Effective areas, for electrons and muons used to mitigate the effect of pileup by using the so-called effective area correction.

2346 A loose cut on I_{mini} is applied to pre-select the muon and electron candidates;
 2347 however, the full shape is used in the lepton MVA discriminator when performing the
 2348 signal lepton selection.

2349 **Jet-related variables.**

2350 In order to reject misidentified leptons from b -jets, mostly coming from $t\bar{t}$ +jets,
 2351 Drell-Yan+jets, and W+jets events, the vertexing and isolation described in previous
 2352 sections are complemented with additional variables related to the closest recon-
 2353 structed jet to the lepton, i.e., the PF jets reconstructed³ around the leptons with
 2354 $\Delta R = \sqrt{(\eta^l - \eta^{jet})^2 + (\phi^l - \phi^{jet})^2} < 0.5$. The identification variables used in the lep-
 2355 ton MVA discriminator are the ratio p_T^l/p_T^{jet} , the CSV b-tagging discriminator value
 2356 of the jet, the number of charged tracks of the jet, and the relative p_T given by

$$p_T^{rel} = \frac{(\vec{p}_{jet} - \vec{p}_l) \cdot \vec{p}_l}{\|\vec{p}_{jet} - \vec{p}_l\|}. \quad (6.5)$$

2357 **LeptonMVA discriminator.**

2358 Electrons and muons passing the basic selection process described above are referred
 2359 to as *loose leptons*. Additional discrimination between signal leptons and background
 2360 leptons is crucial considering that the rate of $t\bar{t}$ production is much larger than the
 2361 signal, hence, an overwhelming background from $t\bar{t}$ production. To maximally ex-
 2362 ploit the available information in each event to that end, the dedicated lepton MVA
 2363 discriminator, based on a boosted decision tree (BDT) algorithm, has been built so
 2364 that all the identification variables can be used together.

2365 The lepton MVA discriminator training is performed using simulated signal Loose
 2366 leptons from the $t\bar{t}H$ MC sample and fake leptons from the $t\bar{t}$ +jets MC sample,
 2367 separately for muons and electrons. The input variables used include vertexing, iso-
 2368 lation and jet-related variables, the p_T and η of the lepton, the electron MVA eID
 2369 discriminator and the muon segment-compatibility variables. An additional require-
 2370 ment known as *tight-charge* requirement, is imposed by comparing two independent

³ charged hadrons from PU vertices are not removed prior to the jet clustering.

measurement of the charge, one from the ECAL supercluster and the other from the tracker; thus, the consistency in the measurements of the electron charge is ensured so that events with a wrong electron charge assignment are rejected; this variable is particularly used in the 2lss channel to suppress opposite-sign events for which the charge of one of the leptons has been mismeasured. The tight-charge requirement for muons is represented by the requirement of a consistently well measured track transverse momentum given by $\Delta p_T/p_T < 0.2$. Leptons are selected for the final analysis if they pass a given threshold of the BDT output, and are referred to as *tight leptons* in the following.

The validation of the lepton MVA algorithm and the lepton identification variables is performed using data in various control regions; the details about that validation are not discussed here but can be found in Reference [137].

Selection definitions

Electron and muon object identification is defined in three different sets of selections criteria; the *Loose*, *Fakeable Object*, and *Tight* selection. These three levels of selection are designed to serve for event level vetoes, the fake rate estimation application region, and the final signal selection, respectively. The p_T of fakeable objects is defined as $0.85 \times p_T(\text{jet})$, where the jet is the one associated to the lepton object. This mitigates the dependence of the fake rate on the momentum of the fakeable object and thereby improves the precision of the method.

Tables 6.8 and 6.9 list the full criteria for the different selections of muons and electrons.

In addition to the previously defined requirements for jets, they are required to be separated from any lepton candidates passing the fakeable object selections by $\Delta R > 0.4$.

Cut	Loose	Fakeable object	Tight
$ \eta < 2.4$	✓	✓	✓
p_T	$> 5\text{GeV}$	$> 15\text{GeV}$	$> 15\text{GeV}$
$ d_{xy} < 0.05 \text{ (cm)}$	✓	✓	✓
$ d_z < 0.1 \text{ (cm)}$	✓	✓	✓
$\text{SIP}_{3D} < 8$	✓	✓	✓
$I_{\text{mini}} < 0.4$	✓	✓	✓
is Loose Muon	✓	✓	✓
jet CSV	—	< 0.8484	< 0.8484
is Medium Muon	—	—	✓
tight-charge	—	—	✓
lepMVA > 0.90	—	—	✓

Table 6.8: Requirements on each of the three muon selections. In the cases where the cut values change between the selections, those values are listed in the table. Otherwise, whether the cut is applied is indicated.

Cut	Loose	Fakeable Object	Tight
$ \eta < 2.5$	✓	✓	✓
p_T	$> 7\text{GeV}$	$> 15\text{GeV}$	$> 15\text{GeV}$
$ d_{xy} < 0.05 \text{ (cm)}$	✓	✓	✓
$ d_z < 0.1 \text{ (cm)}$	✓	✓	✓
$\text{SIP}_{3D} < 8$	✓	✓	✓
$I_{\text{mini}} < 0.4$	✓	✓	✓
MVA eID $> (0.0, 0.0, 0.7)$	✓	✓	✓
$\sigma_{in\eta} < (0.011, 0.011, 0.030)$	—	✓	✓
H/E $< (0.10, 0.10, 0.07)$	—	✓	✓
$\Delta\eta_{in} < (0.01, 0.01, 0.008)$	—	✓	✓
$\Delta\phi_{in} < (0.04, 0.04, 0.07)$	—	✓	✓
$-0.05 < 1/E - 1/p < (0.010, 0.010, 0.005)$	—	✓	✓
p_T^{ratio}	—	$> 0.5^\dagger / -$	—
jet CSV	—	$< 0.3^\dagger / < 0.8484$	< 0.8484
tight-charge	—	—	✓
conversion rejection	—	—	✓
Number of missing hits	< 2	$= 0$	$= 0$
lepton MVA > 0.90	—	—	✓

Table 6.9: Criteria for each of the three electron selections. In cases where the cut values change between selections, those values are listed in the table. Otherwise, whether the cut is applied is indicated. In some cases, the cut values change for different η ranges. These ranges are $0 < |\eta| < 0.8$, $0.8 < |\eta| < 1.479$, and $1.479 < |\eta| < 2.5$ and the respective cut values are given in the form (value₁, value₂, value₃). For the two p_T^{ratio} and CSV rows, the cuts marked with a \dagger are applied to leptons that fail the lepton MVA cut, while the loose cut value is applied to those that pass the lepton MVA cut.

2396 6.5.4 Lepton selection efficiency

2397 Efficiencies of reconstruction and selecting loose leptons are measured both for muons
 2398 and electrons using a tag and probe method on both data and MC, using $Z \rightarrow \ell^+ \ell^-$
 2399 [142]. The scale factors are derived from the ratio of efficiencies $\varepsilon_i(p_T, \eta)$ measured
 2400 for a given lepton in data/MC, according to

$$\rho(p_T, \eta) = \frac{\varepsilon_{\text{data}}(p_T, \eta)}{\varepsilon_{\text{MC}}(p_T, \eta)}. \quad (6.6)$$

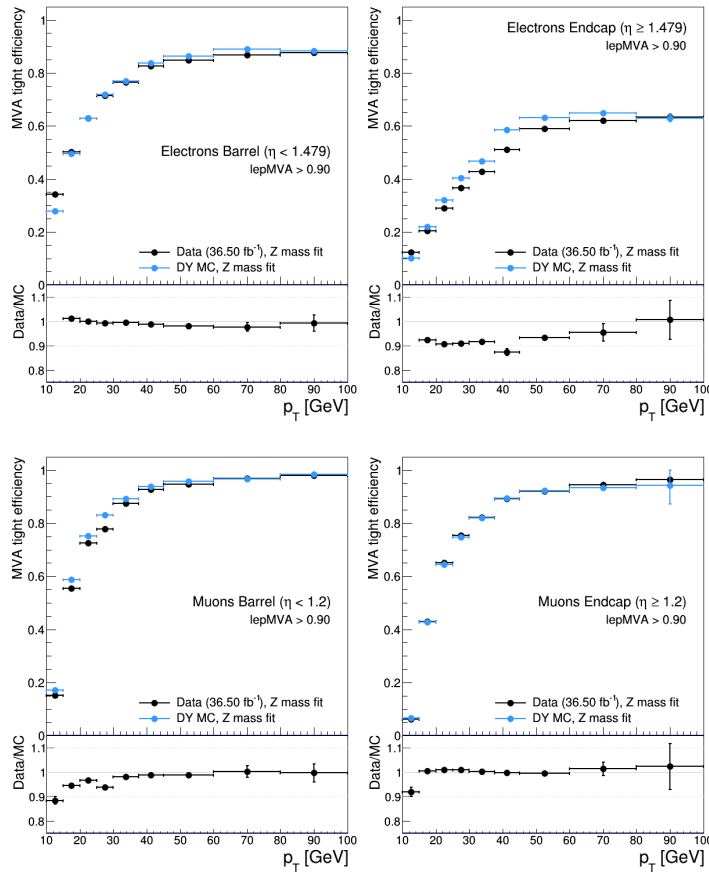


Figure 6.3: Tight vs loose selection efficiencies for electrons (top), and muons (bottom), for the 2lss definition, i.e., including the tight-charge requirement.

2401 The scale factor for each event is used to correct the weight of the event in the

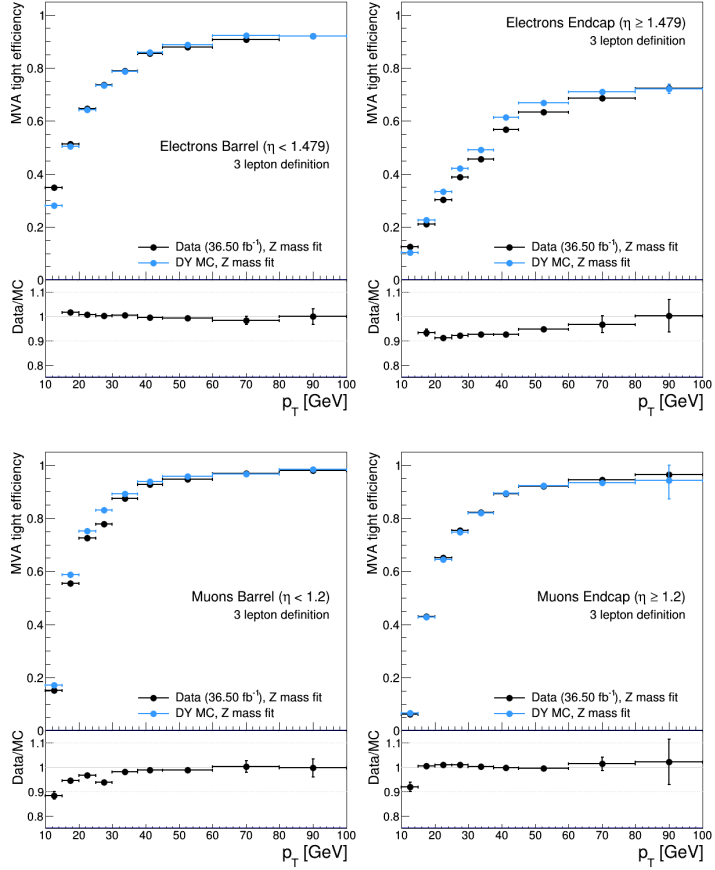


Figure 6.4: Tight vs loose selection efficiencies for electrons (top), and muons (bottom), for the 3l channel not including the tight-charge requirement.

2402 full sample; therefore, the full simulation correction is given by the product of all
 2403 the individual scale factors. The scale factors used in this thesis are inherited from
 2404 the reference [137] which in turns inherited them from leptonic SUSY analyses using
 2405 equivalent lepton selections.

2406 The efficiency of applying the tight selection as defined in Tables 6.8 and 6.9, on the
 2407 loose leptons are determined by using a tag and probe method on a sample of Drell-
 2408 Yan enriched events. Figures 6.3 and 6.4 show the efficiencies for the 2lss channel and
 2409 3l channel respectively. Efficiencies in the 2lss channel have been produced including
 2410 the tight-charge requirement, while for the 3l channel it is not included. Number

2411 of passed and failed probes are determined from a fit to the invariant mass of the
 2412 dilepton system.

2413 Simulation is corrected using these scale factors; note that they depends on η and
 2414 p_T .

2415 **6.6 Event selection**

2416 .

2417 .

2418 .

2419 .

2420 .

2421 .

2422 .

2423 .

2424 .

2425 . . .

2426 The analysis is designed to efficiently identify and select prompt leptons from
 2427 on-shell W and

2428 Z boson decays and to reject non-prompt leptons from b quark decays and spurious
 2429 lepton

2430 signatures from hadronic jets. Events are then selected in the various lepton
 2431 channels, and are

2432 required to contain hadronic jets, some of which must be consistent with b quark
 2433 hadronization. Finally, the signal yield is extracted by simultaneously fitting the
 2434 output of two dedicated

2435 multivariate discriminants (trained to separate the tHq signal from the two dom-
 2436 inant backgrounds) in all categories

2437 . Multivariate techniques are used to discriminate the signal from the dominant
 2438 backgrounds. The analysis yields a 95% confidence level (C.L.) upper limit on the
 2439 combined $tH + ttH$ production cross section times branching ratio of 0.64 pb, with
 2440 an expected limit of 0.32 pb, for a scenario with $kt = \sqrt{1.0}$ and $kV = 1.0$. Values
 2441 of kt outside the range of $\sqrt{1.25}$ to $\sqrt{1.60}$ are excluded at 95% C.L., assuming kV
 2442 $= 1.0$.

2443 Dont forget to mention previous constrains to ct check reference ?? and references
 2444 <https://link.springer.com/content/pdf/10.1007%2FJHEP01%282013%29088.pdf> (para-
 2445 graph after eq 2)

2446 We selects events with three leptons and a b -jet tagged jet in the final state. The tHq
 2447 signal contribution is then determined in a fit of the observed data to two multivariate
 2448 classifier outputs, each trained to discriminate against one of the two dominant back-
 2449 grounds of events with non-prompt leptons from $t\bar{t}$ and of associated production of $t\bar{t}$
 2450 and vector bosons ($t\bar{t}W$, $t\bar{t}Z$). The fit result is then used to set an upper limit on the
 2451 combined $t\bar{t}H$, tHq and tHW production cross section, as a function of the relative
 2452 coupling strengths of Higgs and top quark and Higgs and W boson, respectively.

2453 6.7 Background predictions

2454 The modeling of reducible and irreducible backgrounds in this analysis uses the exact
 2455 methods, analysis code, and ROOT trees used for the $t\bar{t}H$ multilepton analysis. We
 2456 give a brief description of the methods and refer to the documentation of that analysis
 2457 in Refs. [132, 137] for any details.

2458 The backgrounds in three-lepton final states can be split in two broad categories:

irreducible backgrounds with genuine prompt leptons (i.e. from on-shell W and Z boson decays); and reducible backgrounds where at least one of the leptons is “non-prompt”, i.e. produced within a hadronic jet, either a genuine lepton from heavy flavor decays, or simply mis-reconstructed jets.

Irreducible backgrounds can be reliably estimated directly from Monte-Carlo simulated events, using higher-order cross sections or data control regions for the overall normalization. This is done in this analysis for all backgrounds involving prompt leptons: $t\bar{t}W$, $t\bar{t}Z$, $t\bar{t}H$, WZ , ZZ , $W^\pm W^\pm qq$, $t\bar{t}t\bar{t}$, tZq , tZW , WWW , WWZ , WZZ , ZZZ .

Reducible backgrounds, on the other hand, are not well predicted by simulation, and are estimated using data-driven methods. In the case of non-prompt leptons, a fake rate method is used,

Additional identification criteria are applied for electrons with p_T greater than 30 GeV to mimic the identification applied at trigger level in order to ensure consistency between the measurement region and application region of the fake-rate.

where the contribution to the final selection is estimated by extrapolating from a sideband (or “application region”) with a looser lepton definition (the fakeable object definitions in Tabs. 6.8 and 6.9) to the signal selection. The tight-to-loose ratios (or “fake rates”) are measured in several background dominated data events with dedicated triggers, subtracting the residual prompt lepton contribution using MC. Non-prompt leptons in our signal regions are predominantly produced in $t\bar{t}$ events, with a much smaller contribution, from Drell–Yan production. The systematic uncertainty on the normalization of the non-prompt background estimation is on the order of 50%, and thereby one of the dominant limitations on the performance of multilepton analyses in general and this analysis in particular. It consists of several individual sources, such as the result of closure tests of the method using simulated

2485 events, limited statistics in the data control regions due to necessary prescaling of
 2486 lepton triggers, and the uncertainty in the subtraction of residual prompt leptons
 2487 from the control region.

2488 The fake background where the leptons pass the looser selection are weighted
 2489 according to how many of them fail the tight criteria. Events with a single failing
 2490 lepton are weighted with the factor $f/(1-f)$ for the estimate to the tight selection
 2491 region, where f is the fake rate. Events with two failing leptons are given the negative
 2492 weight $-f_i f_j / (1-f_i)(1-f_j)$, and for three leptons the weight is positive and equal
 2493 to the product of $f/(1-f)$ factor evaluated for each failing lepton.

2494 Figures 6.5 show the distributions of some relevant kinematic variables, normalized
 2495 to the cross section of the respective processes and to the integrated luminosity.

2496 6.8 Signal discrimination

2497 The tHq signal is separated from the main backgrounds using a boosted decision
 2498 tree (BDT) classifier, trained on simulated signal and background events. A set
 2499 of discriminating variables are given as input to the BDT which produces a output
 2500 distribution maximizing the discrimination power. Table 6.10 lists the input variables
 2501 used while Figures 6.6 show their distributions for the relevant signal and background
 2502 samples, for the three lepton channel. Two BDT classifiers are trained for the two
 2503 main backgrounds expected in the analysis: events with prompt leptons from $t\bar{t}W$ and
 2504 $t\bar{t}Z$ (also referred to as $t\bar{t}V$), and events with non-prompt leptons from $t\bar{t}$. The datasets
 2505 used in the training are the tHq signal (see Tab. 6.1), and LO MADGRAPH samples
 2506 of $t\bar{t}W$ and $t\bar{t}Z$, in an admixture proportional to their respective cross sections (see
 2507 Tab. 6.4).

2508 The MVA analysis consist of two stages: first a “training” where the MVA method

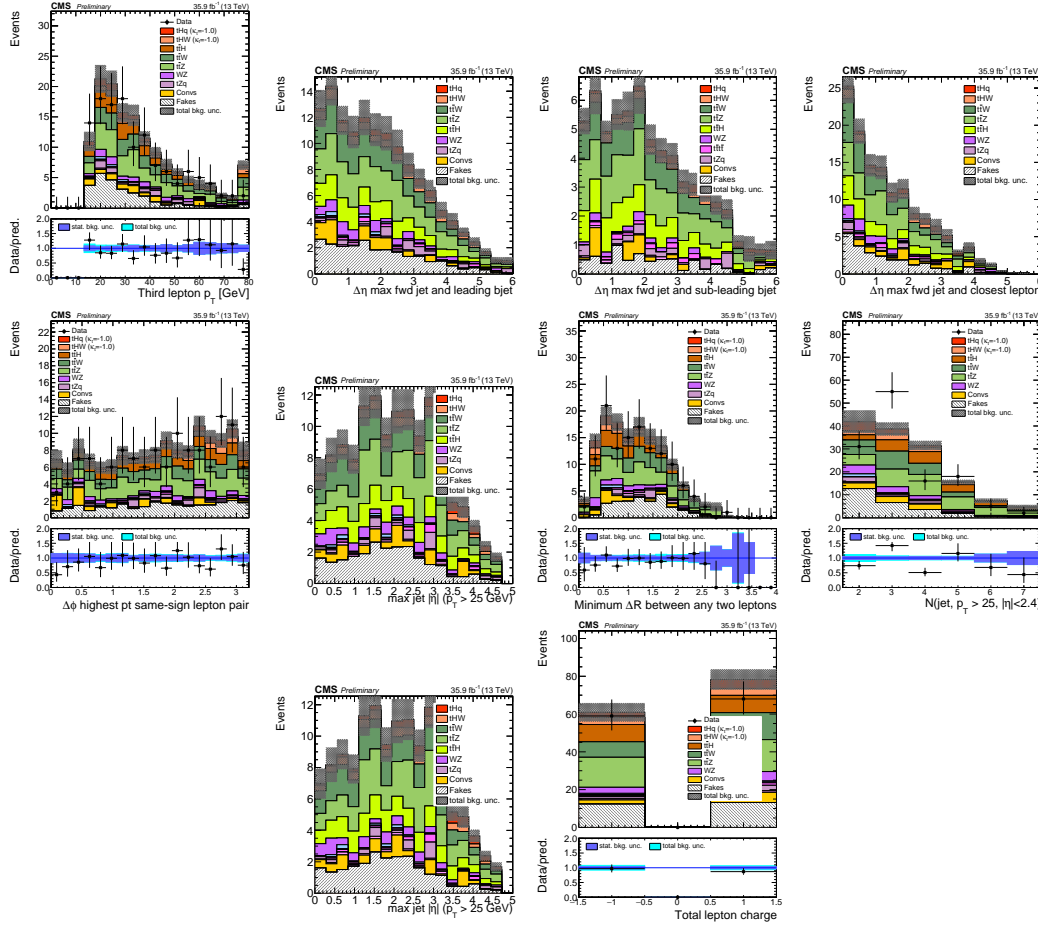


Figure 6.5: Distributions of input variables to the BDT for signal discrimination, three lepton channel, normalized to their cross section and to 35.9 fb^{-1} .

is trained to discriminate between simulated signal and background events, then a “test” stage where the trained algorithm is used to classify different events from the samples. The sample is obtained from a pre-selection (see Tab. ?? with pre-selection cuts). Figures 6.7 show the input variables distributions as seen by the MVA algorithm. Note that in contrast to the distributions in Fig. 6.6 only the main backgrounds ($t\bar{t}$ from simulation, $t\bar{t}V$) are included.

Note that splitting the training in two groups reveals that some variables show opposite behavior for the two background sources; potentially screening the discrimination power if they were to be used in a single discriminant. For some other variables

Variable name	Description
nJet25	Number of jets with $p_T > 25$ GeV, $ \eta < 2.4$
MaxEtaJet25	Maximum $ \eta $ of any (non-CSV-loose) jet with $p_T > 25$ GeV
totCharge	Sum of lepton charges
nJetEta1	Number of jets with $ \eta > 1.0$, non-CSV-loose
detaFwdJetBJet	$\Delta\eta$ between forward light jet and hardest CSV loose jet
detaFwdJet2BJet	$\Delta\eta$ between forward light jet and second hardest CSV loose jet (defaults to -1 in events with only one CSV loose jet)
detaFwdJetClosestLep	$\Delta\eta$ between forward light jet and closest lepton
dphiHighestPtSSPair	$\Delta\phi$ of highest p_T same-sign lepton pair
minDRll	minimum ΔR between any two leptons
Lep3Pt/Lep2Pt	p_T of the 3 rd lepton (2 nd for ss2l)

Table 6.10: MVA input discriminating variables

2518 the distributions are similar in both background cases.

2519 From table 6.10, it is clear that the input variables are correlated to some extend.
 2520 These correlations play an important role for some MVA methods like the Fisher
 2521 discriminant method in which the first step consist of performing a linear transfor-
 2522 mation to an phase space where the correlations between variables are removed. In
 2523 case a boosted decision tree (BDT) method however, correlations do not affect the
 2524 performance. Figure 6.9 show the linear correlation coefficients for signal and back-
 2525 ground for the two training cases (the signal values are identical by construction). As
 2526 expected, strong correlations appears for variables related to the forward jet activity.
 2527 Same trend is seen in case of the same sign dilepton channel in Figure ??.

2528 6.8.1 Classifiers response

2529 Several MVA algorithms were evaluated to determine the most appropriate method
 2530 for this analysis. The plots in Fig. 6.10 (top) show the background rejection as a
 2531 function of the signal efficiency for $t\bar{t}$ and $t\bar{t}V$ trainings (ROC curves) for the different

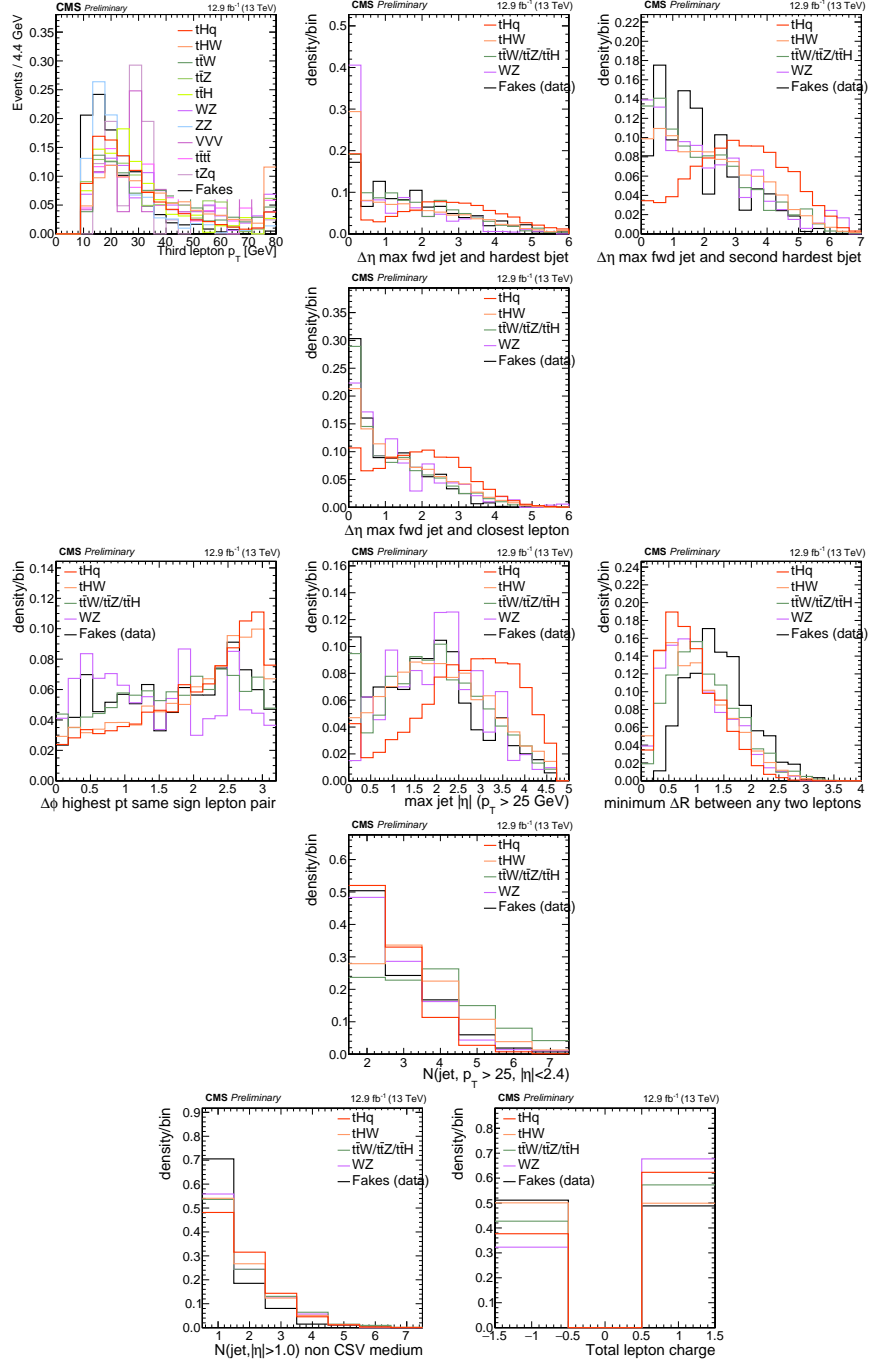


Figure 6.6: Distributions of input variables to the BDT for signal discrimination, three lepton channel.

algorithms that were evaluated.

In both cases the gradient boosted decision tree (“BDTA_GRAD”) classifier offers

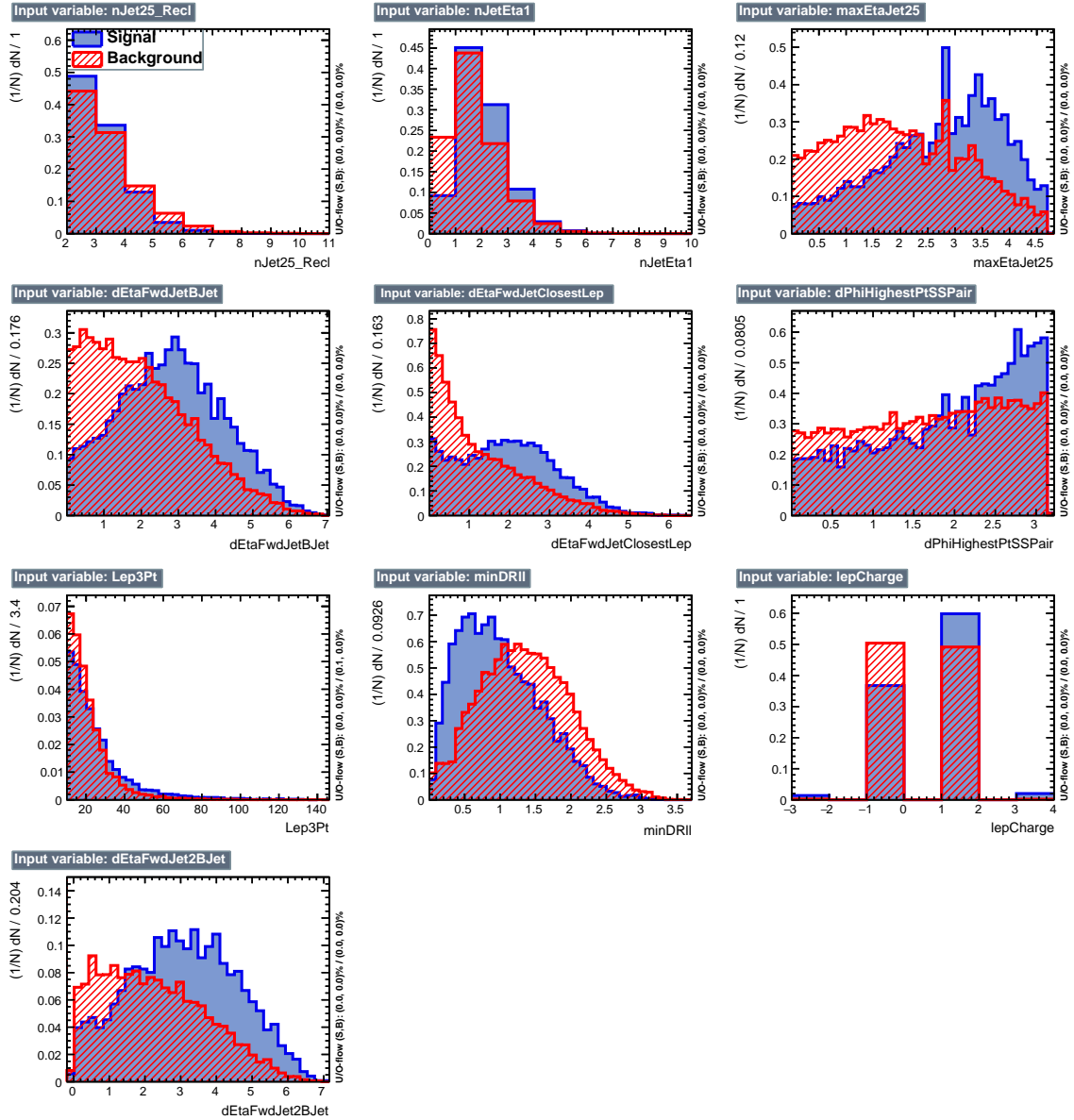


Figure 6.7: BDT inputs as seen by TMVA (signal, in blue, is tHq , background, in red, is $t\bar{t}$) for the three lepton channel, discriminated against $t\bar{t}$ (fakes) background.

the best results, followed by an adaptive BDT classifier (“BDTA”). The BDTA_GRAD classifier output distributions for signal and backgrounds are shown on the bottom of Fig. 6.10. As expected, a good discrimination power is obtained using default discriminator parameter values, with minimal overtraining. TMVA provides a ranking of the input variables by their importance in the classification process, shown in Tab. 6.11.

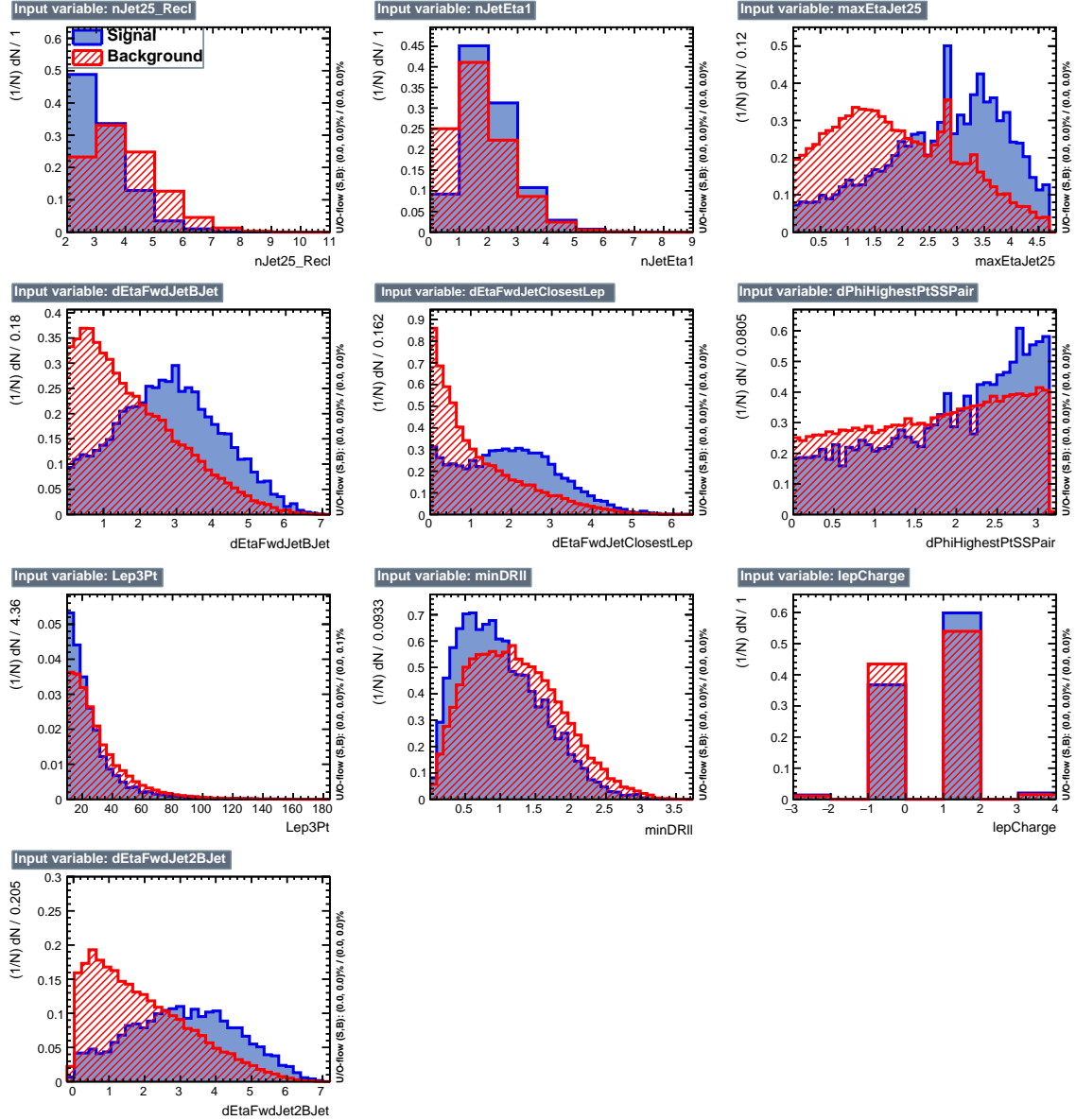


Figure 6.8: BDT inputs as seen by TMVA (signal, in blue, is tHq , background, in red, is $t\bar{t}W+t\bar{t}Z$) for the three lepton channel, discriminated against $t\bar{t}V$ background.

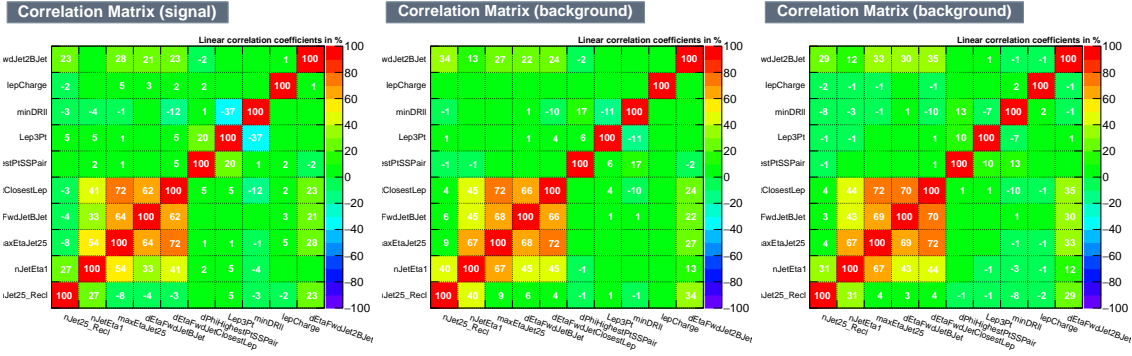


Figure 6.9: Signal (left), $t\bar{t}$ background (middle), and $t\bar{t}V$ background (right.) correlation matrices for the input variables in the TMVA analysis for the three lepton channel.

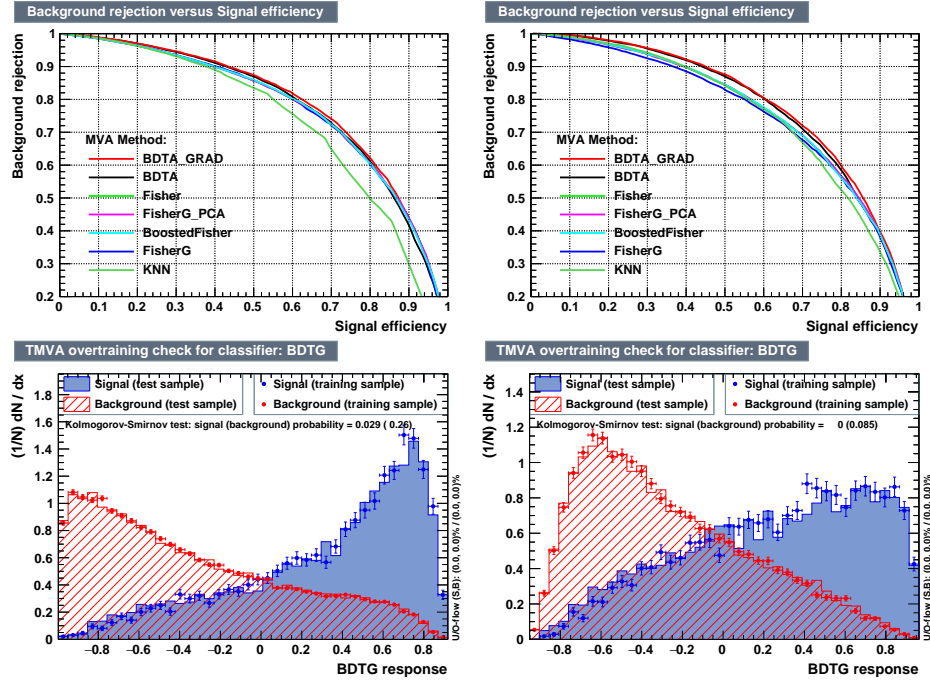


Figure 6.10: Top: background rejection vs signal efficiency (ROC curves) for various MVA classifiers (top) in the three lepton channel against $t\bar{t}V$ (left) and $t\bar{t}$ (right). Bottom: classifier output distributions for the gradient boosted decision trees, for training against $t\bar{t}V$ (left) and against $t\bar{t}$ (right).

2540 6.9 Additional discriminating variables

2541 Two additional discriminating variables were tested considering the fact that the
 2542 forward jet in the background could come from the pileup; since we have a real forward

ttbar training			ttV training		
Rank	Variable	Importance	Variable	Importance	Importance
1	minDRll	1.329e-01	dEtaFwdJetBJet	1.264e-01	
2	dEtaFwdJetClosestLep	1.294e-01	Lep3Pt	1.224e-01	
3	dEtaFwdJetBJet	1.209e-01	maxEtaJet25	1.221e-01	
4	dPhiHighestPtSSPair	1.192e-01	dEtaFwdJet2BJet	1.204e-01	
5	Lep3Pt	1.158e-01	dEtaFwdJetClosestLep	1.177e-01	
6	maxEtaJet25	1.121e-01	minDRll	1.143e-01	
7	dEtaFwdJet2BJet	9.363e-02	dPhiHighestPtSSPair	9.777e-02	
8	nJetEta1	6.730e-02	nJet25_Recl	9.034e-02	
9	nJet25_Recl	6.178e-02	nJetEta1	4.749e-02	
10	lepCharge	4.701e-02	lepCharge	4.116e-02	

Table 6.11: TMVA input variables ranking for BDTA_GRAD method for the trainings in the three lepton channel. For both trainings the rankings show almost the same 5 variables in the first places.

```

TMVA.Types.kBDT
NTrees=800
BoostType=Grad
Shrinkage=0.10
!UseBaggedGrad
nCuts=50
MaxDepth=3
NegWeightTreatment=PairNegWeightsGlobal
CreateMVAPdfs

```

Table 6.12: TMVA configuration used in the BDT training.

jet in the signal, it could give some improvement in the discriminating power. The additional variables describe the forward jet momentum (fwdJetPt25) and the forward jet identification(fwdJetPUID). Distributions for these variables in the three lepton channel are shown in the figure 6.11. The forward jet identification distribution show that for both, signal and background, jets are mostly real jets.

The testing was made including in the MVA input one variable at a time, so we can evaluate the dicrimination power of each variable, and then both simultaneously. fwdJetPUID was ranked in the last place in importance (11) in both training (ttV and tt) while fwdJetPt25 was ranked 3 in the ttV training and 7 in the tt training. When training using 12 variables, fwdJetPt25 was ranked 5 and 7 in the ttV and tt

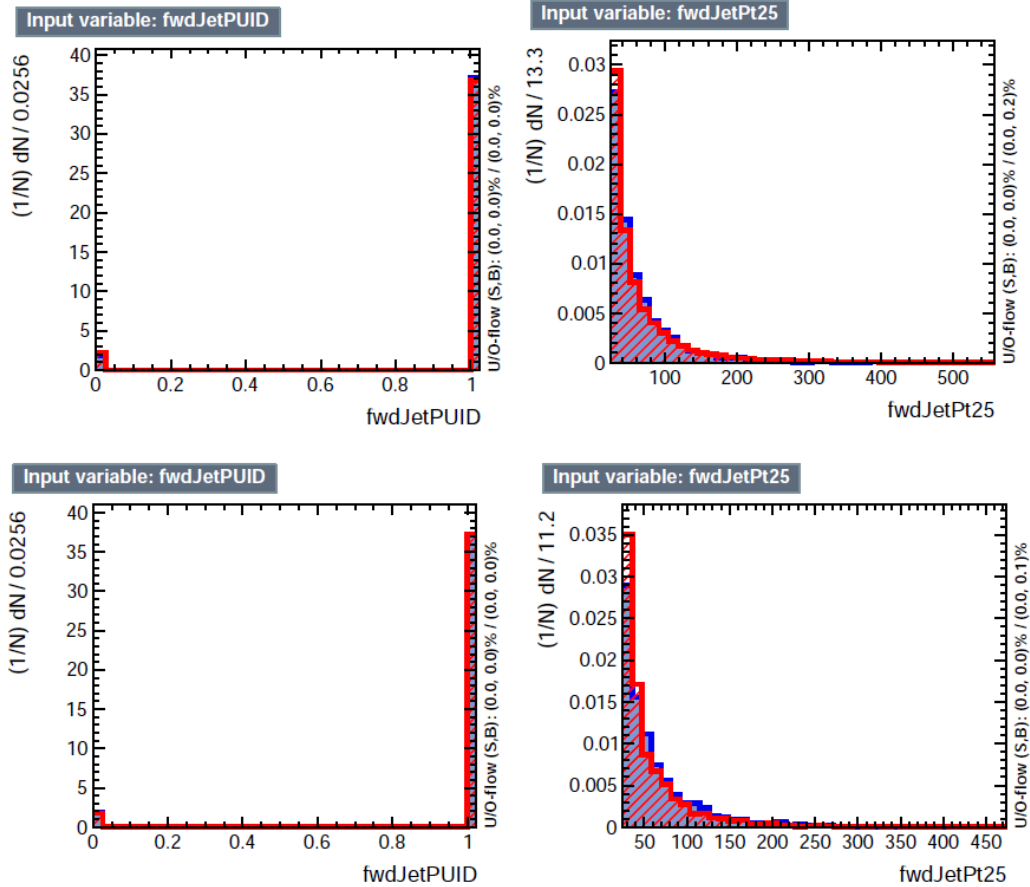


Figure 6.11: Additional discriminating variables distributions for ttv training (Top row) and tt training (bottom row) in the three lepton channel. The origin of the jets in the forward jet identification distribution is tagged as 0 for “pileup jets” while “real jets” are tagged as 1.

2553 trainings respectively, while `fwdJetPUID` was ranked 12 in both cases.

2554 The improvement in the discrimination performance provided by the additional
 2555 variables is about 1%, so it was decided not to include them in the procedure. Table
 2556 6.13 show the ROC-integral for all the testing cases we made.

ROC-integral	
base 10 var ttv	0.848
+ fwdJetPUID ttv	0.849
+ fwdJetPt25 ttv	0.856
12 var ttv	0.856
<hr/>	
base 10 var tt	0.777
+ fwdJetPUID tt	0.777
+ fwdJetPt25 tt	0.787
12 var	0.787

Table 6.13: ROC-integral for all the testing cases we made in the evaluation of the additional variables discriminating power. The improvement in the discrimination performance provided by the additional variables is about 1%

2557 **References**

- 2558 [1] J. Schwinger. "Quantum Electrodynamics. I. A Covariant Formulation". Phys-
2559 ical Review. 74 (10): 1439-61, (1948). <https://doi.org/10.1103/PhysRev.74.1439>
- 2560
- 2561 [2] R. P. Feynman. "Space-Time Approach to Quantum Electrodynamics". Physical
2562 Review. 76 (6): 769-89, (1949). <https://doi.org/10.1103/PhysRev.76.769>
- 2563 [3] S. Tomonaga. "On a Relativistically Invariant Formulation of the Quantum
2564 Theory of Wave Fields". Progress of Theoretical Physics. 1 (2): 27-42, (1946).
2565 <https://doi.org/10.1143/PTP.1.27>
- 2566 [4] D.J. Griffiths, "Introduction to electrodynamics". 4th ed. Pearson, (2013).
- 2567 [5] F. Mandl, G. Shaw. "Quantum field theory." Chichester, Wiley (2009).
- 2568 [6] F. Halzen, and A.D. Martin, "Quarks and leptons: An introductory course in
2569 modern particle physics". New York: Wiley, (1984) .
- 2570 [7] File: Standard_Model_of_Elementary_Particle_dark.svg. (2017, June 12)
2571 Wikimedia Commons, the free media repository. Retrieved November 27, 2017
2572 from <https://www.collegiate-advanced-electricity.com/single-post/2017/04/10/The-Standard-Model-of-Particle-Physics>.
- 2573

- 2574 [8] E. Noether, "Invariante Variationsprobleme", Nachrichten von der Gesellschaft
2575 der Wissenschaften zu Göttingen, mathematisch-physikalische Klasse, vol. 1918,
2576 pp. 235-257, (1918).
- 2577 [9] C. Patrignani et al. (Particle Data Group), Chin. Phys. C, 40, 100001 (2016)
2578 and 2017 update.
- 2579 [10] M. Goldhaber, L. Grodzins, A.W. Sunyar "Helicity of Neutrinos", Phys. Rev.
2580 109, 1015 (1958).
- 2581 [11] Palanque-Delabrouille N et al. "Neutrino masses and cosmology with Lyman-
2582 alpha forest power spectrum", JCAP 11 011 (2015).
- 2583 [12] M. Gell-Mann. "A Schematic Model of Baryons and Mesons". Physics Letters.
2584 8 (3): 214-215 (1964).
- 2585 [13] G. Zweig. "An SU(3) Model for Strong Interaction Symmetry and its Breaking"
2586 (PDF). CERN Report No.8182/TH.401 (1964).
- 2587 [14] G. Zweig. "An SU(3) Model for Strong Interaction Symmetry and its Breaking:
2588 II" (PDF). CERN Report No.8419/TH.412(1964).
- 2589 [15] M. Gell-Mann. "The Interpretation of the New Particles as Displaced Charged
2590 Multiplets". Il Nuovo Cimento 4: 848. (1956).
- 2591 [16] T. Nakano, K. Nishijima. "Charge Independence for V-particles". Progress of
2592 Theoretical Physics 10 (5): 581-582. (1953).
- 2593 [17] N. Cabibbo, "Unitary symmetry and leptonic decays" Physical Review Letters,
2594 vol. 10, no. 12, p. 531, (1963).

- 2595 [18] M.Kobayashi, T.Maskawa, “CP-violation in the renormalizable theory of weak
2596 interaction,” Progress of Theoretical Physics, vol. 49, no. 2, pp. 652-657, (1973).
- 2597 [19] File: Weak Decay (flipped).svg. (2017, June 12). Wikimedia Com-
2598 mons, the free media repository. Retrieved November 27, 2017
2599 from [https://commons.wikimedia.org/w/index.php?title=File:
2600 Weak_Decay_\(flipped\)\.svg&oldid=247498592](https://commons.wikimedia.org/w/index.php?title=File:Weak_Decay_(flipped)\.svg&oldid=247498592).
- 2601 [20] Georgia Tech University. Coupling Constants for the Fundamental Forces(2005).
2602 Retrieved January 10, 2018, from [http://hyperphysics.phy-astr.gsu.edu/
2603 hbase/Forces/couple.html#c2](http://hyperphysics.phy-astr.gsu.edu/hbase/Forces/couple.html#c2)
- 2604 [21] M. Strassler. (May 31, 2013).The Strengths of the Known Forces. Retrieved Jan-
2605 uary 10, 2018, from [https://profmattstrassler.com/articles-and-posts/
2606 particle-physics-basics/the-known-forces-of-nature/
2607 the-strength-of-the-known-forces/](https://profmattstrassler.com/articles-and-posts/particle-physics-basics/the-known-forces-of-nature/the-strength-of-the-known-forces/)
- 2608 [22] S.L. Glashow. “Partial symmetries of weak interactions”, Nucl. Phys. 22 579-
2609 588, (1961).
- 2610 [23] A. Salam, J.C. Ward. “Electromagnetic and weak interactions”, Physics Letters
2611 13 168-171, (1964).
- 2612 [24] S. Weinberg, “A model of leptons”, Physical Review Letters, vol. 19, no. 21, p.
2613 1264, (1967).
- 2614 [25] M. Peskin, D. Schroeder, “An introduction to quantum field theory”. Perseus
2615 Books Publishing L.L.C., (1995).
- 2616 [26] A. Pich. “The Standard Model of Electroweak Interactions” <https://arxiv.org/abs/1201.0537>
- 2617

- 2618 [27] G. Arnison et al. (UA1 Collaboration), Phys. Lett. B 122, 103 (1983).
- 2619 [28] M. Banner et al. (UA2 Collaboration), Phys. Lett. B 122, 476 (1983).
- 2620 [29] G. Arnison et al. (UA1 Collaboration), Phys. Lett. B 126, 398 (1983).
- 2621 [30] P. Bagnaia et al. (UA2 Collaboration), Phys. Lett. B 129, 130 (1983).
- 2622 [31] F.Bellaiche. (2012, 2 September). “What’s this Higgs boson anyway?”. Retrieved
2623 from: <https://www.quantum-bits.org/?p=233>
- 2624 [32] M. Endres et al. Nature 487, 454-458 (2012) doi:10.1038/nature11255
- 2625 [33] F. Englert, R. Brout. “Broken Symmetry and the Mass of Gauge
2626 Vector Mesons”. Physical Review Letters. 13 (9): 321-23.(1964)
2627 doi:10.1103/PhysRevLett.13.321
- 2628 [34] P.Higgs. “Broken Symmetries and the Masses of Gauge Bosons”. Physical Re-
2629 view Letters. 13 (16): 508-509,(1964). doi:10.1103/PhysRevLett.13.508.
- 2630 [35] G.Guralnik, C.R. Hagen and T.W.B. Kibble. “Global Conservation Laws
2631 and Massless Particles”. Physical Review Letters. 13 (20): 585-587, (1964).
2632 doi:10.1103/PhysRevLett.13.585.
- 2633 [36] CMS collaboration. “Observation of a new boson at a mass of 125 GeV with
2634 the CMS experiment at the LHC”. Physics Letters B. 716 (1): 30-61 (2012).
2635 arXiv:1207.7235. doi:10.1016/j.physletb.2012.08.021
- 2636 [37] ATLAS collaboration. “Observation of a New Particle in the Search for the Stan-
2637 dard Model Higgs Boson with the ATLAS Detector at the LHC”. Physics Letters
2638 B. 716 (1): 1-29 (2012). arXiv:1207.7214. doi:10.1016/j.physletb.2012.08.020.

- 2639 [38] ATLAS collaboration; CMS collaboration (26 March 2015). “Combined Mea-
 2640 surement of the Higgs Boson Mass in pp Collisions at $\sqrt{s}=7$ and 8 TeV with
 2641 the ATLAS and CMS Experiments”. Physical Review Letters. 114 (19): 191803.
 2642 arXiv:1503.07589. doi:10.1103/PhysRevLett.114.191803.
- 2643 [39] LHC InternationalMasterclasses“When protons collide”. Retrieved from http://atlas.physicsmasterclasses.org/en/zpath_protoncollisions.htm
- 2645 [40] CMS Collaboration, “SM Higgs Branching Ratios and Total Decay Widths (up-
 2646 date in CERN Report4 2016)”. <https://twiki.cern.ch/twiki/bin/view/LHCPhysics/CERNYellowReportPageBR> , last accessed on 17.12.2017.
- 2648 [41] R.Grant V. “Determination of Higgs branching ratios in $H \rightarrow W^+W^- \rightarrow l\nu jj$
 2649 and $H \rightarrow ZZ \rightarrow l^+l^-jj$ channels”. Physics Department, University of Ten-
 2650 nessee (Dated: October 31, 2012). Retrieved from <http://aesop.phys.utk.edu/ph611/2012/projects/Riley.pdf>
- 2652 [42] LHC Higgs Cross Section Working Group, Denner, A., Heinemeyer, S. et al.
 2653 “Standard model Higgs-boson branching ratios with uncertainties”. Eur. Phys.
 2654 J. C (2011) 71: 1753. <https://doi.org/10.1140/epjc/s10052-011-1753-8>
- 2655 [43] D. de Florian et al., LHC Higgs Cross Section Working Group,
 2656 CERNâš2017âš002-M, arXiv:1610.07922[hep-ph] (2016).
- 2657 [44] F. Maltoni, K. Paul, T. Stelzer, and S. Willenbrock, “Associated production
 2658 of Higgs and single top at hadron colliders”, Phys.Rev. D64 (2001) 094023,
 2659 [hep-ph/0106293].

- 2660 [45] S. Biswas, E. Gabrielli, F. Margaroli, and B. Mele, “Direct constraints on the
 2661 top-Higgs coupling from the 8 TeV LHC data,” Journal of High Energy Physics,
 2662 vol. 07, p. 073, (2013).
- 2663 [46] M. Farina, C. Grojean, F. Maltoni, E. Salvioni, and A. Thamm, “Lifting de-
 2664 generacies in Higgs couplings using single top production in association with a
 2665 Higgs boson,” Journal of High Energy Physics, vol. 05, p. 022, (2013).
- 2666 [47] T.M. Tait and C.-P. Yuan, “Single top quark production as a window to physics
 2667 beyond the standard model”, Phys. Rev. D 63 (2000) 014018 [hep-ph/0007298].
- 2668 [48] F. Demartin, F. Maltoni, K. Mawatari, and M. Zaro, “Higgs production in
 2669 association with a single top quark at the LHC,” European Physical Journal C,
 2670 vol. 75, p. 267, (2015).
- 2671 [49] CMS Collaboration, “Modelling of the single top-quark production in associa-
 2672 tion with the Higgs boson at 13 TeV.” [https://twiki.cern.ch/twiki/bin/](https://twiki.cern.ch/twiki/bin/viewauth/CMS/SingleTopHiggsGeneration13TeV)
 2673 [viewauth/CMS/SingleTopHiggsGeneration13TeV](#), last accessed on 16.01.2018.
- 2674 [50] CMS Collaboration, “SM Higgs production cross sections at $\sqrt{s} =$
 2675 13 TeV.” [https://twiki.cern.ch/twiki/bin/view/LHCPhysics/](https://twiki.cern.ch/twiki/bin/view/LHCPhysics/CERNYellowReportPageAt13TeV)
 2676 [CERNYellowReportPageAt13TeV](#), last accessed on 16.01.2018.
- 2677 [51] S. Dawson, The effective W approximation, Nucl. Phys. B 249 (1985) 42.
- 2678 [52] S. Biswas, E. Gabrielli and B. Mele, JHEP 1301 (2013) 088 [arXiv:1211.0499
 2679 [hep-ph]].
- 2680 [53] F. Demartin, B. Maier, F. Maltoni, K. Mawatari, and M. Zaro, “tWH associated
 2681 production at the LHC”, European Physical Journal C, vol. 77, p. 34, (2017).
 2682 arXiv:1607.05862

- 2683 [54] LHC Higgs Cross Section Working Group, “Handbook of LHC Higgs Cross
2684 Sections: 4.Deciphering the Nature of the Higgs Sector”, arXiv:1610.07922.
- 2685 [55] J. Ellis, D. S. Hwang, K. Sakurai, and M. Takeuchi.“Disentangling Higgs-Top
2686 Couplings in Associated Production”, JHEP 1404 (2014) 004, [arXiv:1312.5736].
- 2687 [56] CMS Collaboration, V. Khachatryan et al., “Precise determination of the mass
2688 of the Higgs boson and tests of compatibility of its couplings with the standard
2689 model predictions using proton collisions at 7 and 8 TeV,” arXiv:1412.8662.
- 2690 [57] ATLAS Collaboration, G. Aad et al., “Updated coupling measurements of the
2691 Higgs boson with the ATLAS detector using up to 25 fb^{-1} of proton-proton
2692 collision data”, ATLAS-CONF-2014-009.
- 2693 [58] ATLAS and CMS Collaborations, “Measurements of the Higgs boson produc-
2694 tion and decay rates and constraints on its couplings from a combined ATLAS
2695 and CMS analysis of the LHC pp collision data at $\sqrt{s} = 7$ and 8 TeV,” (2016).
2696 CERN-EP-2016-100, ATLAS-HIGG-2015-07, CMS-HIG-15-002.
- 2697 [59] File:Cern-accelerator-complex.svg. Wikimedia Commons, the free media repos-
2698 itory. Retrieved January, 2018 from <https://commons.wikimedia.org/wiki/File:Cern-accelerator-complex.svg>
- 2700 [60] J.L. Caron , “Layout of the LEP tunnel including future LHC infrastructures.”,
2701 (Nov, 1993). A C Collection. Legacy of AC. Pictures from 1992 to 2002. Re-
2702 trieved from <https://cds.cern.ch/record/841542>
- 2703 [61] M. Vretenar, “The radio-frequency quadrupole”. CERN Yellow Report CERN-
2704 2013-001, pp.207-223 DOI:10.5170/CERN-2013-001.207. arXiv:1303.6762
- 2705 [62] L.Evans. P. Bryant (editors). “LHC Machine”. JINST 3 S08001 (2008).

- 2706 [63] CERN Photographic Service.“Radio-frequency quadrupole, RFQ-1”, March
2707 1983, CERN-AC-8303511. Retrieved from <https://cds.cern.ch/record/615852>.
- 2709 [64] CERN Photographic Service “Animation of CERN’s accelerator network”, 14
2710 October 2013. DOI: 10.17181/cds.1610170 Retrieved from <https://videos.cern.ch/record/1610170>
- 2712 [65] C.Sutton. “Particle accelerator”.Encyclopedia Britannica. July 17,
2713 2013. Retrieved from <https://www.britannica.com/technology/particle-accelerator>.
- 2715 [66] L.Guiraud. “Installation of LHC cavity in vacuum tank.”. July 27 2000. CERN-
2716 AC-0007016. Retrieved from <https://cds.cern.ch/record/41567>.
- 2717 [67] J.L. Caron, “Magnetic field induced by the LHC dipole’s superconducting coils”.
2718 March 1998. AC Collection. Legacy of AC. Pictures from 1992 to 2002. LHC-
2719 PHO-1998-325. Retrieved from <https://cds.cern.ch/record/841511>.
- 2720 [68] AC Team. “Diagram of an LHC dipole magnet”. June 1999. CERN-DI-9906025
2721 retrieved from <https://cds.cern.ch/record/40524>.
- 2722 [69] CMS Collaboration “Public CMS Luminosity Information”. https://twiki.cern.ch/twiki/bin/view/CMSPublic/LumiPublicResults#2016_proton_proton_13_TeV_collis, last accessed 24.01.2018
- 2725 [70] J.L Caron. “LHC Layout” AC Collection. Legacy of AC. Pictures from 1992
2726 to 2002. September 1997, LHC-PHO-1997-060. Retrieved from <https://cds.cern.ch/record/841573>.

- 2728 [71] J.A. Coarasa. “The CMS Online Cluster:Setup, Operation and Maintenance
2729 of an Evolving Cluster”. ISGC 2012, 26 February - 2 March 2012, Academia
2730 Sinica, Taipei, Taiwan.
- 2731 [72] CMS Collaboration. “The CMS experiment at the CERN LHC” JINST 3 S08004
2732 (2008).
- 2733 [73] CMS Collaboration. “CMS detector drawings 2012” CMS-PHO-GEN-2012-002.
2734 Retrieved from <http://cds.cern.ch/record/1433717>.
- 2735 [74] Davis, Siona Ruth. “Interactive Slice of the CMS detector”, Aug. 2016,
2736 CMS-OUTREACH-2016-027, retrieved from [https://cds.cern.ch/record/](https://cds.cern.ch/record/2205172)
2737 2205172
- 2738 [75] R. Breedon. “View through the CMS detector during the cooldown of the
2739 solenoid on February 2006. CMS Collection”, February 2006, CMS-PHO-
2740 OREACH-2005-004, Retrieved from <https://cds.cern.ch/record/930094>.
- 2741 [76] Halyo, V. and LeGresley, P. and Lujan, P. “Massively Parallel Computing and
2742 the Search for Jets and Black Holes at the LHC”, Nucl.Instrum.Meth. A744
2743 (2014) 54-60, DOI: 10.1016/j.nima.2014.01.038”
- 2744 [77] A. Dominguez et. al. “CMS Technical Design Report for the Pixel Detector
2745 Upgrade”, CERN-LHCC-2012-016. CMS-TDR-11.
- 2746 [78] CMS Collaboration. “Description and performance of track and primary-vertex
2747 reconstruction with the CMS tracker,” Journal of Instrumentation, vol. 9, no.
2748 10, p. P10009,(2014).

- 2749 [79] CMS Collaboration and M. Brice. “Images of the CMS Tracker Inner Bar-
2750 rel”, November 2008, CMS-PHO-TRACKER-2008-002. Retrieved from <https://cds.cern.ch/record/1431467>.
2751
- 2752 [80] M. Weber. “The CMS tracker”. 6th international conference on hyperons, charm
2753 and beauty hadrons Chicago, June 28-July 3 2004.
2754
- 2755 [81] CMS Collaboration. “Projected Performance of an Upgraded CMS Detector at
the LHC and HL-LHC: Contribution to the Snowmass Process”. Jul 26, 2013.
2756 arXiv:1307.7135
- 2757 [82] L. Veillet. “End assembly of HB with EB rails and rotation inside SX ”,Jan-
2758 uary 2002. CMS-PHO-HCAL-2002-002. Retrieved from <https://cds.cern.ch/record/42594>.
2759
- 2760 [83] J. Puerta-Pelayo.“First DT+RPC chambers installation round in the UX5 cav-
2761 ern.”. January 2007, CMS-PHO-OREACH-2007-001. Retrieved from <https://cds.cern.ch/record/1019185>
2762
- 2763 [84] X. Cid Vidal and R. Cid Manzano. “CMS Global Muon Trigger” web site:
2764 Taking a closer look at LHC. Retrieved from https://www.lhc-closer.es/taking_a_closer_look_at_lhc/0.lhc_trigger
2765
- 2766 [85] WLCG Project Office, “Documents & Reference - Tiers - Structure,”
2767 (2014). <http://wlcg.web.cern.ch/documents-reference> , last accessed on
2768 30.01.2018.
2769
- 2770 [86] CMS Collaboration. “CMSSW Application Framework”, <https://twiki.cern.ch/twiki/bin/view/CMSPublic/WorkBookCMSSWFramework>,
2771 last accesses 06.02.2018

- 2772 [87] A. Buckleya, J. Butterworthb, S. Giesekec, et. al. “General-purpose event gen-
 2773 erators for LHC physics”. arXiv:1101.2599v1 [hep-ph] 13 Jan 2011
- 2774 [88] A. Quadt. “Top Quark Physics at Hadron Colliders”. Advances in the Physics
 2775 of Particles and Nuclei. Springer-Verlag Berlin Heidelberg. DOI: 10.1007/978-
 2776 3-540-71060-8 (2007)
- 2777 [89] DurhamHep Data Project, “The Durham HepData Project - PDF Plotter”
 2778 <http://hepdata.cedar.ac.uk/pdf/pdf3.html> , last accessed on 02.02.2018.
- 2779 [90] G. Altarelli and G. Parisi. “ASYMPTOTIC FREEDOM IN PARTON LAN-
 2780 GUAGE”, Nucl.Phys. B126:298 (1977).
- 2781 [91] Yu.L. Dokshitzer. Sov.Phys. JETP 46:641 (1977)
- 2782 [92] V.N. Gribov, L.N. Lipatov. “Deep inelastic e p scattering in perturbation the-
 2783 ory”, Sov.J.Nucl.Phys. 15:438 (1972)
- 2784 [93] F. Maltoni, G. Ridolfi, and M. Ubiali, “b-initiated processes at the LHC: a
 2785 reappraisal,” Journal of High Energy Physics, vol. 07, p. 022, (2012).
- 2786 [94] B. Andersson, G. Gustafson, G. Ingelman and T. Sjostrand, “Parton fragmen-
 2787 tation and string dynamics”, Physics Reports, Vol. 97, No. 2-3, pp. 31-145,
 2788 1983.
- 2789 [95] CMS Collaboration, “Event generator tunes obtained from underlying event
 2790 and multiparton scattering measurements;” European Physical Journal C, vol.
 2791 76, no. 3, p. 155, (2016).
- 2792 [96] J. Alwall et. al., “The automated computation of tree-level and next-to-leading
 2793 order differential cross sections, and their matching to parton shower simula-
 2794 tions,” Journal of High Energy Physics, vol. 07, p. 079, (2014).

- 2795 [97] S. Frixione, P. Nason, and C. Oleari, “Matching NLO QCD computations with
 2796 Parton Shower simulations: the POWHEG method,” Journal of High Energy
 2797 Physics, vol. 11, p. 070, (2007).
- 2798 [98] S. Agostinelli et al., “GEANT4: A Simulation toolkit,” Nuclear Instruments
 2799 and Methods in Physics, vol. A506, pp. 250–303, (2003).
- 2800 [99] J.Allison et.al.,“Recent developments in Geant4”, Nuclear Instruments and
 2801 Methods in Physics Research A 835 (2016) 186-225.
- 2802 [100] CMS Collaboration “Full Simulation Offline Guide”, <https://twiki.cern.ch/twiki/bin/view/CMSPublic/SWGuideSimulation>, last accessed 04.02.2018
- 2803
- 2804 [101] A. Giammanco. “The Fast Simulation of the CMS Experiment” J. Phys.: Conf.
 2805 Ser. 513 022012 (2014)
- 2806 [102] A.M. Sirunyan et. al. “Particle-flow reconstruction and global event description
 2807 with the CMS detector”, JINST 12 P10003 (2017) <https://doi.org/10.1088/1748-0221/12/10/P10003>.
- 2808
- 2809 [103] The CMS Collaboration. “ Description and performance of track and pri-
 2810 mary vertex reconstruction with the CMS tracker”. JINST 9 P10009 (2014).
 2811 doi:10.1088/1748-0221/9/10/P10009
- 2812 [104] J. Incandela. “Status of the CMS SM Higgs Search” July 4, 2012. Pdf slides.
 2813 Retrieved from https://indico.cern.ch/event/197461/contributions/1478917/attachments/290954/406673/CMS_4July2012_Final.pdf
- 2814
- 2815 [105] P. Billoir and S. Qian, “Simultaneous pattern recognition and track fitting by
 2816 the Kalman filtering method”, Nucl. Instrum. Meth. A 294 219. (1990).

- 2817 [106] W. Adam, R. Fruhwirth, A. Strandlie and T. Todorov, “Reconstruction of
2818 electrons with the Gaussian sum filter in the CMS tracker at LHC”, eConf
2819 C 0303241 (2003) TULT009 [physics/0306087].
- 2820 [107] K. Rose, “Deterministic Annealing for Clustering, Compression, Classification,
2821 Regression and related Optimisation Problems”, Proc. IEEE 86 (1998) 2210.
- 2822 [108] R. Fruhwirth, W. Waltenberger and P. Vanlaer, “ Adaptive Vertex Fitting”,
2823 CMS Note 2007-008 (2007).
- 2824 [109] CMS collaboration, “Performance of CMS muon reconstruction in pp collision
2825 events at $\sqrt{s} = 7$ TeV ”, JINST 7 P10002 2012, [arXiv:1206.4071].
- 2826 [110] M. Cacciari, G. P. Salam, and G. Soyez, “The anti- k_t jet clustering algorithm,”
2827 Journal of High Energy Physics, vol. 04, p. 063, (2008).
- 2828 [111] B. Dorney. “Anatomy of a Jet in CMS”. Quantum Diaries. June
2829 1st, 2011. Retrieved from <https://www.quantumdiaries.org/2011/06/01/anatomy-of-a-jet-in-cms/>
- 2831 [112] The CMS Collaboration.“Event Displays from the high-energy collisions at 7
2832 TeV”, May 2010, CMS-PHO-EVENTS-2010-007, Retrieved from <https://cds.cern.ch/record/1429614>.
- 2834 [113] The CMS collaboration. “Determination of jet energy calibration and transverse
2835 momentum resolution in CMS”. JINST 6 P11002 (2011). <http://dx.doi.org/10.1088/1748-0221/6/11/P11002>
- 2837 [114] The CMS Collaboration, “Introduction to Jet Energy Corrections at
2838 CMS.”. <https://twiki.cern.ch/twiki/bin/view/CMS/IntroToJEC>, last ac-
2839 cessed 10.02.2018.

- 2840 [115] CMS Collaboration Collaboration. “Identification of b quark jets at the CMS
2841 Experiment in the LHC Run 2”. Tech. rep. CMS-PAS-BTV-15-001. Geneva:
2842 CERN, (2016). <https://cds.cern.ch/record/2138504>.
- 2843 [116] CMS Collaboration Collaboration. “Performance of missing energy reconstruc-
2844 tion in 13 TeV pp collision data using the CMS detector”. Tech. rep. CMS-PAS-
2845 JME16-004. Geneva: CERN, 2016. <https://cds.cern.ch/record/2205284>.
- 2846 [117] CMS Collaboration, “New CMS results at Moriond (Electroweak) 2013”,
2847 Retrieved from <http://cms.web.cern.ch/sites/cms.web.cern.ch/files/>
2848 styles/large/public/field/image/HIG13004_Event01_0.png?itok=
2849 LAwZzPHR
- 2850 [118] CMS Collaboration, “New CMS results at Moriond (Electroweak) 2013”,
2851 Retrieved from <http://cms.web.cern.ch/sites/cms.web.cern.ch/>
2852 files/styles/large/public/field/image/TOP12035_Event01.png?itok=
2853 uMdnSqzC
- 2854 [119] K. Skovpen. “Event displays highlighting the main properties of heavy flavour
2855 jets in the CMS Experiment”, Aug 2017, CMS-PHO-EVENTS-2017-006. Re-
2856 trieval from <https://cds.cern.ch/record/2280025>.
- 2857 [120] G. Cowan. “Topics in statistical data analysis for high-energy physics”.
2858 arXiv:1012.3589v1
- 2859 [121] A. Hoecker et al., “TMVA-Toolkit for multivariate data analysis”
2860 arXiv:physics/0703039v5 (2009)

- 2861 [122] L. Lista. “Statistical Methods for Data Analysis in Particle Physics”, 2nd
2862 ed. Springer International Publishing. (2017) <https://dx.doi.org/10.1007/978-3-319-62840-0>
- 2864 [123] I. Antcheva et al., “ROOT-A C++ framework for petabyte data storage, sta-
2865 tistical analysis and visualization ,” Computer Physics Communications, vol.
2866 182, no. 6, pp. 1384â€¢1385, (2011).
- 2867 [124] Y. Coadou. “Boosted decision trees”, ESIPAP, Archamps, 9 Febru-
2868 ary 2016. Lecture. Retrieved from https://indico.cern.ch/event/472305/contributions/1982360/attachments/1224979/1792797/ESIPAP_MVA160208-BDT.pdf
- 2871 [125] J.H. Friedman. “Greedy function approximation: A gradient boosting ma-
2872 chine”. Ann. Statist. Volume 29, Number 5 (2001), 1189-1232. https://projecteuclid.org/download/pdf_1/euclid-aos/1013203451.
- 2874 [126] F. James, M. Roos, “MINUIT: Function minimization and error analysis”. Cern
2875 Computer Centre Program Library, Geneve Long Write-up No. D506, 1989
- 2876 [127] J. Neyman and E. S. Pearson, “On the problem of the most efficient tests
2877 of statistical hypotheses”. Philosophical Transactions of the Royal Society of
2878 London. Series A, Containing Papers of a Mathematical or Physical Character.
2879 Vol. 231 (1933), pp. 289-337
- 2880 [128] B. Hespel, F. Maltoni, and E. Vryonidou, “Higgs and Z boson associated pro-
2881 duction via gluon fusion in the SM and the 2HDM”, JHEP 06 (2015) 065,
2882 [https://dx.doi.org/10.1007/JHEP06\(2015\)065](https://dx.doi.org/10.1007/JHEP06(2015)065), arXiv:1503.01656.

- 2883 [129] ATLAS Collaboration, “Measurements of Higgs boson produc-
 2884 tion and couplings in diboson final states with the ATLAS
 2885 detector at the LHC”, Phys. Lett. B726 (2013) 88âš119,
 2886 doi:10.1016/j.physletb.2014.05.011,10.1016/j.physletb.2013.08.010,
 2887 arXiv:1307.1427. [Erratum: Phys. Lett.B734,406(2014)].
- 2888 [130] CMS Collaboration, “Search for the associated production of a Higgs boson
 2889 with a single top quark in proton-proton collisions at $\sqrt{s} = 8$ TeV”, JHEP 06
 2890 (2016) 177,doi:10.1007/JHEP06(2016)177, arXiv:1509.08159.
- 2891 [131] B. Stieger, C. Jordà Lope et al., “Search for Associated Production of a Single
 2892 Top Quark and a Higgs Boson in Leptonic Channels”, CMS Analysis Note CMS
 2893 AN-14-140, 2014.
- 2894 [132] M. Peruzzi, C. Mueller, B. Stieger et al., “Search for ttH in multilepton final
 2895 states at $\sqrt{s} = 13$ TeV”, CMS Analysis Note CMS AN-16-211, 2016.
- 2896 [133] CMS Collaboration, “Search for H to bbar in association with a single top quark
 2897 as a test of Higgs boson couplings at $\sqrt{s} = 13$ TeV”, CMS Physics Analysis
 2898 Summary CMS-PAS-HIG-16-019, 2016.
- 2899 [134] CMS Collaboration, “Search for production of a Higgs boson and a single top
 2900 quark in multilepton final states in proton collisions at $\sqrt{s} = 13$ TeV”, CMS
 2901 Physics Analysis Summary CMS-PAS-HIG-17-005, 2016.
- 2902 [135] B. WG, “BtagRecommendation80XReReco”, February, 2017. <https://twiki.cern.ch/twiki/bin/view/CMS/BtagRecommendation80XReReco>.

- 2904 [136] CMS Collaboration, “Identification of b quark jets at the CMS Experiment
2905 in the LHC Run 2”, CMS Physics Analysis Summary CMS-PAS-BTV-15-001,
2906 2016.
- 2907 [137] M. Peruzzi, F. Romeo, B. Stieger et al., “Search for ttH in multilepton final1
2908 states at $\sqrt{s} = 13$ TeV”, CMS Analysis Note CMS AN-17-029, 2017.
- 2909 [138] CMS Collaboration, “Baseline muon selections for Run-II.” <https://twiki.cern.ch/twiki/bin/view/CMSPublic/SWGuideMuonIdRun2>, last accessed on
2910 24.02.2018.
- 2912 [139] G. Petrucciani and C. Botta, “Two step prompt muon identification”, January,
2913 2015. <https://indico.cern.ch/event/368007/contribution/2/material/slides/0.pdf>.
- 2915 [140] H. Brun and C. Ochando, “Updated Results on MVA eID with 13 TeV samples”,
2916 October, 2014. <https://indico.cern.ch/event/298249/contribution/3/material/slides/0.pdf>.
- 2918 [141] K. Rehermann and B. Tweedie, “Efficient Identification of Boosted Semileptonic
2919 Top Quarks at the LHC”, JHEP 03 (2011) 059, [https://dx.doi.org/10.1007/JHEP03\(2011\)059](https://dx.doi.org/10.1007/JHEP03(2011)059), arXiv:1007.2221.
- 2921 [142] CMS Collaboration. “Tag and Probe”, <https://twiki.cern.ch/twiki/bin/view/CMSPublic/TagAndProbe>, last accessed on 02.03.2018.
- 2923 [143] B. Maier, “SingleTopHiggProduction13TeV”, February, 2016. <https://twiki.cern.ch/twiki/bin/viewauth/CMS/SingleTopHiggsGeneration13TeV>.